

**NANO SCALE DEVICES FOR
PLASMONIC NANOLITHOGRAPHY AND RAPID SENSING OF BACTERIA**

A Dissertation

by

SUNGKYU SEO

Submitted to the Office of Graduate Studies of
Texas A&M University
in partial fulfillment of the requirements for the degree of

DOCTOR OF PHILOSOPHY

December 2007

Major Subject: Electrical Engineering

**NANO SCALE DEVICES FOR
PLASMONIC NANOLITHOGRAPHY AND RAPID SENSING OF BACTERIA**

A Dissertation

by

SUNGKYU SEO

Submitted to the Office of Graduate Studies of
Texas A&M University
in partial fulfillment of the requirements for the degree of

DOCTOR OF PHILOSOPHY

Approved by:

Chair of Committee,
Committee Members,

Mosong Cheng
Laszlo B. Kish
Kai Chang
Yue Kuo

Head of Department,

Costas N. Georghiades

December 2007

Major Subject: Electrical Engineering

ABSTRACT

Nano Scale Devices for Plasmonic Nanolithography and Rapid Sensing of Bacteria.

(December 2007)

Sungkyu Seo, B.S., Korea University

Chair of Advisory Committee: Dr. Mosong Cheng

This dissertation contains two different research topics. One is a ‘Nano Scale Device for Plasmonic Nanolithography – Optical Antenna’ and the other is a ‘Nano Scale Device for Rapid Sensing of Bacteria – SEPTIC’. Since these two different research topics have little analogy to each other, they were divided into different chapters throughout the whole dissertation. The ‘Optical Antenna’ and ‘Nanowell / Microwell / ISFET Sensor’ represent the device names of each topic ‘Plasmonic Nanolithography’ and ‘Rapid Sensing of Bacteria’, respectively.

For plasmonic nanolithography, we demonstrated a novel photonic device - Optical Antenna (OA) - that works as a nano scale object lens. It consists of a number of sub-wavelength features in a metal film coated on a quartz substrate. The device focuses the incident light to form a narrow beam in the near-field and even far-field region. The narrow beam lasts for up to several wavelengths before it diverges. We demonstrated that the OA was able to focus a sub-wavelength spot with a working distance (also the focal length) of several μm , theoretically and experimentally. The highest imaging resolution (90-nm spots) is more than a 100% improvement of the diffraction limit ($\text{FWHM} = 210 \text{ nm}$) in conventional optics. A model and 3D electromagnetic simulation results were also studied. Given its small footprint and sub-wavelength resolution, the PL holds great promise in direct-writing and scanning microscopy.

Collaborative work demonstrated a Nanowell (or Microwell) device which enables a rapid and specific detection of bacteria using nano (or micro) scale probe to monitor the electric field fluctuations caused by ion leakage from the bacteria. When a bacteriophage infects a bacterium and injects its DNA into the host cell, a massive and transitory ion efflux from the host cell occurs. SEPTIC (Sensing of Phage-Triggered Ion Cascade) technology developed by collaboration uses a nanowell device to detect the nano-scale electric field fluctuations caused by this ion efflux. The SEPTIC provides fast (within several minutes), effective (living cell only), phage specific (simple and less malfunction), cheap, compact and robust method for bacteria sensing. We fabricated a number of devices, including ‘Nanowell’, ‘Microwell’, and ‘ISFET (Ion Selective Field Effect Transistor)’, which detect bacteria-phage reactions in frequency domain and time domain. In the frequency domain, detected noise spectrum is characterized by $1/f^\beta$. The positive reaction showed much higher $\beta \cong 1$ than that of background noise or negative reaction ($\beta \cong 0$). For the time domain, we observed abnormal pulses ($> 8\sigma$) lasting 0.1 ~ 0.3 s which match the duration of ion flux reported by prior literatures. And the ISFET showed the phage-infection-triggered pulse in the form of the deviated drain current. Given the size of nanowell (or microwell, ISFET) and the simplified detection electronics, the cost of bacteria sensing is significantly reduced and the robustness is well improved, indicating very promising applications in clinical diagnosis and bio-defense.

DEDICATION

To my parents

ACKNOWLEDGEMENTS

It was a long journey to complete this study and there are numerous people who supported me. I would like to express my sincere appreciation to the chair of my committee, Dr. Mosong Cheng. Without his guidance and support, this study could not have been achievable. During the last 4 years, I have been impressed and learned many things in science as well as life by which I hope to make my future model and portrait. I am also deeply grateful to Dr. Laszlo B. Kish who gave me great advice, concern, and a huge number of recommendation letters. Dr. Kai Chang and Dr. Yue Kuo, members of the advisory committee, should be remembered at the first line of acknowledgement list for their unique contribution. Regarding nanowell experiments, I appreciate to Dr. Maria King for her great collaboration and support.

I am very thankful to the Solid State Electronics Group colleagues Yongwook Shin, Hyunchul Kim, Hyungduk Ko, Liu Chao, Phillip Ping, Jaewon Park, Hyunsoo Park, Jungmoo Hong and Nick Jing, for their invaluable assistance and wonderful friendship during my Ph.D. courses. I am also thankful to Robert A. Atkins and James Gardner for their technical assistance. In addition, I truly appreciate all my Korean Catholic Community friends at St. Mary's who prayed for and encouraged me.

Finally, I would like to share my pleasure in completing this study with my wife Seokjin, my son Justin (Taebin), my family, and her family who have waited for this moment such a long time.

TABLE OF CONTENTS

	Page
ABSTRACT	iii
DEDICATION	v
ACKNOWLEDGEMENTS	vi
LIST OF TABLES	ix
LIST OF FIGURES	x
CHAPTER I INTRODUCTION	1
1.1 Organization of the Dissertation	1
1.2 Plasmonic Nanolithography Using Surface Plasmon	2
1.2.1 Background.....	2
1.2.2 Literature Review	3
1.2.3 Purpose and Objective of This Study	8
1.3 Rapid Sensing of Bacteria through Electrical Noise – SEPTIC.....	8
1.3.1 Background.....	8
1.3.2 Literature Review	9
1.3.3 Purpose and Objective of This Study	10
CHAPTER II PLASMONIC NANOLITHOGRAPHY - THEORY	12
2.1 Theory	12
2.1.1 Surface Plasmon and Metamaterial	12
2.1.2 Wave Equation and Wavevector.....	15
2.2 Design and Modeling of Optical Antenna	22
2.3 Finite-Difference-Time-Domain (FDTD) Simulation	26
2.3.1 Methodology.....	26
2.3.2 Light after a Sub-Wavelength Hole	28
2.3.3 Light after a Tiny Ring	33
CHAPTER III PLASMONIC NANOLITHOGRAPHY - EXPERIMENT	43
3.1 Device Fabrication and Experiment Apparatus	43
3.2 Experiment Results	46
3.3 Summary	51
CHAPTER IV PLASMONIC NANOLITHOGRAPHY – CONCLUSION	52
4.1 Conclusion	52
4.2 Future Application	53

	Page
CHAPTER V RAPID SENSING OF BACTERIA – SEPTIC	54
5.1 SEPTIC (SEnsing of Phage-Triggered Ion Cascade).....	54
5.1.1 Phage Specific Reaction	54
5.1.2 Detection Principle of the SEPTIC	56
CHAPTER VI RAPID SENSING OF BACTERIA – EXPERIMENT.....	61
6.1 Device Fabrication	61
6.1.1 Nanowell and Microwell Sensor.....	61
6.1.2 Ion Selective Field Effect Transistor (ISFET) Sensor	68
6.2 Experiment Apparatus.....	71
6.3 Experiment Results	73
6.3.1 Nanowell / Microwell Sensor	73
6.3.2 ISFET Sensor.....	79
6.4 Summary	82
CHAPTER VII RAPID SENSING OF BACTERIA – CONCLUSION.....	83
7.1 Conclusion	83
7.2 Future Application	84
REFERENCES.....	85
APPENDIX A	89
APPENDIX B.....	95
APPENDIX C.....	96
APPENDIX D	101
VITA	118

LIST OF TABLES

	Page
Table 2.1 Wavevectors on Case Studied Materials with Air Interface	34
Table 5.1 ICTV Classification of Phages	55
Table 5.2 Three Classic Coliphages.....	56
Table 6.1 The Average β of the Positive and Negative Noises	78

LIST OF FIGURES

	Page
Fig. 1.1 AFM Scans of Gratings After Exposure and Experiment.....	5
Fig. 1.2 AFM Image Comparison With and Without Silver Superlens.....	6
Fig. 1.3 Effects of Parameters on Zero-Order Transmission Spectra.....	7
Fig. 2.1 EM Waves and Characteristics of SP.....	13
Fig. 2.2 Illustration of the Negative Refraction of Two Waves	14
Fig. 2.3 Dispersion Curve for a SP Mode.....	17
Fig. 2.4 SP Wave Numbers of Highly Conductive Metals.....	19
Fig. 2.5 Design of an Optical Antenna.....	23
Fig. 2.6 Simulations of the Optical Field.....	26
Fig. 2.7 (a) Circular Aperture Geometry (b) The Airy Pattern.....	29
Fig. 2.8 Surface Waves Passing Through a Sub-Wavelength Hole.....	30
Fig. 2.9 Electric Field Intensity	32
Fig. 2.10 Electric Field Intensity $\langle E ^2 \rangle$ Comparison at the Exit of a Sub-Wavelength Hole	33
Fig. 2.11 Light Field Passing Through a Simple Ag Ring Aperture	35
Fig. 2.12 Light Intensity Distribution of a Simple Ag Ring Aperture.....	36
Fig. 2.13 Light Field Passing Through a Simple Al Ring Aperture	37
Fig. 2.14 Light Intensity Distribution of a Simple Al Ring Aperture.....	38
Fig. 2.15 Light Field Passing Through a Simple Cr Ring Aperture	39
Fig. 2.16 Light Intensity Distribution of a Simple Cr Ring Aperture.....	40
Fig. 2.17 Light Field Passing Through a Simple Ti Ring Aperture	41
Fig. 2.18 Light Intensity Distribution of a Simple Ti Ring Aperture	42

	Page
Fig. 3.1 Optical Antenna Fabrication Processes.....	44
Fig. 3.2 Scanning Electron Micrograph (SEM) of the Fabricated Optical Antenna	44
Fig. 3.3 Experiment Apparatus to Record the Optical Field Emanating from an Optical Antenna.....	45
Fig. 3.4 Atomic Force Micrograph (AFM) of the Developed Spots in the Resist.....	47
Fig. 3.5 SEM of the Developed Spots Whose Periods are 300 nm, 400 nm, and 500 nm	48
Fig. 3.6 SEM of the Simple Optical Antenna.....	49
Fig. 3.7 A Set-Up for the Contact Printing Experiment Using a Simple Optical Antenna	49
Fig. 3.8 AFM Image of the Over Exposed Si Sample with a Simple Optical Antenna.....	50
Fig. 5.1 Illustration of the Detection Principles of the SEPTIC Technology	58
Fig. 6.1 Top-Down View of the Chip with Nanowell, Contact Pads and Bridges	61
Fig. 6.2 Fabrication Processes of the Nanowell	63
Fig. 6.3 Fabricated Nanowell	64
Fig. 6.4 Top-Down View of the Microwell Array with Different Gaps.....	65
Fig. 6.5 Fabrication Processes of the Microwell Array	67
Fig. 6.6 Fabricated Microwell Array	67
Fig. 6.7 Fabrication Processes of the ISFET	70
Fig. 6.8 Fabricated ISFET Sensor	71
Fig. 6.9 Experiment Apparatus for the Nanowell / Microwell Sensor	73
Fig. 6.10 Response with Lamda-UR Phages with Different Host Bacteria.....	75
Fig. 6.11 The Spectrum Measured in the 100 um Gap Device.....	75
Fig. 6.12 Time Series of the Measured Voltage in Positive Test (<i>E-coli</i> plus T7 phage)	77
Fig. 6.13 Time Series of the Measured Voltage in Negative Test (T7 phage only)	77

	Page
Fig. 6.14 The PSD of a Positive Noise (<i>E-coli</i> plus T7 Phage, the Solid Red Curve) and a Negative Noise (T7 Phage only, the Dotted Blue Curve).....	78
Fig. 6.15 ISFET IV-Characteristics with E-coli (coded 17181) Bacteria and Lambda-UR Phages.....	80

CHAPTER I

INTRODUCTION

1.1 Organization of the Dissertation

This dissertation contains two different research topics. One is a ‘Nano Scale Device for Plasmonic Nanolithography – Optical Antenna’ and the other is a ‘Nano Scale Device for Rapid Sensing of Bacteria – SEPTIC’. Since those two different research topics have little analogy each other, they were divided into different chapters throughout the whole dissertation. The ‘Optical Antenna’ and ‘Nanowell / Microwell / ISFET Sensor’ represent the device names of each topic ‘Plasmonic Nanolithography’ and ‘Rapid Sensing of Bacteria’, respectively.

This chapter surveys and discusses the technical background, prior literatures and the objective of the proposed research topics as an introduction to the dissertation.

Chapter II, plasmonic nanolithography - theory, discusses the theory, design and modeling of optical antenna, and finite-difference-time-domain simulation. The theory section consists of surface plasmon and metamaterial, wave equation and wavevector, and design and modeling of optical antenna are also provided. In the finite-difference-time-domain (FDTD) simulation section, a characterization of light wave after various highly conductive metals such as Ag, Al, Cr, and Ti would be discussed with a circular aperture and a ring aperture. Simulation methodology is also included in this section.

Chapter III, plasmonic nanolithography – result, provides device fabrication and experiment apparatus, experiment result, and brief summary of plasmonic nanolithography.

Chapter IV concludes the plasmonic nanolithography and shows future applications.

Chapter V, rapid sensing of bacteria – SEPTIC, covers an overview of the other research

topic. SEPTIC (SEnsing of Phage Triggered Ion Cascade) technology is introduced, and phage specific reaction and detection principle of the SEPTIC are also discussed.

In chapter VI, rapid sensing of bacteria – experiment, device fabrication, experiment apparatus, and experiment result are explained in detail. Roughly, two types of sensing devices Nanowell (and Microwell) and Ion Selective Field Effect Transistor (ISFET) are described in the device fabrication and experiment result section. A summary for rapid sensing of bacteria is given at the end of this chapter.

Finally, chapter VII discuss the conclusion and future applications of the second topic, rapid sensing of bacteria.

Wavevectors and optical property of highly conductive materials, simulation code, analysis code, and a number of simulation results on the circular aperture and ring aperture in highly conductive metals are included in the appendix to help to understand the achievement of the plasmonic nanolithography.

1.2 Plasmonic Nanolithography Using Surface Plasmon

1.2.1 Background

A perfect lens which is ideally made of corrected glass that is free of aberration, has been believed as the best solution to achieve the smallest focus in a diffraction-limited system. To realize sub-wavelength resolution focusing, however, recent progresses of nano fabrication techniques provided alternatives to circumvent polishing the lens more precisely or inventing slightly better dielectric by adopting sub-wavelength structures, e.g. periodic apertures, which can excite and scatter plasmon waves.

Instead of a perfect lens, Near-field Scanning Optical Microscope (NSOM) uses a nano size probe to scan and illuminate a sample to achieve sub-wavelength resolution imaging.

However, the probe, which is usually a tapered optical fiber tip, results in very weak signal power (transmission coefficient of 10^{-2} - 10^{-6}), short working distance (probe to sample distance should be within 10nm), and small depth-of-field (the region being illuminated is within 10 nm in the axial direction). The resulted poor image contrast and slow scanning speed severely limit the applications of NSOM. To achieve a strong light field, sub-wavelength surface plasmonic (SP) structures substituting the NSOM probe which provided up to 25 nm resolution in the near-field region have been adopted by several research groups, but the working distance is still within a fraction of the wavelength.^{1,2}

We propose a novel photonic device - Optical Antenna - that acts as a nano scale objective lens. It consists of a number of sub-wavelength features in a metal film coated on a quartz substrate. The device focuses the incident light to form a narrow beam in the near field and even far field region. The narrow beam lasts up to several wavelengths before it diverges. This device showed much larger working distance (probe to sample distance is 1.7 μm or more) and enabled 95 nm resolution maskless lithography (95 nm spots and lines) with 405 nm light source. This is far beyond the diffraction limit in optics. This would also allow for high speed scanning, large field-of-view and significantly improved image contrast, and imaging details. Given its small footprint and sub-wavelength resolution, the Optical Antenna holds great promise in direct writing and scanning microscopy.

1.2.2 Literature Review

Sub-wavelength imaging in a diffraction-limited system can be achieved via a variety of means such as apodization,³ confocal microscopy and liquid immersion microscopy and/or lithography.⁴ Recent progresses of nano fabrication techniques provided alternatives to these techniques by creating sub-wavelength apertures which can excite optical near field with lateral dimensions much shorter than the wavelength. However, the issues associated with the light

emerging from these sub-wavelength apertures, such as very low transmission and diffraction toward all directions, make them only effective within a fraction of wavelength from the apertures.⁵ This brings particular difficulties to lithography, which needs to pattern a resist layer of certain thickness in the presence of wafer topographical variation. In other words, an effective lithography technique must provide a satisfactory working distance (WD; distance between apertures and a sample) and depth-of-field (DOF; distance in front of and beyond the subject that appears to be in focus).

Near-field scanning optical microscopy (NSOM) has been an exciting modality which permits super-resolution imaging of samples, breaking the diffraction barrier of light. However, one of the major disadvantages of the NSOM is that the object must be placed within a fraction of wavelength from the measuring probe, which makes the imaging of thick specimen impossible. This severely limits the applications of NSOM in some fields where large WD or DOF are necessary, including biological imaging and nanolithography. The former often needs to image the interiors of cells rather than the surfaces, and the latter usually needs to expose a resist layer of certain thickness. Moreover, the small WD means a great danger of physical contact between the optical probe and the object. The small WD and DOF are mainly restrained by the issues associated with the light emerging from sub-wavelength apertures used in NSOM, including very low transmission and diffraction toward all directions.⁵

Since it was proposed that the near field can be enhanced by surface plasmon (SP) excited on a metal layer whose dielectric constant is negative,⁶ sub-wavelength plasmonic imaging techniques, which promise higher transmission and confinement of near-field, have been widely investigated. A SP is an electromagnetic surface mode excited on the interface between a metal and a dielectric material. The SP decays exponentially in both the lateral and the axial direction. Meanwhile, the wavelength of SP can be shorter than the corresponding light.

Thus the imaging resolution using SP can be much higher than the diffraction limit. The SP, as a result of collective oscillation of free electrons in metal, is much stronger than the near field directly created by a sub-wavelength aperture. This means the plasmonic imaging has much higher throughput than conventional near-field optics.

The plasmonic imaging techniques that have been reported are similar to contact lithography except that they insert a metal film, e.g. silver (Ag) or aluminum (Al), between a mask and a resist layer⁷⁻⁹ or deposit a titanium (Ti) shield on a sample¹⁰ to improve the resolution. For example, a 60 nm hole array can be patterned with i-line illumination.¹¹ Even though there is a controversy whether it was over development or super lensing effect,¹² Blaikie et al. demonstrated that 250 nm resolution in proximity lithography with mercury lamp source when a silver film was inserted between the mask and the wafer (Fig. 1.1).¹³

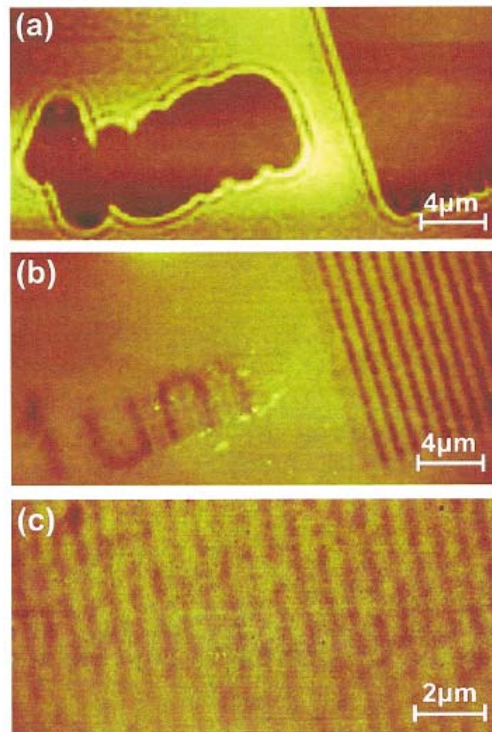


Fig. 1.1 AFM Scans of Gratings After Exposure and Experiment. (a) A proximity exposure of a 1 μm grating, (b) a silver lens exposure of a 1 μm grating, and (c) the smallest features resolved during the silver lens exposures.¹³

Zhang et al. reported a novel superlens that images a nano object in near field as shown in Fig. 1.2.⁷ The superlens imaging results show that the nano-wire object with 120 nm period is clearly resolved (Fig. 1.2(a)) and the height modulation of the recorded image is observed in cross-section plot (Fig. 1.2(b)). These results are strong indications that the evanescent field of the object is restored and recorded as an image by superlensing. With this design, 60 nm half-pitch object has been successfully imaged with 364 nm incident wavelength, which is 1/6 resolution, well beyond the diffraction limit. The control experiment result evidently supports the role of silver as a superlens. Without the silver, no image contrast is recorded by photoresist (Fig. 1.2(c)) and its cross section (Fig. 1.2(d)) also show no evidences of periodic structure imaged by the control sample.

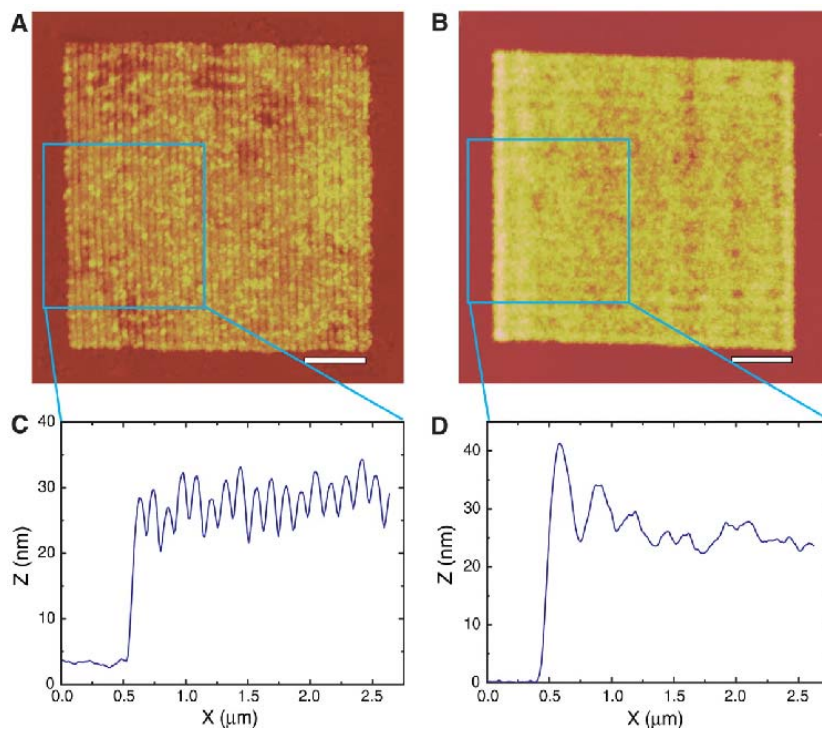


Fig. 1.2 AFM Image Comparison With and Without Silver Superlens. (a) The image of 120 period grating object recorded by superlensing, (b) its average cross section, (c) the image of same grating object recorded without superlens, and (d) its average cross section.⁷

Although SP structures have been used to create strong near-field as small as 25 nm, the distance between the mask and the resist, namely the WD, is still within a fraction of the wavelength due to the decay of SP in the axial direction.¹⁴⁻¹⁶ The small WD brings great difficulties in overlay and alignment, mask contaminations, focusing and dose control, etc., which severely limit the manufacturability.

The effects of SP in far-field have also been studied. Researchers demonstrated that SP resonant structures, e.g. a periodic texture on the exit side of an aperture in a metal film, can enhance the transmitted light wave and confine it to a small divergence angle in Fig. 1.3.¹⁷⁻²⁰

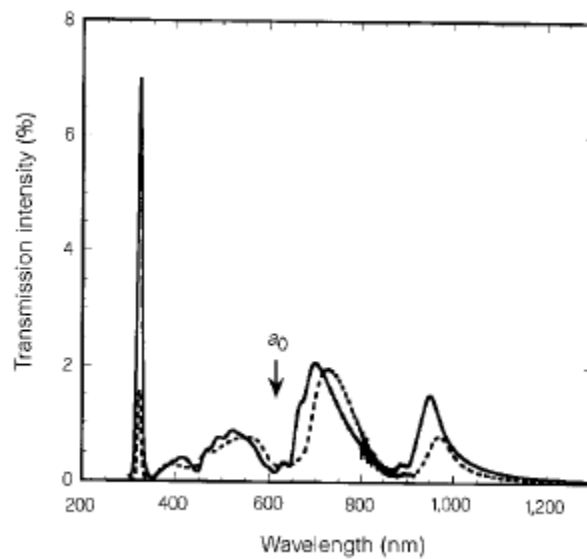


Fig. 1.3 Effects of Parameters on Zero-Order Transmission Spectra. Spectra for two identical Ag arrays with different thicknesses. Solid line: $t = 200$ nm; Dashed line: $t = 500$ nm. For both arrays: period = 600 nm, hole diameter = 150 nm.¹⁷

The propagation of SP to far-field is attributed to it being scattered by surface structures on the metal.²¹ The propagating SP is nothing more than an electromagnetic wave in the free space. So it is not expected to achieve sub-diffraction resolution in far-field.

1.2.3 Purpose and Objective of This Study

The purpose of this research could be summarized as understanding the effect of surface plasmon in plasmonic imaging, achieving a sub-wavelength resolution focus smaller than zone plate nanolithography which uses diffractive optics,²² improving working distance and depth-of-field to a satisfactory level for non-contact lithography, and demonstrating the plasmonic nanolithography which goes beyond the diffraction limit in optics. To achieve those purposes, we defined the objectives as follows.

1. Characterization of a light wave spatially modulated by the nano structures.
2. Development of a sub 100nm resolution plasmonic nanolithography technology, device, and system.
3. Improvement of the working distance to the several orders of the incident wavelength.
4. Improvement of the depth-of-field to the reasonable value to be used in lithography.

1.3 Rapid Sensing of Bacteria through Electrical Noise – SEPTIC

1.3.1 Background

One of the most imperative needs in clinical and agricultural practice as well as in homeland security applications is the rapid and sensitive identification of bacteria. For example, certain strains of the bacterium *Escherichia coli* (*E. coli*) can cause widespread illness if they get into the food supply. Even though several technologies are available for the identification of bacteria or viruses in humans, veterinary and agricultural diagnostic laboratories, such as culturing and polymerase chain reaction (PCR), these approaches have difficulties such as time

required for culturing of bacteria, expensive instrumentation or poor selectivity between living and dead bacteria. A rapid and inexpensive method for detecting and sub-typing bacteria suitable for large-scale surveillance efforts, much less employment in the field, is not available.

1.3.2 Literature Review

Solid-state biological sensors have the potential to satisfy this need due to their compactness, fast response to target, potential for integration with digital/analog electronics and potential advantage in mass production. The majority of these sensors use a bio-affinity element for sensing. This involves an antibody, binding protein or receptor protein that forms a stable complex with a corresponding ligand. The bio-affinity protein-ligand complex is stable enough to result in signal transduction. The complex can be detected with the help of a label such as an enzyme, fluorophore or electroactive substance.²³ Redox enzymes are the major components in constructing bio-affinity sensors, and electrochemically active substances are used in signal transduction.^{23,24} Examples of bioaffinity sensors include Enzyme Field Effect Transistor (ENFET)²⁵, ImmunoFET^{26,27}, etc.²⁸⁻³² For practical solid-state biosensors, however, several issues need to be considered, such as the limited sensitivity due to the poor charge variation caused by biological processes, non-specific response due to interfering ions or other substances present in the solution, and the limited stability of the electrochemically active membrane on the gate of the specific MOSFET.³³

Several nanotechnology-based methods have been proposed. All these methods, like other sensors, use a sensing element and a transducer. The sensing element, such as an antibody or a phage, seeks specific bacteria and, once it finds a target, triggers certain physiological and/or chemical reactions. The transducer then converts the reactions to electrical or optical signals for analysis. Currently being explored transducers include ferrofluid magnetic nanoparticles (NPs)^{34,35}, ceramic nanospheres and quantum dots (QDs). Tan et al. developed a bioconjugated NP-

based assay for in-situ pathogen quantification that can detect a single bacterium within 20 min³⁶. Dye-loaded NPs are conjugated with antibodies. When an antibody finds a specific bacterium, the conjugated NP provides a very bright fluorescent signal. Edgar et al. reported an approach that combines in vivo biotinylation of engineered host-specific bacteriophage and conjugation of the phage to quantum dots. The method provides specific detection of as few as 10 bacterial cells per milliliter, with a 100-fold amplification of the signal over background in 1 hr.³⁷ In this apparatus, phages were genetically engineered to produce a specific protein on their surface. When these phages infect bacteria and reproduce, the bacteria burst and release many phage progeny attached to biotin (vitamin H). The biotin-capped phages selectively attract streptavidin-coated QDs. The resulting phage-quantum dot complexes can be detected and counted using microscopy, spectroscopy or flow cytometry.

Kish et al reported that the detection capability of a solid-state sensor can be dramatically improved by the aid of Fluctuation Enhanced Sensing (FES).³⁸ The interaction between a sensing probe and an analyte is always a dynamic stochastic process. Micro-fluctuations that result from this interaction carry a “stochastic fingerprint” of the analyte, and contain much more information than the mean value alone. Thus fluctuation-enhanced sensing can improve sensitivity, selectivity, and reduce false alarm rates by orders of magnitude over conventional sensor systems that only measure the average values.³⁸ In the simplest version of FES, the power density spectrum (PSD) of the detected fluctuations is used as the detected signal.³⁹

1.3.3 Purpose and Objective of This Study

The purpose of this research is the rapid and sensitive identification of bacteria. To attain the purpose, we have schemed following objectives.

1. Detection and identification of a specific bacterium should be completed within a few minutes.
2. Development of a sensor which is reasonably inexpensive and has less mal-function for detecting a specific bacterium.
3. Development of a sensor having integration compatibility and compactness.
4. Improvement of a sensitivity in bacteria detection,
5. Proof of the Fluctuation Enhanced Sensing (FES) technology.

CHAPTER II

PLASMONIC NANOLITHOGRAPHY - THEORY

Optical Antenna (OA) is a device which consists of metal nano-structures on a fused silica substrate. The OA focuses an incident light to a spot narrower a diffraction limit in conventional optics with a focal length of several wavelength, so it can be also called as ‘Nano Objective Lens’. To create the sub-wavelength spot, the OA utilizes the engineered large wavevector of the surface electromagnetic field excited between metal nano-structures and dielectric interface.

2.1 Theory

2.1.1 Surface Plasmon and Metamaterial

Surface Plasmon (SP) is a collective oscillation of electron gas at the surface of a conductive metal that can be excited by the electromagnetic waves under certain conditions. Because of its evanescent characteristics, it can’t travel far, so for a long time SP has received little attention except for some sensing applications. However, thanks to the progress in fabrication technique of micro/nano scale structures, SP becomes a hot research area since micro/nano structures can alter the interaction of light with electron.⁴⁰

The electromagnetic field applied in a metal results in a combined electromagnetic wave as shown in Fig. 2.1 (a). SP at the interface between a metal and a dielectric material has a transverse magnetic component, and the generated surface charge induces an electric field normal to the surface. This combined character leads to a field component perpendicular to the surface that decays exponentially with the distance from the surface (b). The electric field perpendicular to the surface is evanescent, meaning bounded and non-radiative, and can’t be

propagating from the surface. The distance that SP propagates from the surface is determined by the decay length (δ_d) of the field in dielectric and the skin depth (δ_m) in metal. Usually, the decay length (δ_d) of the field in dielectric is comparable to a half of the incident light wavelength.⁴¹

A metamaterial is a material that gains its property from structure rather than composition. The term ‘meta’ means ‘beyond’ in Greek, so ‘metamaterial’ means ‘beyond a conventional material’.¹⁴ Metamaterial is used when a specific material has a property that has not been found naturally, thus it was defined as ‘macroscopic composites having a manmade, three-dimensional, periodic cellular architecture designed to produce an optimized combination, not available in nature, of two or more responses to specific excitation’ by R. M. Walser in 2002.⁴² Usually, Metamaterial is composed of periodic structures at least as small as the wavelength of the electromagnetic radiation it interacts with.

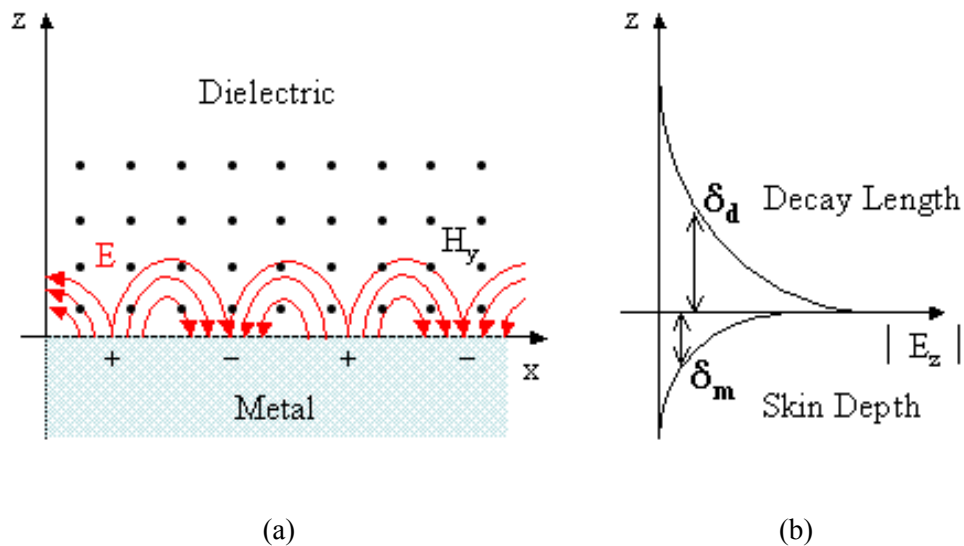


Fig. 2.1 EM Waves and Characteristics of SP. (a) TM field on a metal surface. H is in y direction (b) Evanescent characteristics prevents SP from being propagating to the dielectric medium.

One of the most exciting opportunities for the metamaterial is the development of Negative Refractive Index Material (NRIM). NRIM make it possible that was not achievable with current optics technology.¹³ For example, a negative refractive index medium bends light to a negative angle as shown in Fig. 2.2. Light usually diverging from a point source is set in reverse manner, so it converges into a point after the negative refractive medium.⁶

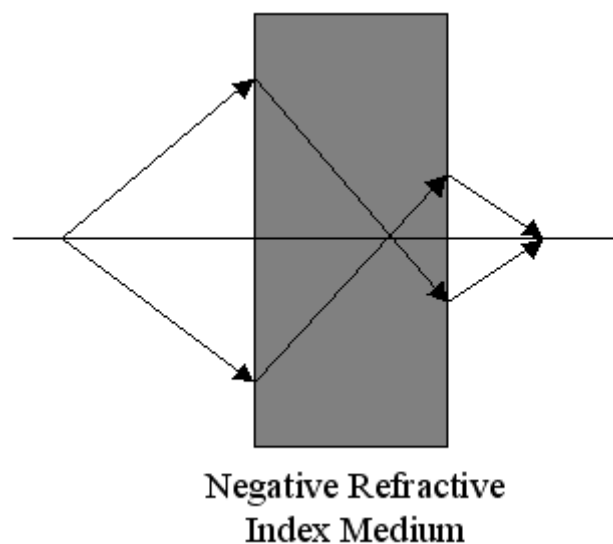


Fig. 2.2 Illustration of the Negative Refraction of Two Waves.

A superlens which uses the negative refraction property and has the power to transmit all Fourier components of a 2D image is a good application of NRIM. The superlens proposed by Sir Pendry and realized by Zhang group uses a thin silver slab to allow the imaging of objects with a sub-wavelength resolution.⁷ The superlens only requires a condition $\epsilon_m = -\epsilon_d$ for superlensing effect where ϵ_m, ϵ_d are the permittivities of the metal and the dielectric ($\epsilon_d = 1$ for air). Although it is limited to the near-field region, the superlens enables sub-wavelength

lithography and optical imaging assisted by surface plasmon excitation. Experiments with the silver slab (superlens) have already shown extended evanescent waves and super resolution optical imaging far beyond the diffraction limit in conventional optics.

2.1.2 Wave Equation and Wavevector

Although SP is resulted from the quantization of classical light reaction with electrons, most of the SP's property can be derived directly from Maxwell equations. As illustrated in Fig. 2.1, considering two media, one is metal and the other is dielectric. Maxwell equations give the wave equations for the electric field (\vec{E}) and magnetic field (\vec{H}) with assumptions of zero charge density ($\rho = 0$) and zero current density ($\vec{J} = 0$) in those two media.

$$\nabla^2 \vec{E} = \frac{\mu\epsilon}{c^2} \frac{\partial^2 \vec{E}}{\partial t^2} \quad (2.1a)$$

$$\nabla^2 \vec{H} = \frac{\mu\epsilon}{c^2} \frac{\partial^2 \vec{H}}{\partial t^2} \quad (2.1b)$$

Solving Eq. (2.1) provides wave equations

$$\vec{E}(\vec{r}, t) = \vec{E}_0 \cdot \exp(ik_x x + ik_y y + ik_z z - i\omega t) \quad (2.2a)$$

$$\vec{H}(\vec{r}, t) = \vec{H}_0 \cdot \exp(ik_x x + ik_y y + ik_z z - i\omega t) \quad (2.2b)$$

are solutions propagating to the \vec{k} direction with angular frequency ω in Cartesian coordinate. The wave equation implements a relation between the magnitude of \vec{k} and ω as

$$k^2 = \frac{\omega^2}{c^2} \mu\epsilon \quad (2.3)$$

The Eq. (2.3) is known as the dispersion relation and k varies with the frequency ω . In a dielectric material such as air or glass, where $\mu = 1$ and ϵ varies with the frequency, the light is dispersed.

Now, we need to investigate further for the Eq. (2.2) with specific boundary conditions. In case of the TE (Transverse Electric) mode, because $\vec{E} = (0, E_y, 0)$ and $\vec{H} = (H_x, 0, H_z)$, there is no surface plasmon in x and z directions. But if we assume the TM (Transverse Magnetic) mode, we can use the field components of the x and z axes with $\vec{E} = (E_x, 0, E_z)$ and $\vec{H} = (0, H_y, 0)$. Then, there are a set of surface wave solutions for Eq. (2.2) at $z = 0$ plane having no y-component. For metal where $z \leq 0$,

$$E_{x,m} = E_0 \cdot \exp(ik_{sp}x - i\omega t) \cdot \exp\left(+z \cdot \sqrt{k_{sp}^2 - \epsilon_m \frac{\omega^2}{c^2}}\right) \quad (2.4a)$$

$$E_{y,m} = 0 \quad (2.4b)$$

$$E_{z,m} = \frac{-ik_{sp}E_0}{\sqrt{k_{sp}^2 - \epsilon_m \frac{\omega^2}{c^2}}} \cdot \exp(ik_{sp}x - i\omega t) \cdot \exp\left(+z \cdot \sqrt{k_{sp}^2 - \epsilon_m \frac{\omega^2}{c^2}}\right) \quad (2.4c)$$

and for dielectric where $z \geq 0$,

$$E_{x,d} = E_0 \cdot \exp(ik_{sp}x - i\omega t) \cdot \exp\left(-z \cdot \sqrt{k_{sp}^2 - \epsilon_d \frac{\omega^2}{c^2}}\right) \quad (2.5a)$$

$$E_{y,d} = 0 \quad (2.5b)$$

$$E_{z,d} = \frac{+ik_{sp}E_0}{\sqrt{k_{sp}^2 - \epsilon_d \frac{\omega^2}{c^2}}} \cdot \exp(ik_{sp}x - i\omega t) \cdot \exp\left(-z \cdot \sqrt{k_{sp}^2 - \epsilon_d \frac{\omega^2}{c^2}}\right) \quad (2.5c)$$

These equations should satisfy the boundary conditions, i.e., continuity of the tangential and normal components of \vec{E} and \vec{H} , at $z = 0$ imposed by Maxwell equations as follows.

$$E_{x,m}(z=0) = E_{x,d}(z=0), H_{x,m}(z=0) = H_{x,d}(z=0) \quad (2.6a)$$

$$E_{z,m}(z=0) = E_{z,d}(z=0), H_{z,m}(z=0) = H_{z,d}(z=0) \quad (2.6b)$$

For \vec{E} , this is met by the choice of E_0 , and for \vec{H} we have the constraint that

$$-\varepsilon_m \sqrt{k_{sp,x}^2 - \varepsilon_d \frac{\omega^2}{c^2}} = \varepsilon_d \sqrt{k_{sp,x}^2 - \varepsilon_m \frac{\omega^2}{c^2}} \quad (2.7)$$

where ε_m is negative and Eq. (2.7) provides

$$k_{sp,x} = \frac{\omega}{c} \sqrt{\frac{\varepsilon_m \varepsilon_d}{\varepsilon_m + \varepsilon_d}} = \frac{2\pi}{\lambda_0} \sqrt{\frac{\varepsilon_m \varepsilon_d}{\varepsilon_m + \varepsilon_d}} = k_0 \sqrt{\frac{\varepsilon_m \varepsilon_d}{\varepsilon_m + \varepsilon_d}} \quad (2.8)$$

Since ε_d is always positive, the Eq. (2.8) says that $\varepsilon_m + \varepsilon_d < 0$ to have SP waves. This momentum mismatch between $k_{sp,x}$ and k_0 that must be solved in order to couple light and SP mode together. SP mode always lies beyond the incident light line and this particular property make SP having a greater wavevector and smaller wavelength at the same frequency as depicted in Fig. 2.3.

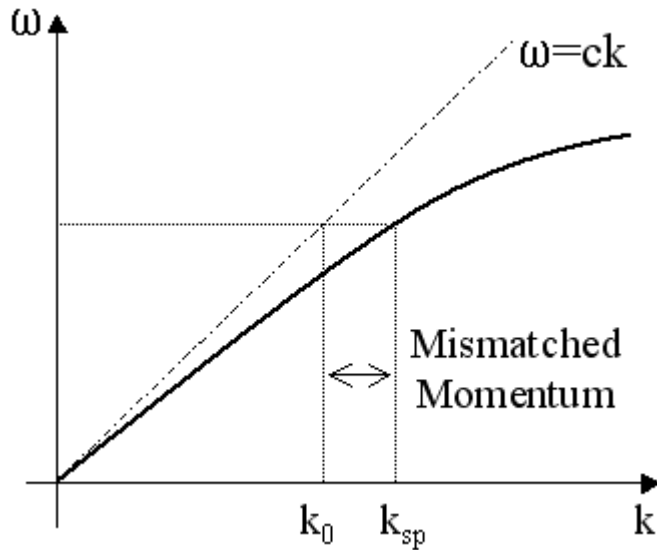


Fig. 2.3 Dispersion Curve for a SP Mode.

To derive the SP wavevectors propagating to the +z and -z directions into the dielectric and the metal, we need to modify Eq. (2.3) with Maxwell equations as following

$$k_{sp,x}^2 + k_{sp,zm}^2 = k_0^2 \epsilon_m \quad (2.9a)$$

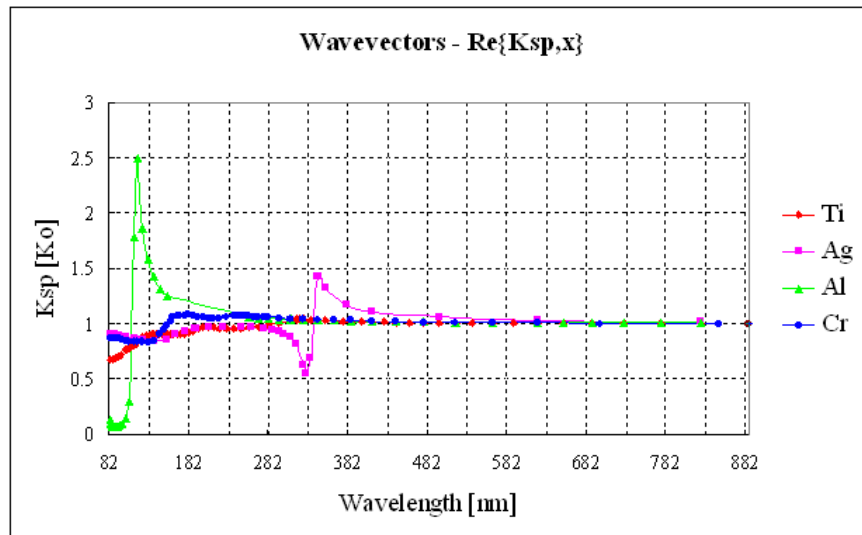
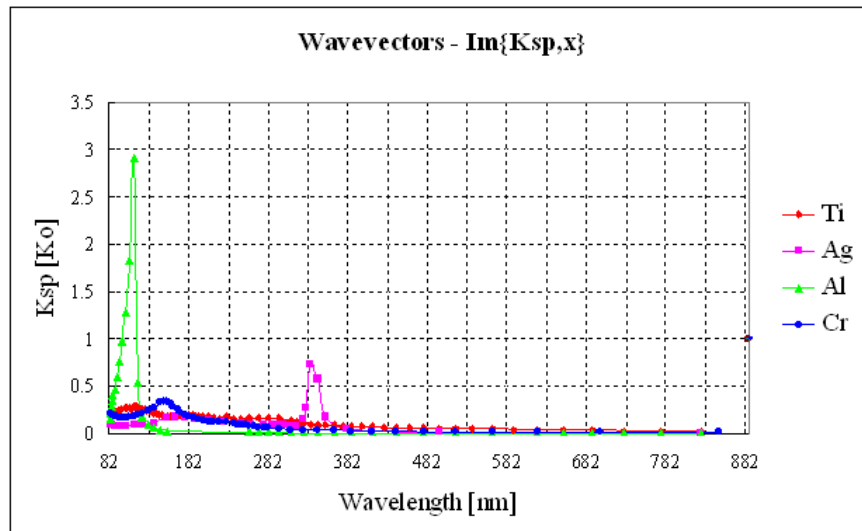
$$k_{sp,x}^2 + k_{sp,zd}^2 = k_0^2 \epsilon_d \quad (2.9a)$$

where k_0 is the wavevector of the incident light. Combining Eq. (2.8) and (2.9) results in

$$k_{sp,zd} = \frac{\omega}{c} \sqrt{\frac{\epsilon_d^2}{\epsilon_m + \epsilon_d}} = \frac{2\pi}{\lambda_0} \sqrt{\frac{\epsilon_d^2}{\epsilon_m + \epsilon_d}} = k_0 \sqrt{\frac{\epsilon_d^2}{\epsilon_m + \epsilon_d}} \quad (2.10a)$$

$$k_{sp,zm} = \frac{\omega}{c} \sqrt{\frac{\epsilon_m^2}{\epsilon_m + \epsilon_d}} = \frac{2\pi}{\lambda_0} \sqrt{\frac{\epsilon_m^2}{\epsilon_m + \epsilon_d}} = k_0 \sqrt{\frac{\epsilon_m^2}{\epsilon_m + \epsilon_d}} \quad (2.10b)$$

Eqs. (2.8) and (2.10) could be used to predict engineered wavevector and propagation length in different media. To find wavevectors in SP mode, Eqs. (2.8) and (2.10) are enough, but for the SP propagation we need to use a relation $\Lambda = 1/\text{Im}\{k_{sp}\}$ where Λ is a decay length of SP. Figs. 2.4 shows SP wavevectors of highly conductive metals (Ti, Al, Ag, and Cr) interfaced with a dielectric material of the refractive index $n=1$ (air) at 82 ~ 882 nm incidence wavelength; (a) $\text{Re}\{k_{sp,x}\}$ plot, (b) $\text{Im}\{k_{sp,x}\}$ plot, (c) $\text{Re}\{k_{sp,zd}\}$ plot, (d) $\text{Im}\{k_{sp,zd}\}$ plot, (e) $\text{Re}\{k_{sp,zm}\}$ plot, and (f) $\text{Im}\{k_{sp,zm}\}$ plot. The optical property of each material⁵⁶ and calculated wavevectors are listed in the Appendix A.

(a) $\text{Re}\{k_{\text{sp},x}\}$ plot(b) $\text{Im}\{k_{\text{sp},x}\}$ plot**Fig. 2.4 SP Wave Numbers of Highly Conductive Metals.**

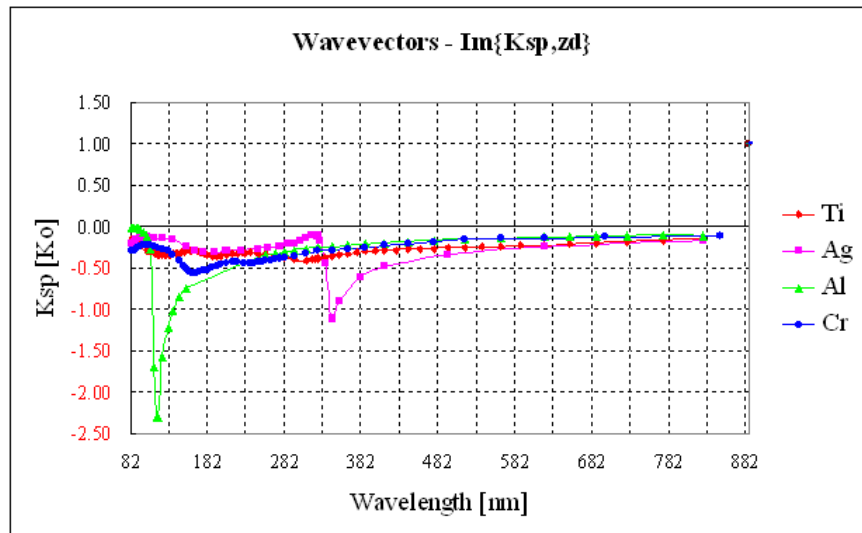
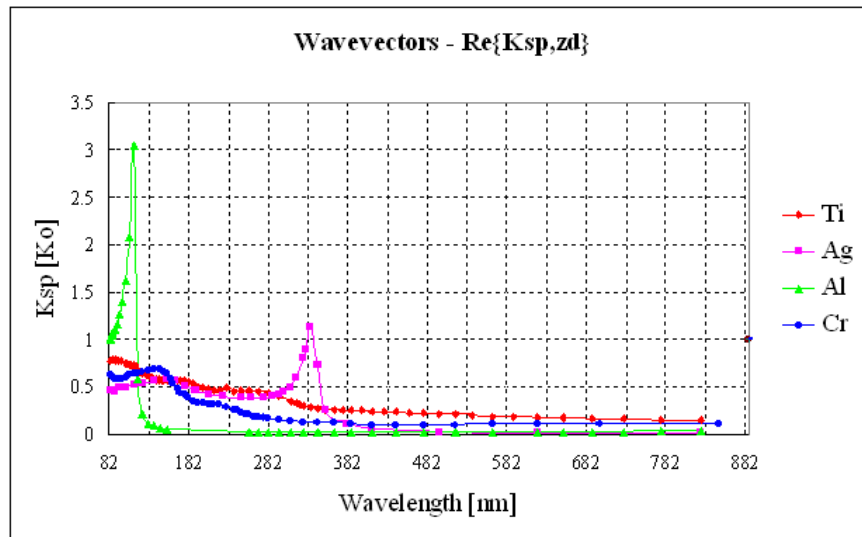


Fig. 2.4 (continued).

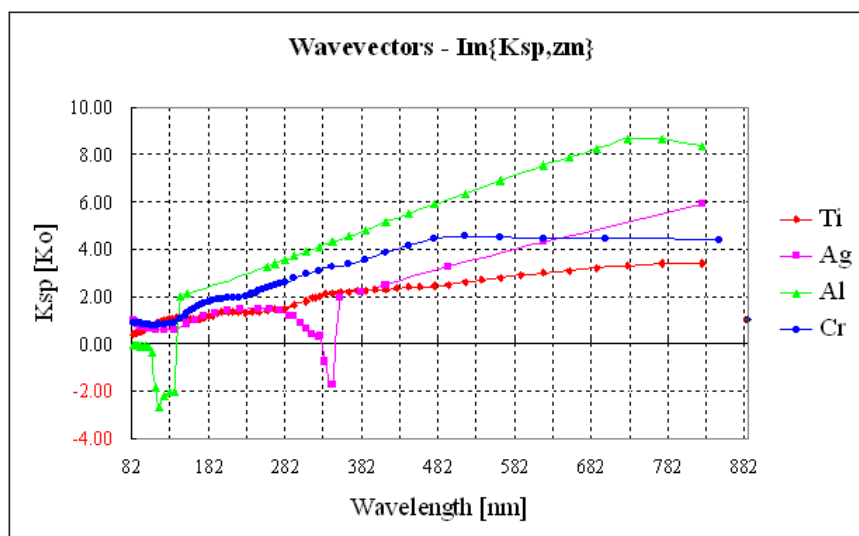
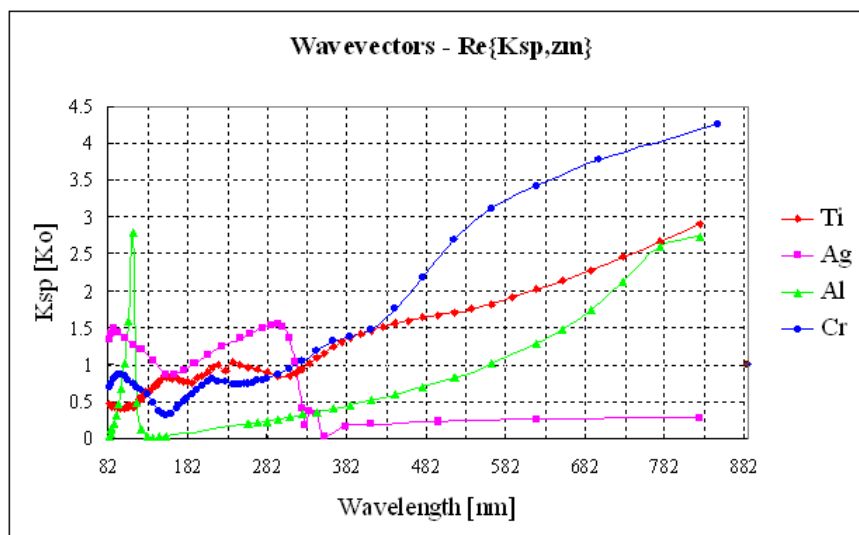


Fig. 2.4 (continued).

2.2 Design and Modeling of Optical Antenna

For simplicity, consider a 2D SP on the xz plane. Denote the z -axis as the optical axis and the x -axis as the lateral direction. Then the wave number of the SP in the x -direction is given by Eq. (2.8) where k_0 is the wave number of the light in free space, and ε_m and ε_d are the relative permittivity of the metal and dielectrics, respectively. In the spectra of interest, ε_m is a complex number whose real part is negative. The wavelength of the SP in the lateral direction is given by $\lambda_{sp,x} = 2\pi / \text{Re}\{k_{sp,x}\}$.

When the light frequency approaches the plasmon frequency of the metal, $\text{Re}\{k_{sp,x}\}$ can be significantly higher than k_0 ; so $\lambda_{sp,x}$ is much smaller than λ_0 , the light wavelength in free space. That is to say, the SP can have higher lateral resolution than the light due to its engineered large wavevector $k_{sp,x} (> k_0)$ achieved by selecting the absolute value of the negative dielectric constant of the metal matching the positive dielectric constant of the dielectrics.¹¹ Moreover, $\text{Im}\{k_{sp,x}\} \neq 0$, which means that SP decays exponentially in the lateral direction. This further reduces its spreading, resulting in even higher resolution.

However, the SP is also localized in the axial direction. Its wave number in the z -direction in the dielectric material is given by Eq. (2.10a). So the SP decays exponentially in the z -direction. For the most interesting plasmonic metals such as Au and Ag, the SP practically vanishes within $\lambda_0 / 2$. So the SP can't be used directly in proximity lithography. To this end, a propagating SP is needed, which can be obtained by disturbing the SP with apertures or nanoparticles.⁴³ We further conjectured that if an SP had a cylindrical or spherical symmetry, it should tend to converge or diverge. Thus, we constructed a plasmonic structure, named an "Optical Antenna" (OA), which consists of a set of concentric ring apertures in a metal film

deposited on a fused silica substrate. By illuminating the structure, the rings excite a cylindrical SP. The SP is then disturbed by the apertures and becomes a propagating wave that still has cylindrical symmetry and converges in the mid-field.

The design of an optical antenna (OA) is shown in Fig. 2.5. The width of the rings is a , and the inner and outer radii of the n -th ring are given by $R_{n,inner} = nr - a/2$ and $R_{n,outer} = nr + a/2$, respectively. In this section, we chose titanium as the metal to describe the design because it has a smaller imaginary term of $k_{sp,zd}$ than Ag or Au at $\lambda = 405$ nm. We simulated the optical field exiting a simple OA that has only one ring, $a = 150$ nm, $r = 3$ μ m, using TEMPEST, a FDTD Maxwell equation solver,⁴⁴ using four Itanium-2 processors on an SGI Altix 3700 supercomputer. To select the optimized a and r in a Ti film, we performed a number of numerical simulations by changing width and radius of ring, and thickness of the Ti film. Each node of the simulation domain was set as 20 nm ($\sim \lambda_0/20$). The dielectric constants of

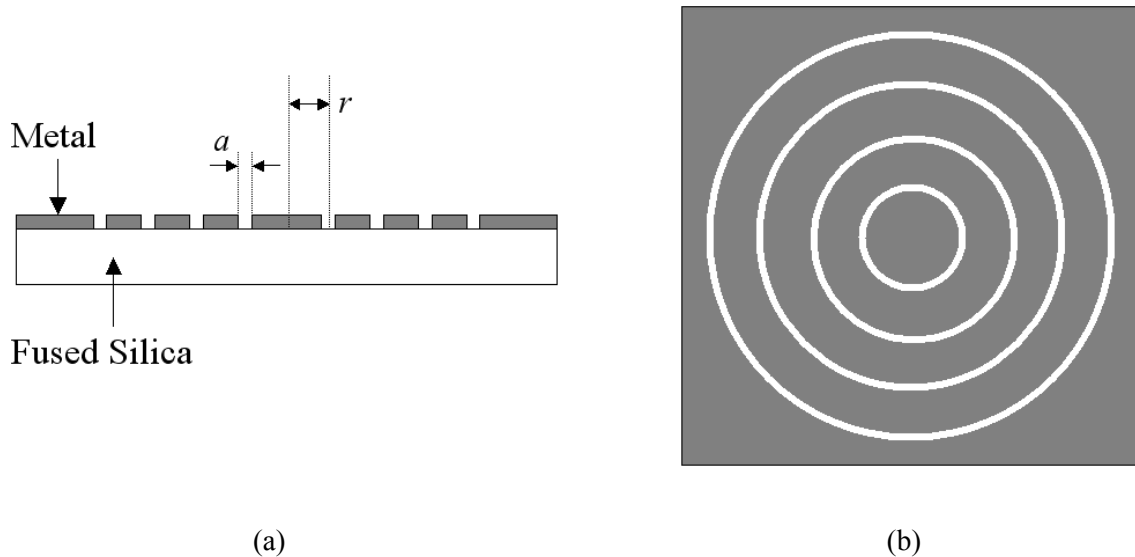


Fig. 2.5 Design of an Optical Antenna. (a) Cross-section (b) Top-down view

Ti and silica were chosen as $\epsilon_{Ti} = -2.22 + i6.66$ and $\epsilon_{Silica} = 2.16$, respectively.⁴⁵ The exit surface of the OA was placed on the plane $z = 0$. Assuming a circularly polarized coherent plane wave, $\lambda = 405$ nm, normally incident on the back side of the silica, the simulated light field is graphed in Fig. 2.6(a). It shows that the wave propagating along the optical axis has three axial maxima within the simulation domain, located at $z = 1.6, 2.2$, and 3.2 μm . The full width at half maximum (FWHM) of the beam at these axial maxima are 210 nm, comparable to a . The distance between an axial maximum and the exit surface of the OA is defined as its focal length. As in other optical systems, the light-field distribution on the image plane can be defined as its point-spread function (PSF). The PSF of a diffraction-limited system with a circular aperture pupil is known as the Airy pattern, and the diameter of the main lobe is given by $1.22\lambda / \text{NA}$ where NA is the numerical aperture.⁴⁶ The FWHM of the Airy pattern is $0.52\lambda / \text{NA}$. The normalized PSF of the OA on the focal plane $z = 1.6, 2.2$, and 3.2 μm are compared in Fig. 2.6(c). The FWHM of this simple OA at $z = 3.2$ μm is calculated as 210 nm, equivalent to 0.52λ , indicating that the OA is equivalent to a lens with $\text{NA}=1$. But the side lobes are higher than the Airy pattern, indicating energy leakage from the main lobe. This effect also appears in the apodization.³ Fig. 2.6(b) graphs the light field on the exit surface of the OA. The light transmitting through the rings excites cylindrical SP waves, and the interference of the SP waves with the zero-order transmitted wave forms a circular standing-wave pattern, shown as the many concentric rings in the graph. In a cylindrical coordinate system (r, θ, z) , the SP has a magnetic field along the θ -axis, and an electric field along the r and z axes. The components of the SP are given by:⁴⁷

$$H_{sp,\theta} = [C_1 H_1^{(1)}(k_{sp,r}) + C_2 H_1^{(2)}(k_{sp,r})] \exp(ik_{sp,z}z) \quad (2.11a)$$

$$E_{sp,r} = \frac{k_{sp,z}}{\omega\epsilon} H_{sp,\theta} \quad (2.11b)$$

$$E_{sp,z} = \frac{i}{\omega\epsilon} \left(\frac{H_{sp,\theta}}{r} + \frac{\partial H_{sp,\theta}}{\partial r} \right) \quad (2.11c)$$

where $k_{sp,r}$ and $k_{sp,z}$ are the SP wave numbers in the r and z directions, respectively;

$k_{sp,r} = k_0 \sqrt{\epsilon_m \epsilon_d / (\epsilon_m + \epsilon_d)}$, and $k_{sp,zd} = k_0 \epsilon_d / \sqrt{\epsilon_m + \epsilon_d}$ is given by Eq. (2.10a). $H_1^{(1)}$ and

$H_1^{(2)}$ are the Hankel functions of the first and second kind, corresponding to outward and

inward travelling cylindrical waves, respectively. C_1 and C_2 are the amplitudes. Due to the

film thickness and apertures, there also exist a zero-order transmitted wave and wavelets directly

transmitted through the apertures. The resulting field in air, shown in Fig. 2.6(a), is the

summation of the fields diffracted by the apertures and the disturbed propagating SP.

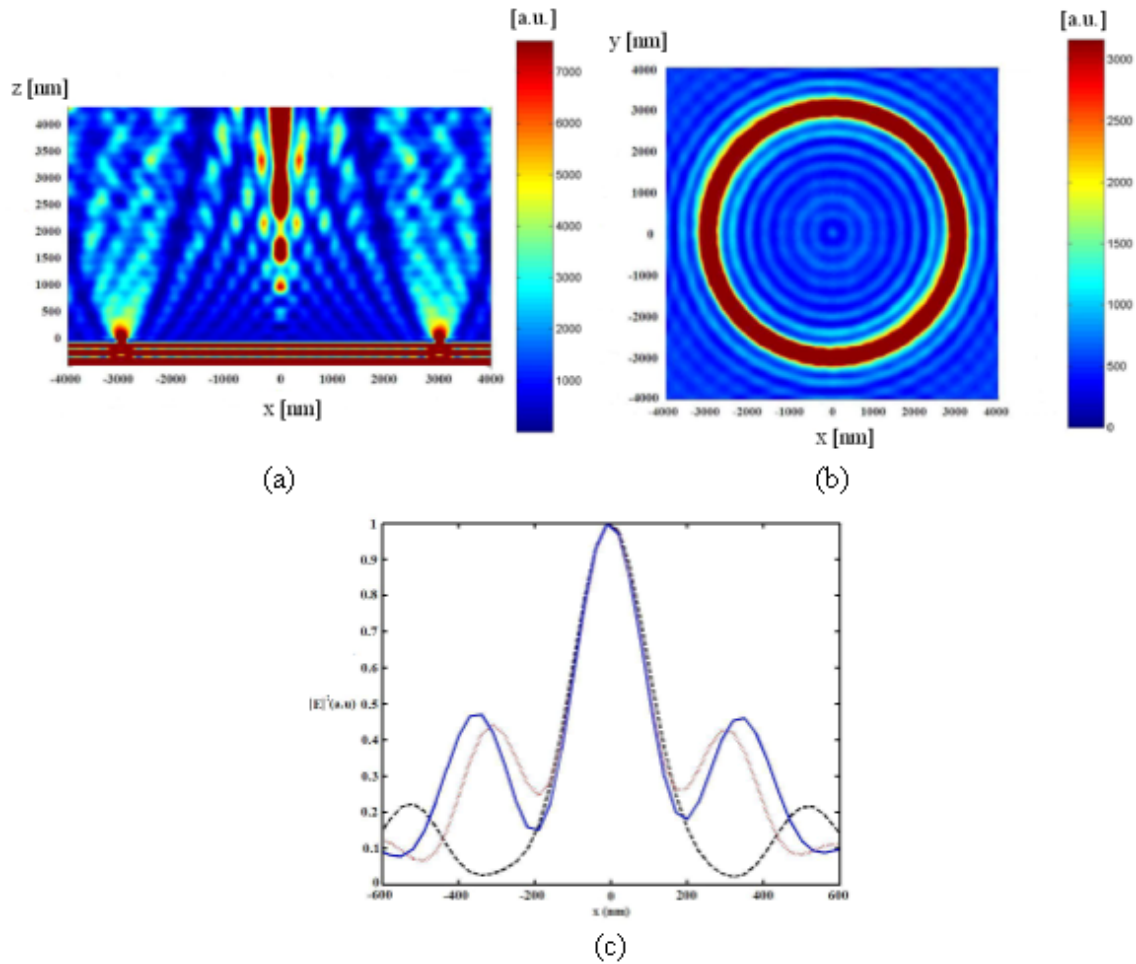


Fig. 2.6 Simulations of the Optical Field. (a) optical field exiting a plasmonic lens and (b) light field on the exit plane of this PL. The PL has one ring, $a = 150$ nm, $r = 3$ μm . (c) Comparison of the PSF at different planes, $z=1.6$ μm (black dashed line), 2.2 μm (red dotted line), and 3.2 μm (blue solid line).

2.3 Finite-Difference-Time-Domain (FDTD) Simulation

2.3.1 Methodology

To help understand the behavior of the optical antenna (OA), we simulated the optical field around the OA by using ‘TEMPEST (version 6.0) – Time-domain Electromagnetic

Massively Parallel Evaluation of Scattering from Topography' which was developed by the 'Electronic Research Laboratory' of University of California, Berkeley. TEMPEST solves Maxwell's equation using a time-domain-finite-difference algorithm, where the electric and magnetic field nodes are spatially and temporally staggered over a three dimensional topography of interest.⁴⁴ Illumination is assumed to be monochromatic and coherent as 405 nm wavelength violet laser throughout the whole simulations. TEMPEST parses topography information of an input file which can be checked for errors. The input file is calculated until the electromagnetic (EM) field reaches steady-state or user set number of wave cycles. After collecting calculation information of the geometry from an input file (see an example in Appendix B), TEMPEST writes an output file, topography, and field data to be analyzed by numerical computing tool such as MATLAB.

The design of the optical antenna described in 2.1.1.3 is based on four ring structures which can scatter and induce EM fields. Since the optical field simulation of the design is too computationally expensive to do, we focus on a simple OA composed of a ring. The exit surface of the OA was placed on the z -plane, so z is the optical axis. Assuming a circularly polarized coherent plane wave, $\lambda = 405$ nm, normally incident upon the back side of the silica, the simulated light fields are graphed and analyzed by using MATLAB script files `plotam6.m`, `plotbin.m` and `fwhm.m` (Appendix C).

The 3D simulation domain was set as $8 \mu\text{m} * 8 \mu\text{m} * 6 \mu\text{m}$ in xyz directions and each node of the simulation domain was set as 20 nm ($\sim \lambda_0 / 20$) or 30 nm ($\sim \lambda_0 / 14$) depending on simulation needs. To compute those massive 3D simulation works, four Itanium-2 processors on an SGI Altix 3700 supercomputing system of Supercomputing Facility of Texas A&M University and two Intel Xeon E7500 processors in a work station system were used.

Inserting two Perfectly Matching Layers (PML) on the domain borders ($z = 0$ and $z = 6 \mu\text{m}$) allow for the simulation of fully isolated topographies, i.e., it eliminates the light artificially reflected from the simulation boundaries.

2.3.2 Light after a Sub-Wavelength Hole

In a diffraction-limited system, if an incident wavelength is larger than an aperture, the waves will diverge with a large angle into the region beyond the aperture. The smaller the aperture is, the larger the divergence angle. In case of a circular aperture described in Fig. 2.7(a), the diffraction irradiance can be written as a function of θ ,⁴⁸

$$I(\theta) = I(0) \left[\frac{2J_1(ka \sin \theta)}{ka \sin \theta} \right]^2 \quad (2.12)$$

where $J_1(x)$, k , a , and θ are Bessel Function, wavevector, aperture radius, and irradiation angle, respectively. From the reference,⁴⁸ $J_1(x) = 0$ when $x = 0$, that is $kaq / R = 3.83$. Eq. (2.12) can be plotted as Fig. 2.7(b) and known as the Airy disk. The diameter (D_1) of the main lobe in Fig. 2.7(b) is given by

$$D_1 = 2q = 2 \cdot 1.22 \frac{R\lambda}{2a} = 1.22 \frac{\lambda}{NA} \quad (2.13)$$

where NA is the numerical aperture. Thus, the FWHM (Full-Wave-at-Half-Maximum) of the first Airy pattern is $0.52\lambda / NA$.

As predicted in conventional optics,¹⁴ a wave which is larger than an aperture is diffracted and can't propagate from the obstruction. However, this theory ignored the fact that the surface plasmon (SP) waves created at the interface between a metal and dielectric layer can provide much smaller wavelength. From the Appendix A and Eq. (2.8), real values of the SP wavevectors $k_{sp,x}$ in different metals are $1.109k_0$ (Ag), $1.020k_0$ (Al), $1.022k_0$ (Cr), and $1.014 k_0$ (Ti) at 405nm incident wave with air interfaces. In other words, new SP wavelengths to the

surface direction at the interfaces are 365 nm (Ag), 397 nm (Al), 396 nm (Cr), and 399 nm (Ti), and those are identical to the numerical simulation results shown in Fig. 2.8. The incident wavelength (405 nm) by the metal/dielectric is engineered to be small and the propagation of SP waves to the metal surface direction from the circular aperture exit follows the $\Lambda = 1/\text{Im}\{k_{sp,x}\}$ relation with calculated $\text{Im}\{k_{sp,x}\}$ values of 0.026 (Ag), 0.004 (Al), 0.023 (Cr), and 0.067 (Ti) in Appendix A. As clearly seen in Fig. 2.8, Al provides the longest SP propagation length in air interface condition.

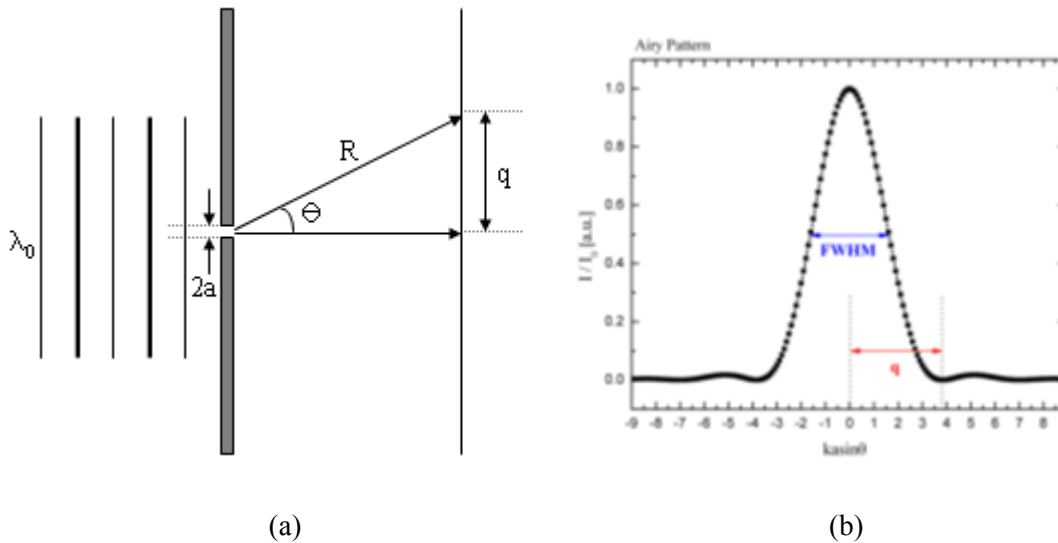


Fig. 2.7 (a) Circular Aperture Geometry (b) The Airy Pattern.

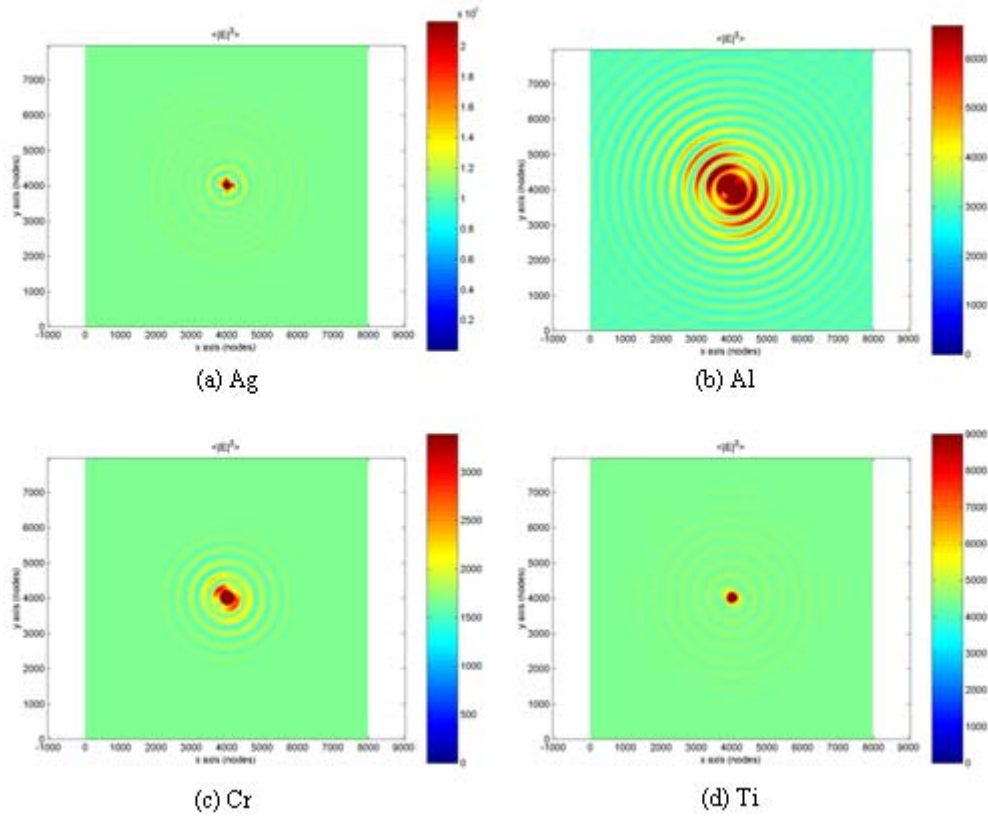


Fig. 2.8 Surface Waves Passing Through a Sub-Wavelength Hole. (diameter of 150 nm) in highly conductive metals (thickness of 60 nm), (view from XY-plane at $Z = 20$ nm. $Z = 0$ is the interface between a metal and dielectric).

To understand light interaction with a tiny hole in highly conductive metals, we conducted a number of simulations as illustrated in Appendix D.1. Simulation parameters include materials (Ag, Al, Cr, and Ti), diameters of the holes (W ; 50 nm, 100 nm, and 150 nm), and thickness of metals (T ; 60 nm, 100 nm, 150 nm, and 200 nm). The dielectric constants of the metals (Ag, Al, Cr, and Ti) and dielectric (silica) were chosen as $\epsilon_{Ag} = -5.10 + i1.04$, $\epsilon_{Al} = -24.97 + i5.26$, $\epsilon_{Cr} = -11.39 + i11.43$, $\epsilon_{Ti} = -2.18 + i6.90$ and $\epsilon_{Silica} = 2.16$, respectively.⁵⁶ All the results, viewed from XZ-plane, are contained in Appendix D.1. Each hole was located at the center of the simulation domain, i.e., $x = 4000$ nm and $y = 4000$ nm.

Fig. 2.9 shows the electric field intensity distribution after a sub-wavelength hole (diameter of 150 nm) in highly conductive metals (thickness of 60 nm). To find out light propagation in dielectric material ($z > 0$), light field intensity data of XY-planes cut at $z = 0, 200$ nm, 400 nm, and 1,000 nm were plotted. As seen in Fig. 2.9(a), over 80% of the light vanished within a half of incident wavelength (~ 200 nm) after the hole in silver (Ag) and nearly no propagation observed at $z = 1 \mu\text{m}$ plane. This decaying property was similar to all other metals, such as aluminum in (b), chromium in (c), and titanium in (d) except that the amounts of transmissions are slightly different. Metals illustrated in Fig. 2.9 were set as thickness of 60 nm. This thickness is not enough to block all the light, so some of the light were transmitted through the metal directly. Fig. 2.10 shows the electric field intensity $\langle |E|^2 \rangle$ comparison at the exit of a 150 nm diameter hole in different metals at $Z = 0$. Ag transmits the incident light more than 10 times than other metals at 405 nm as compared in Fig. 2.10.

A single hole aperture in conductive metals can excite SP mode in surface as shown in Fig. 2.8, however, it is not adequate to make a focused tiny spot at several wavelengths away from metal surface in air.

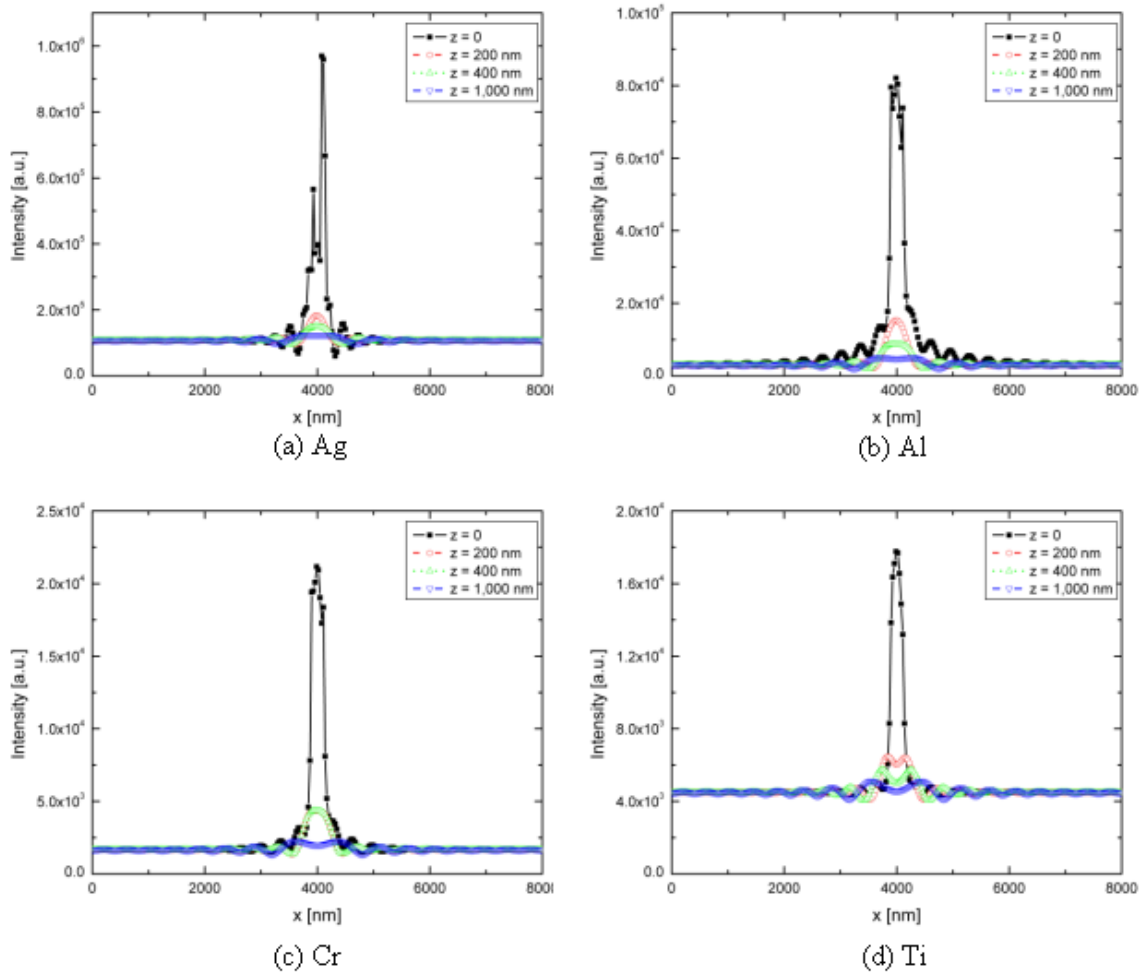


Fig. 2.9 Electric Field Intensity $\langle |E|^2 \rangle$ Distribution After a Sub-Wavelength Hole. (diameter of 150 nm located at (4000 nm, 4000 nm) in XY-coordinate) in highly conductive metals (thickness of 60 nm), (view along with X-axis at Z = 0, 200, 400, and 1,000 nm above the metal).

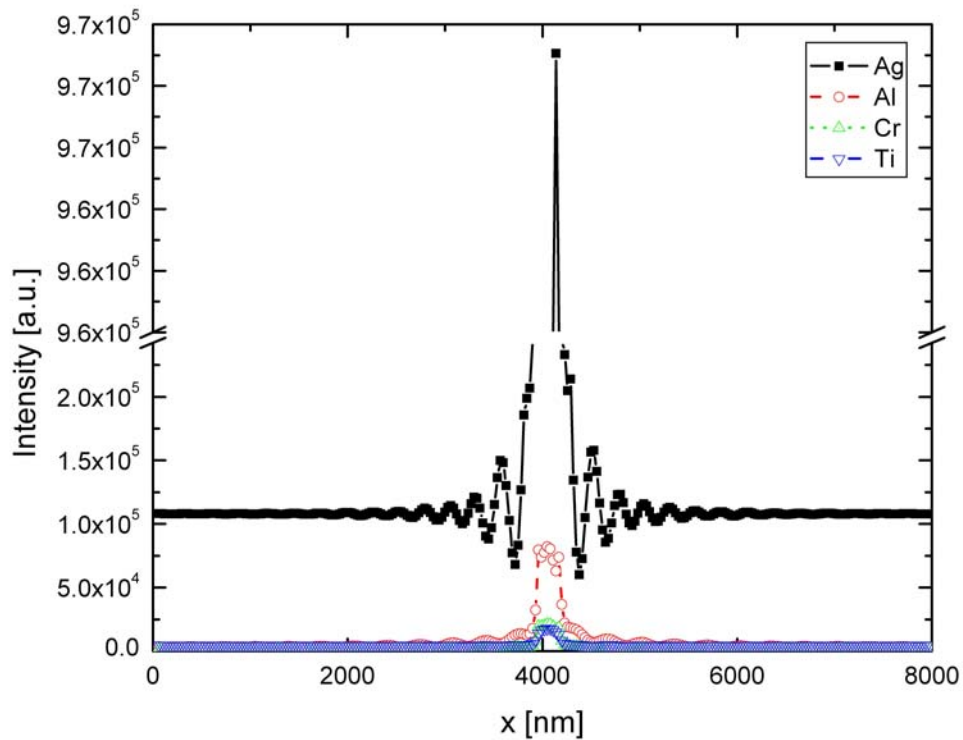


Fig. 2.10 Electric Field Intensity $\langle |E|^2 \rangle$ Comparison at the Exit of a Sub-Wavelength Hole. (diameter of 150 nm) in highly conductive metals (thickness of 60 nm), (view along with X-axis at $Z = 0$).

2.3.3 Light after a Tiny Ring

To make a sub-wavelength focus far from the metal in an interfacing dielectric medium (air in this dissertation), we employed a cylindrical aperture, i.e., a ring shape, as we discussed in section 2.2. We performed a number of FDTD simulations which include variables of four highly conductive metals (Ag, Al, Cr, and Ti), three different radii of the simple ring ($R = 1 \mu\text{m}$, $2 \mu\text{m}$, and $3 \mu\text{m}$), three different widths of the ring ($W = 50 \text{ nm}$, 100 nm , and 150 nm), and four different thicknesses of the metals ($T = 60 \text{ nm}$, 100 nm , 150 nm , and 200 nm) as shown in Appendix D.2. We focused on a simple ring structure, e.g. $n = 1$, because of the computational

resource limit. In this section, we provide a case study for each material showing the best result for our original purpose. Before we proceed to case studies on various materials, we note that Ag has the biggest $k_{sp,x}$ which means the smallest surface plasmon wavelength and Al can provide the biggest propagation in the dielectric at the given wavelengths (Table 2.1).

Table 2.1 Wavevectors on Case Studied Materials with Air Interface.

$\lambda_0 = 405$ [nm]	$k_{sp,x}$ [\mathbf{k}_0]		$k_{sp,zd}$ [\mathbf{k}_0]		$k_{sp,zm}$ [\mathbf{k}_0]	
	Real	Imaginary	Real	Imaginary	Real	Imaginary
Ag	1.109	0.026	0.061	-0.482	0.195	2.523
Al	1.020	0.004	0.022	-0.201	0.512	5.125
Cr	1.022	0.023	0.103	-0.233	1.487	3.827
Ti	1.014	0.069	0.244	-0.289	1.462	2.312

Silver (Ag) is one of the heavily studied metamaterials for the nanolithography and super-resolution imaging by exciting SP.^{6-9, 11-12, 14-15, 21} However, the Ag is not a good choice in terms of the propagation (+z-direction) in the air (refractive index of 1) at 405 nm incident wavelength as compared in Table 2.1. Nevertheless, Ag has a slightly larger $k_{sp,x}$ than k_0 which is equivalent to $\lambda_{sp,x} = 365$ nm. The dielectric constants of Ag and silica were chosen as $\epsilon_{Ag} = -5.10 + i1.04$ and $\epsilon_{Silica} = 2.16$, respectively.⁴⁹

Fig. 2.11(a) and (b) show the electric field intensity passing through a simple Ag optical antenna in XZ ($y = 4,000$ nm) and XY ($z = 20$ nm) planes. The radius and width of the simple ring were set as 3 μm and 100 nm, respectively, and the thickness of the Ag was 100 nm. Fig. 2.11(c) illustrates a distribution of the refractive indices used in this simulation node. From this simulation, we could see six intensity maxima in the air focused at $z = 40$ nm, 460 nm, 1030 nm, 1720 nm, 2710 nm, and 4600nm within a 6000 nm z-axis domain. The smallest beam diameter

in full-wave-at-half-maximum (FWHM) was estimated as 250.79 nm at $z = 3290$ nm which is equivalent to $NA = 0.89$ ($NA = 1$ is a perfect lens) where NA is the numerical aperture (Fig. 2.12). $z' = 0$ is a zero point of z -axis of the whole simulation domain, but all the z -data mentioned here are based on a new zero point at which the interface between the metal and dielectric is located.

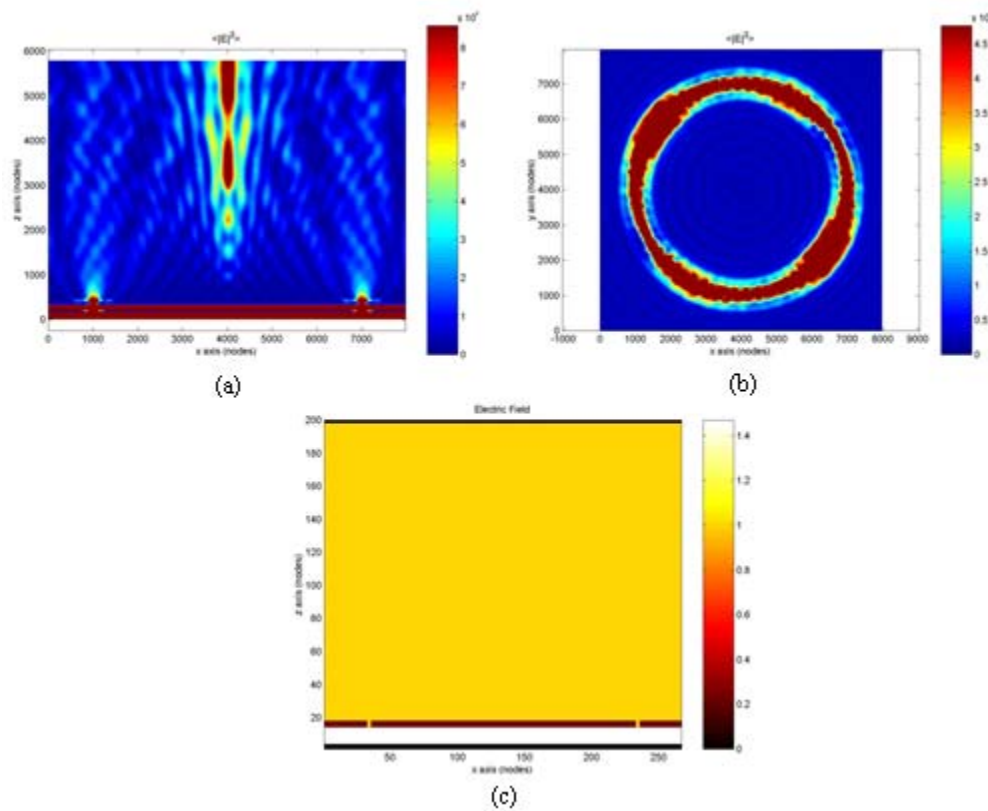
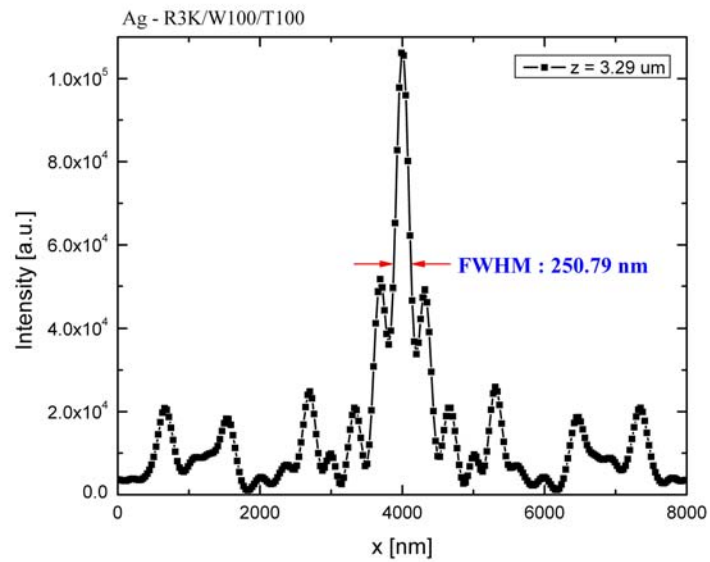
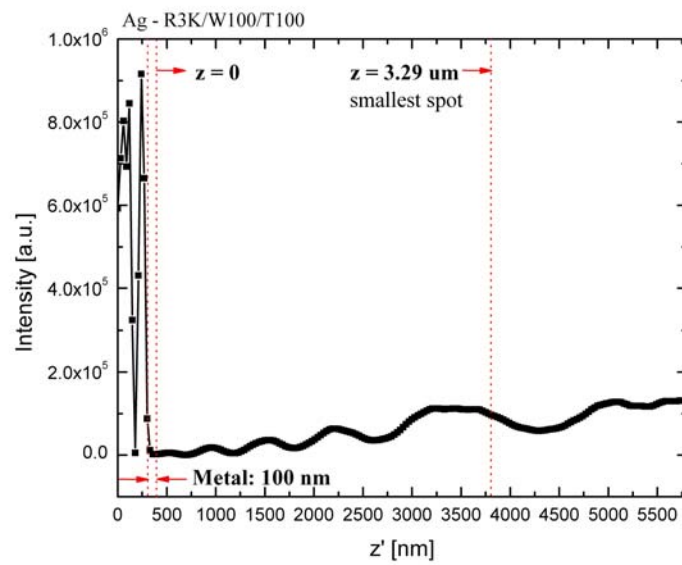


Fig. 2.11 Light Field Passing Through a Simple Ag Ring Aperture. (a) Electric field intensity in XZ-plane ($y = 4000$ nm) (b) Electric field intensity in XY-plane ($z = 20$ nm) (c) Refractive indices.



(a)



(b)

Fig. 2.12 Light Intensity Distribution of a Simple Ag Ring Aperture. (a) along with x-axis at $y = 4000$ nm and $z = 3.29$ μm (b) along with z-axis at $x = y = 4000$ nm.

For Al, $k_{sp,x} = 1.020$ which is equivalent to $\lambda_{sp,x} = 397$ nm and the dielectric constant of Al was chosen as $\epsilon_{Al} = -24.97 + i5.26$. Fig. 2.13(a) and (b) show the electric field intensity passing through a simple Al optical antenna in XZ ($y = 4,000$ nm) and XY ($z = 20$ nm) planes. The radius and width of the simple ring were set as $3 \mu\text{m}$ and 100 nm, respectively, and the thickness of the Al was 60 nm. Fig. 2.13(c) illustrates a distribution of the refractive indices used in this simulation node. From this simulation, we could see six intensity maxima in the air focused at $z = 440$ nm, 1010 nm, 1700 nm, 2720 nm, 4520 nm, and 5120 nm within the 6000 nm z -axis domain. The smallest beam diameter (FWHM) was estimated as 232.74 nm at $z = 3360$ nm which is equivalent to $\text{NA} = 0.96$ (Fig. 2.14).

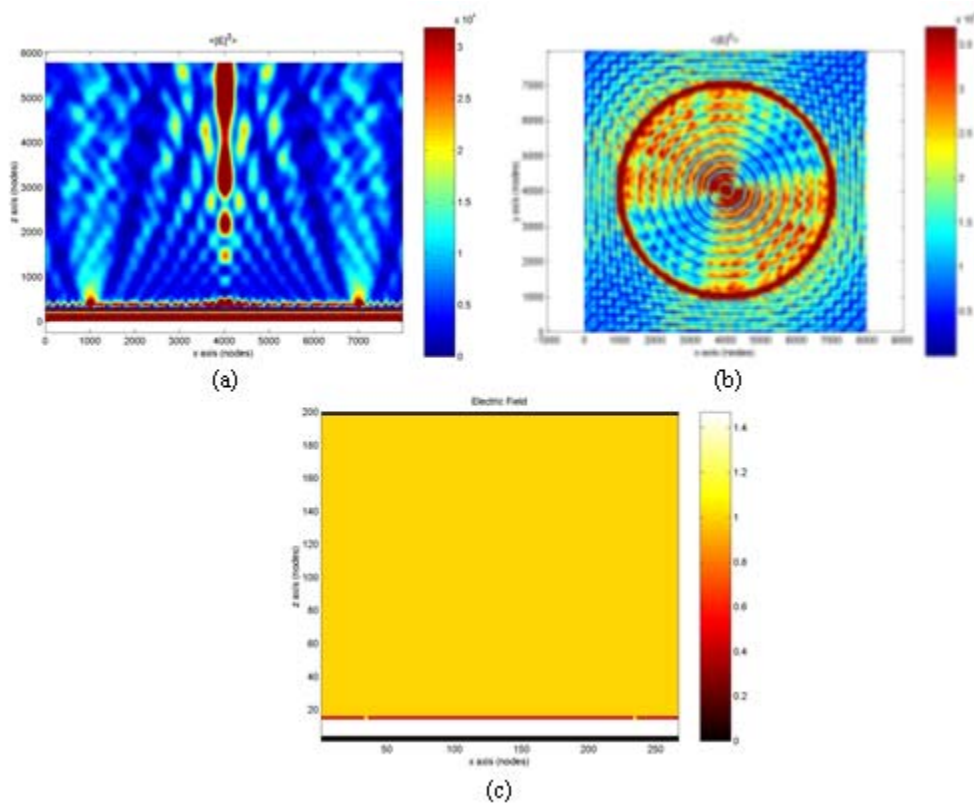
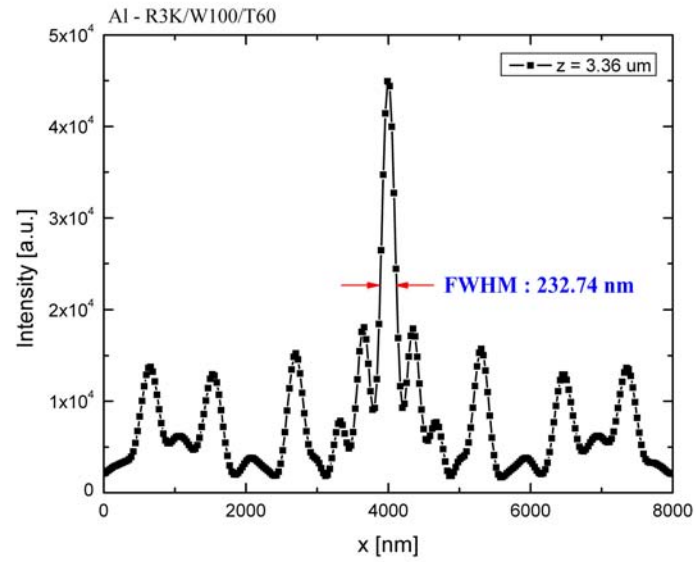
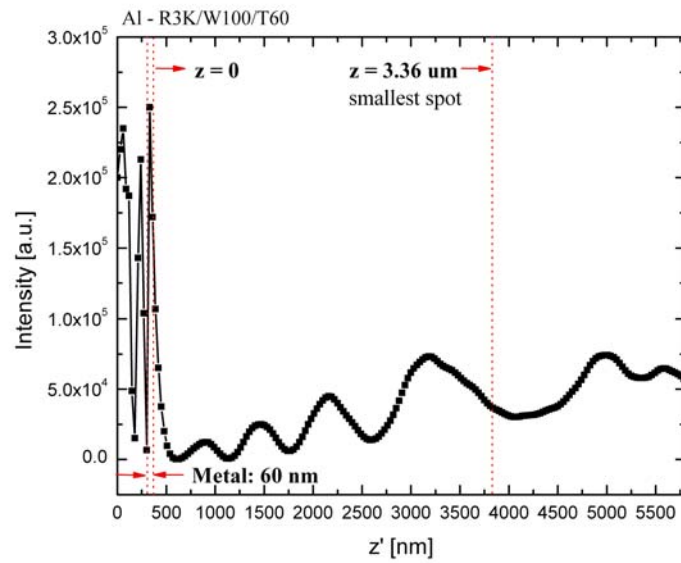


Fig. 2.13 Light Field Passing Through a Simple Al Ring Aperture. (a) Electric field intensity in XZ-plane ($y = 4000$ nm) (b) Electric field intensity in XY-plane ($z = 20$ nm) (c) Refractive indices.



(a)



(b)

Fig. 2.14 Light Intensity Distribution of a Simple Al Ring Aperture. (a) along with x-axis at $y = 4000$ nm and $z = 3.29$ μm (b) along with z-axis at $x = y = 4000$ nm.

For Cr, $k_{sp,x} = 1.022$ which is equivalent to $\lambda_{sp,x} = 396$ nm and the dielectric constant of Cr was chosen as $\epsilon_{Cr} = -11.39 + i11.43$. Fig. 2.15(a) and (b) show the electric field intensity passing through a simple Cr optical antenna in XZ ($y = 4,000$ nm) and XY ($z = 20$ nm) planes. The radius and width of the simple ring were set as $3 \mu\text{m}$ and 100 nm, respectively, and the thickness of the Cr was 60 nm. Fig. 2.15(c) illustrates a distribution of the refractive indices used in this simulation node. From this simulation, we could see five intensity maxima in the air focused at $z = 380$ nm, 920 nm, 1640 nm, 2690 nm, and 4400 nm within the 6000 nm z -axis domain. The smallest beam diameter (FWHM) was estimated as 275.56 nm at $z = 2700$ nm which is comparable to $\text{NA} = 0.81$ (Fig. 2.16).

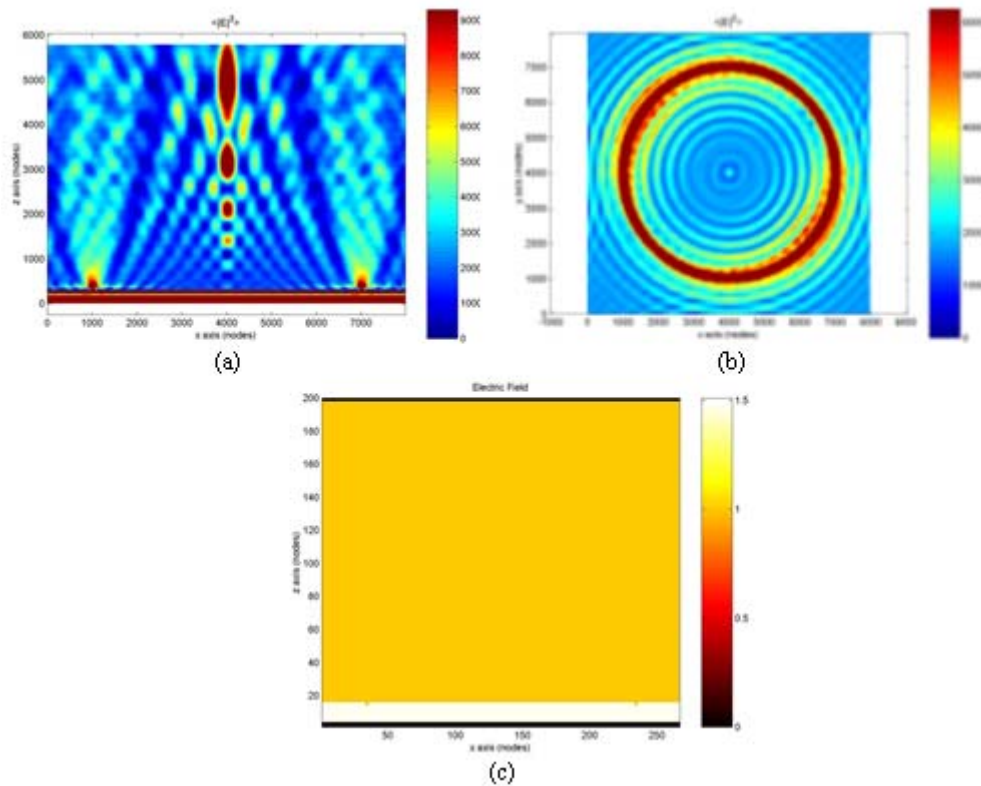
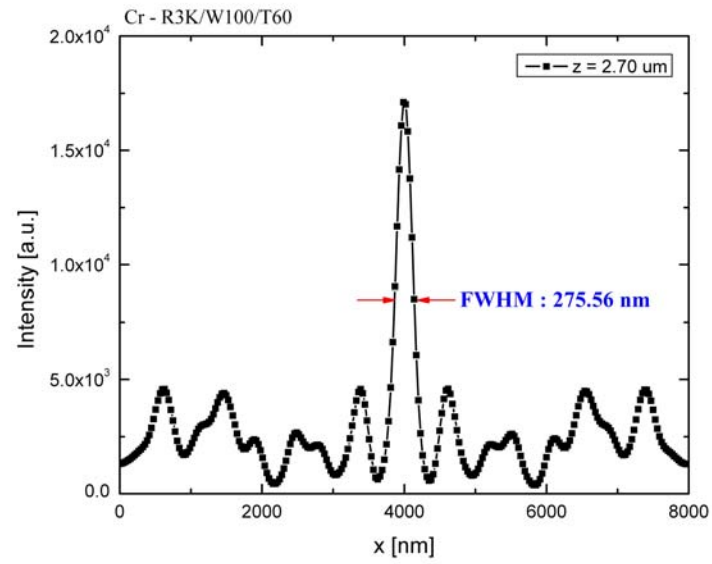
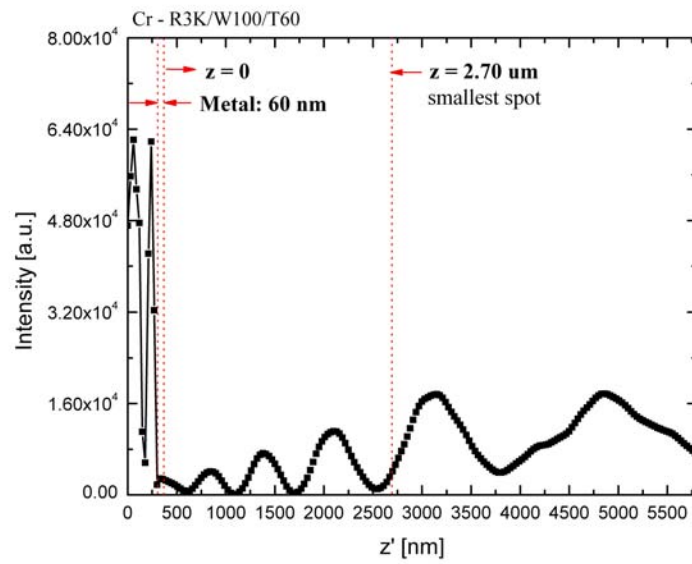


Fig. 2.15 Light Field Passing Through a Simple Cr Ring Aperture. (a) Electric field intensity in XZ-plane ($y = 4000$ nm) (b) Electric field intensity in XY-plane ($z = 20$ nm) (c) Refractive indices.



(a)



(b)

Fig. 2.16 Light Intensity Distribution of a Simple Cr Ring Aperture. (a) along with x -axis at $y = 4000 \text{ nm}$ and $z = 3.29 \mu\text{m}$ (b) along with z -axis at $x = y = 4000 \text{ nm}$.

For Ti, $k_{sp,x} = 1.014$ which is equivalent to $\lambda_{sp,x} = 399$ nm and the dielectric constant of Ti was chosen as $\epsilon_{Ti} = -2.18 + i6.90$. Fig. 2.17(a) and (b) show the electric field intensity passing through a simple Ti optical antenna in XZ ($y = 4,000$ nm) and XY ($z = 20$ nm) planes. The radius and width of the simple ring were set as $3 \mu\text{m}$ and 150 nm, respectively, and the thickness of the Ti was 100 nm. Fig. 2.17(c) illustrates a distribution of the refractive indices used in this simulation node. From this simulation, we could see six intensity maxima in the air focused at $z = 340$ nm, 850 nm, 1510 nm, 2500 nm, 3430 nm, and 4390 nm within the 6000 nm z -axis domain. The smallest beam diameter (FWHM) was estimated as 237.54 nm at $z = 2340$ nm which is equivalent to $\text{NA} = 0.94$ (Fig. 2.18).

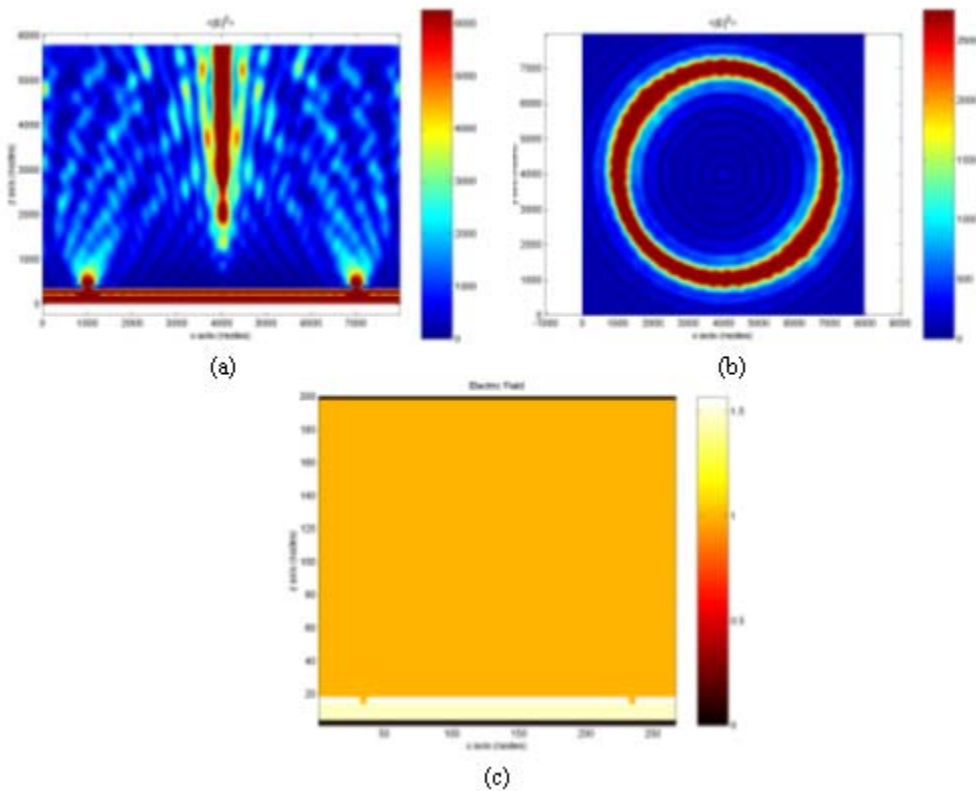
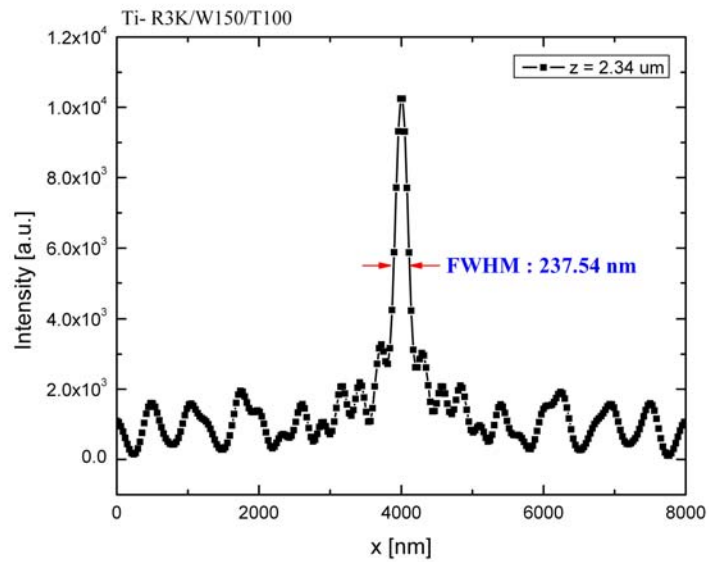
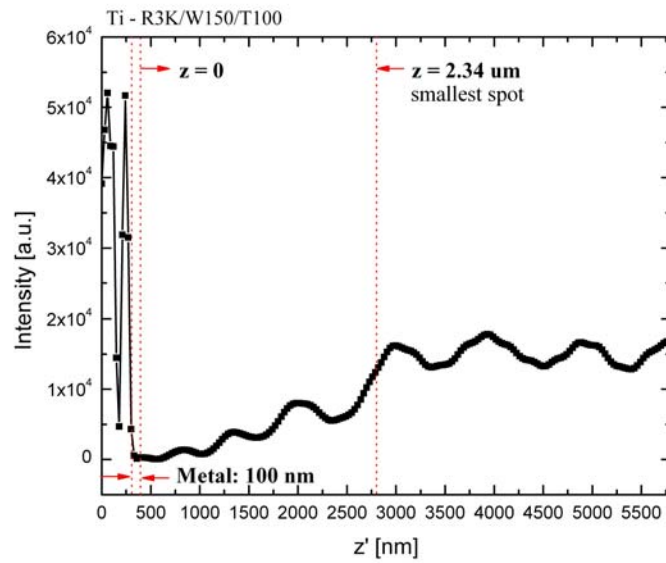


Fig. 2.17 Light Field Passing Through a Simple Ti Ring Aperture. (a) Electric field intensity in XZ-plane ($y = 4000$ nm) (b) Electric field intensity in XY-plane ($z = 20$ nm) (c) Refractive indices.



(a)



(b)

Fig. 2.18 Light Intensity Distribution of a Simple Ti Ring Aperture. (a) along with x-axis at $y = 4000$ nm and $z = 3.29$ μm (b) along with z-axis at $x = y = 4000$ nm.

CHAPTER III

PLASMONIC NANOLITHOGRAPHY - EXPERIMENT

3.1 Device Fabrication and Experiment Apparatus

To fabricate the OA structure designed and modeled in chapter II, first a 100 nm thick Ti film was deposited on a fused silica substrate via DC sputtering with 3200 V / 40 μ A under the pressure of 2×10^{-6} torr and an UV5 resist (Shipley) was spun on the Ti. The spinning took 60 s at 5000 rpm, followed by soft baking for 60 s on a 135°C hotplate, which resulted in a 120 nm thick resist layer. Next, electron beam lithography (JEOL T330 adapted for EBL) was performed with 0.04 μ C / cm line dosage to write the apertures in the resist. The substrate, then, was post exposure baked for 90 s at 135°C on the hotplate and developed in the mixture of MF312 : H₂O (1 : 1.2) for 30 s. A 10 min hard baking in the 130°C convection oven was done for the better etching selectivity before anisotropically etched by reactive ion etching (RIE) in the pressure of 1.2×10^{-5} torr with Ar (3 sccm) / CHF₃ (30 sccm) / He (7.5 sccm) gases for 6.5 min at 350 W power. Finally, the resist layer was stripped by AZ300T at 95°C for 15 min. Fabrication processes are illustrated in Fig. 3.1, and Fig. 3.2 shows a scanning electron micrograph (SEM) of an OA fabricated, which has 4 rings in a 100 nm thick Ti film with the parameters of $a = 150$ nm and $r = 3$ μ m.

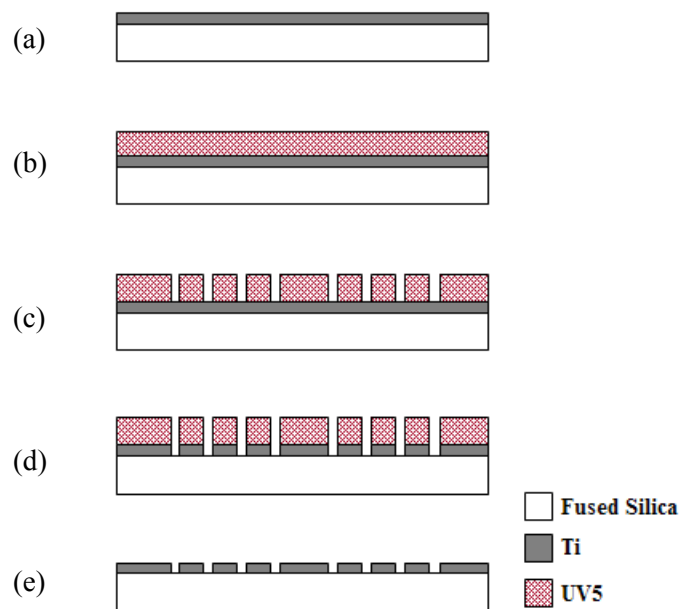


Fig. 3.1 Optical Antenna Fabrication Processes. (a) Ti Deposition by DC Sputtering, (b) Spin Coating an UV5 on a Ti Layer, (c) Definition of the Ring Apertures by Electron Beam Lithography, (d) Reactive Ion Etching for the Ti, and (e) Stripping the UV5 Resist.

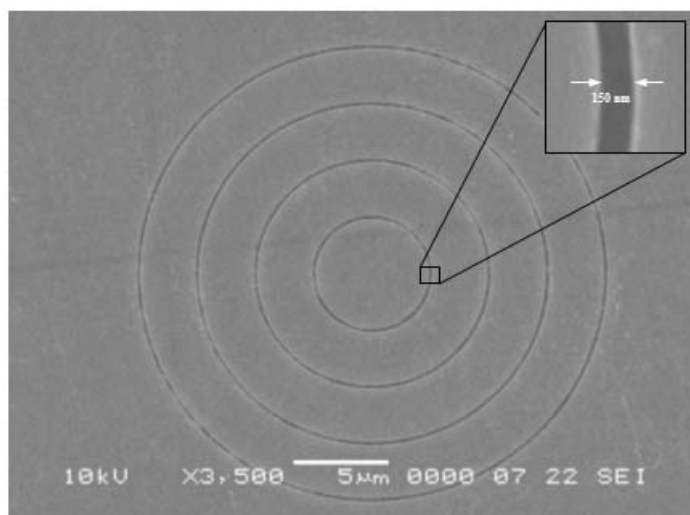


Fig. 3.2 Scanning Electron Micrograph (SEM) of the Fabricated Optical Antenna. Composed of four ($n=4$) equally spaced ($r = 3 \mu\text{m}$) rings in a 150nm ($a = 150 \text{nm}$) width.

A plasmonic nanolithography system, depicted in Fig. 3.3, was built to evaluate the OA. A silicon wafer spin-coated with S1805 (S1805 : PGMEA = 2 : 1) positive resist (200 nm thick at 7500 rpm for 40 s) diluted with PGMEA (Propylene Glycol Methyl Ether Acetate) was mounted on a 6-axis nanopositioning stage (NanoMax-HS, Melles Griot). The OA was mounted above the wafer by a stable sample post. A 5 mW violet laser ($\lambda = 405$ nm) was used to expose the resist through the OA, and a red light emitting diode (LED) (peak wavelength 650 nm) was used with a CCD camera to observe and align the wafer / OA.

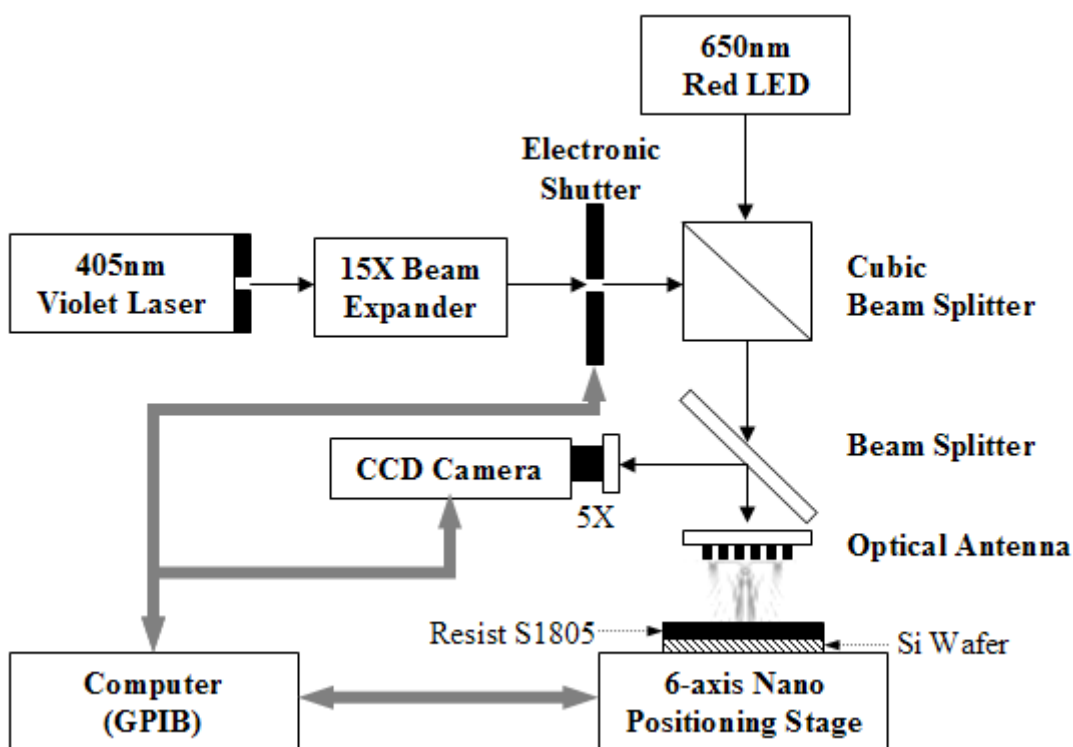


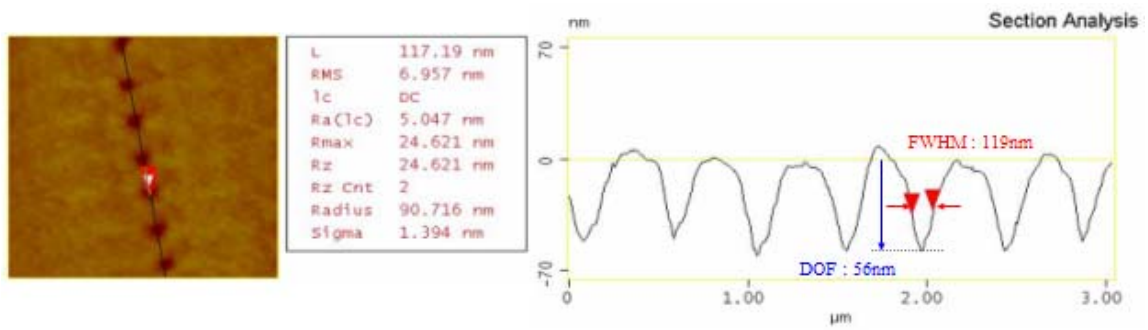
Fig. 3.3 Experiment Apparatus to Record the Optical Field Emanating from an Optical Antenna. A gap of micrometer size is maintained between the OA and the resist by computer controlled 6-axis nano-positioning stage.

Before exposure, the gap between the OA and the wafer was calibrated under the

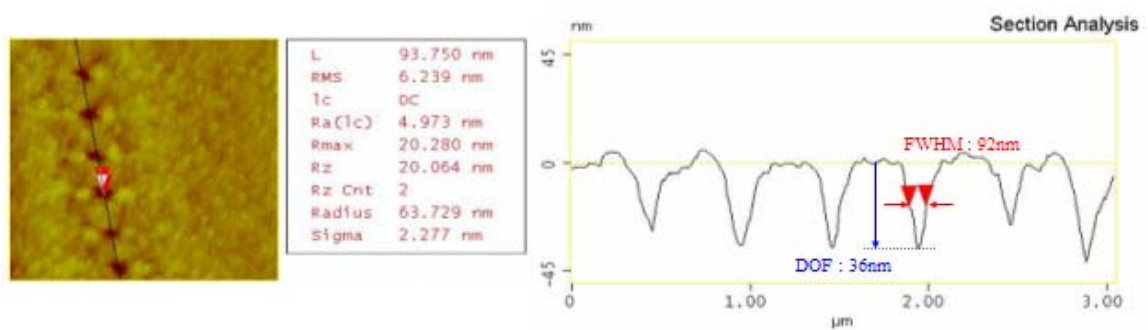
illumination of the red LED. ‘Si Wafer - OA - Beam Splitter - CCD Camera’ setup can be considered as a Michelson interferometer using a quasi-monochromatic illumination.⁵⁰ We first made the OA and wafer in firm contact by tuning the z-axis and observing the fringe patterns until the fringe pattern became uniform under the control of $\theta_{x,ROLL}$ and $\theta_{y,PITCH}$. Then the gap was adjusted to the desired value by tuning the z-axis of the stage. And a step-and-expose process was conducted to print the desired pattern. The nano-positioning stage moved the wafer to a next position and the electronic shutter was turned on for certain time to expose each spot. The stage, then, moved to the next position and timed the shutter again. This process was repeated till all the desired spots were exposed. After developing the resist in the diluted MF312 (MF312 : H₂O = 1 : 1.2) about 10 ~ 15 s, the spot patterns provided ‘snapshots’ of the PSF on the image plane.

3.2 Experiment Results

Fig. 3.4 shows the exposure experiment results. Fig. 3.4(a) is the atomic force micrographs (AFM) of the pattern written by this OA. Each spot was exposed with 0.13 mJ/cm² dosage and the centre-to-centre spacing between the spots was 300 nm. The gap between the OA and the resist, i.e. the WD, was 1.7 μ m. Note that this WD was also a focal length of the PL. Fig. 3.4(b) shows the section analysis of one of the exposed spots. The spot size (FWHM) was measured and averaged as 92 nm through over 100 exposures. Thus the AFM measurement clearly evidences that the OA focuses a beam much narrower than the diffraction limit. Fig. 3.4(a) and (b) indicate that the higher exposed energy (0.17 mJ/cm²) widens spot size to 119 nm, but could improve the Depth-Of-Field (DOF) from 36 nm to 56 nm and Fig. 3.5 shows that an expose dosage (0.25 mJ/cm²) could be used to print different period spots which have 300 nm, 400 nm, and 500 nm in a spot array.⁶³



(a)



(b)

Fig. 3.4 Atomic Force Micrograph (AFM) of the Developed Spots in the Resist. (a) with 0.13 mJ/cm² dose and Section analysis of one spot along the cut line indicated FWHM = 92 nm, DOF = 36 nm. (b) with 0.17 mJ/cm² dose and Section analysis of one spot along the cut line showed FWHM = 119 nm, DOF = 56 nm.

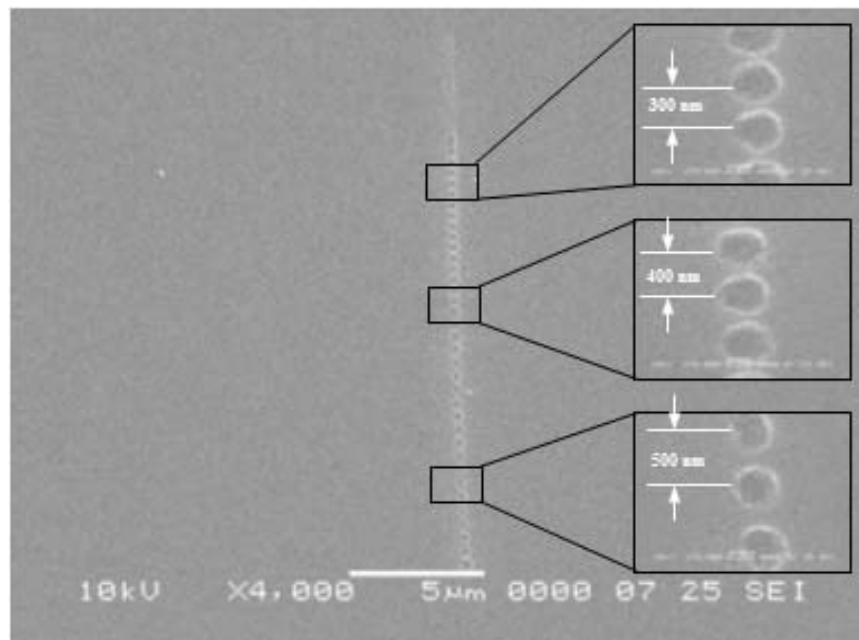


Fig. 3.5 SEM of the Developed Spots Whose Periods are 300 nm, 400 nm, and 500 nm. Dose for spots are all in same as 0.25 mJ/cm².

To confirm the existence and effect of the surface plasmon verified numerically in the simulation section, we prepared a simple optical antenna which is composed of a ring ($r = 2 \mu\text{m}$, $a = 150 \text{ nm}$) and a center hole ($r = 75 \text{ nm}$) in a 100-nm thick Ti thin film on a fused silica substrate as pictured in Fig. 3.6. Then, a set-up for contact lithography was prepared. Fig. 3.7 shows the contact printing using the simple optical antenna; a 405 nm UV laser illuminates a S1805 spin-coated (200 nm thick) Si sample for 90 s which is over exposed condition. Since this set-up only provides a fully contact mode, a big cover glass and proof mass weighted as 200g pressed the simple optical antenna firmly Fig. 3.7. And the 405nm UV laser was illuminated for 90 s which is an over exposure condition on the back side of the simple optical antenna. The light interaction emanating from the simple optical antenna was recorded in the S1805 g-line resist layer.

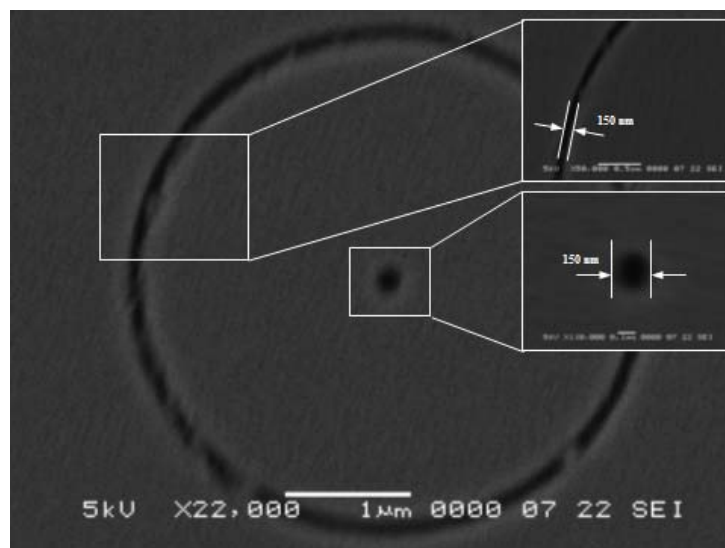


Fig. 3.6 SEM of the Simple Optical Antenna. Composed of a ring ($r = 2 \mu\text{m}$, $a = 150 \text{ nm}$) and a center hole ($r = 75 \text{ nm}$) in a 100 nm thick Ti thin film on a fused silica substrate.

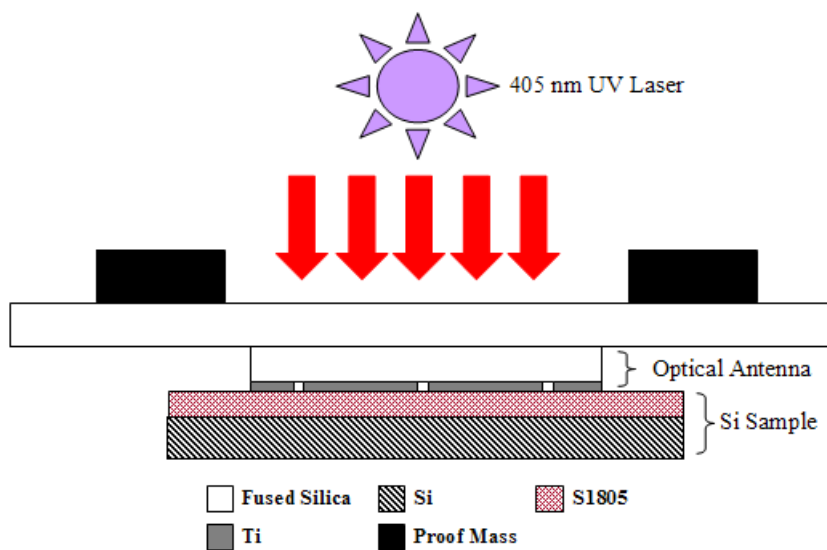


Fig. 3.7 A Set-Up for the Contact Printing Experiment Using a Simple Optical Antenna. Confirming the existence and effect of the surface plasmon.

Because the exposure was conducted with a firm contact condition, developed image of S1805 should show a replication of the simple optical antenna only if considering a conventional diffraction theory. However, the developed Si sample indicated that a number of ring patterns adjacent to the position of the mask contact were recorded and this would be regarded as standing waves of the surface plasmon. Fig. 3.8 describes an AFM image of the developed Si sample after over exposure with a simple optical antenna and actual mask size in amplitude of AFM is compared with recorded standing waves of surface plasmon.

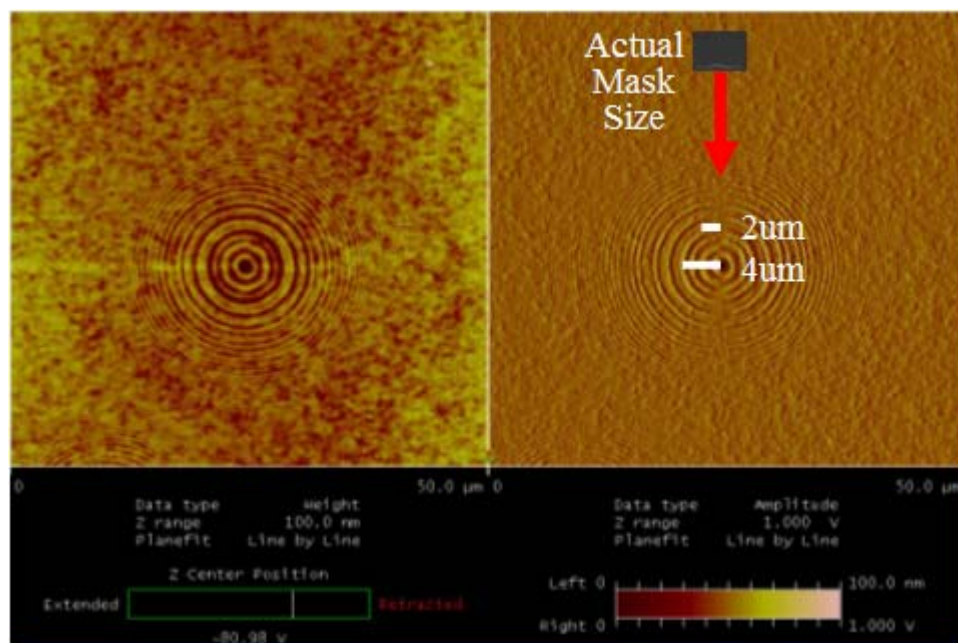


Fig. 3.8 AFM Image of the Over Exposed Si Sample with a Simple Optical Antenna. A weight (left) and amplitude (right) mode analysis – The actual mask is also plotted to compare with standing waves of surface plasmon.

3.3 Summary

Here, we demonstrated that an optical antenna that can focus a sub-wavelength spot with a working distance (also the focal length) of several μm theoretically and experimentally. Several OAs were fabricated by electron-beam lithography followed by reactive-ion etching. The OA was used to focus a collimated 405-nm laser to directly write an array of spots. The developed spot sizes ranged from 90 to 250 nm when the dose varied from 0.13 to 0.25 mJ/cm^2 . The pitches of the spots ranged from 400 to 500 nm. The highest imaging resolution (90-nm spots) is more than a 100% improvement of the diffraction limit ($\text{FWHM} = 210 \text{ nm}$). A model and 3D electromagnetic simulation results were also discussed. The PSF is attributed to the cylindrical SP wave excited at the Ti / air interface that is scattered by the apertures and becomes a propagating wave converging in the mid-field. The simulation predicts a FWHM of 210 nm. So, the 90-nm spots observed experimentally could be the result of underexposure. Nevertheless, the demonstrated 400nm pitch with good imaging quality indicates that the simulated FWHM, which is equivalent to a perfect lens with $\text{NA}=1$, is reasonable.

CHAPTER IV

PLASMONIC NANOLITHOGRAPHY – CONCLUSION

4.1 Conclusion

We proposed a novel photonic device - Optical Antenna - that acts as a nano scale object lens. It consists of a number of sub-wavelength features in a metal film coated on a quartz substrate. The device collimated incident light to form a narrow beam in the near field and even far field region. The narrow beam lasts for up to several wavelengths before it diverges.

We demonstrated that an optical antenna that can focus a sub-wavelength spot with a working distance (also the focal length) of several μm theoretically and experimentally. A number of OAs were fabricated by electron-beam lithography followed by reactive-ion etching. The OA was used to focus a collimated 405-nm laser to directly write an array of spots. The developed spot sizes ranged from 90 to 250 nm when the dose varied from 0.13 to 0.25 mJ/cm^2 . The pitches of the spots ranged from 400 to 500 nm. The highest imaging resolution (90-nm spots) is more than a 100% improvement of the diffraction limit (FWHM = 210 nm). A model and 3D electromagnetic simulation results were also discussed. The PSF is attributed to the cylindrical SP wave excited at the Ti / air interface that is scattered by the apertures and becomes a propagating wave converging in the mid-field. The simulation predicts a FWHM of 210 nm. So, the 90-nm spots observed experimentally could be the result of underexposure. Nevertheless, the demonstrated 400nm pitch with good imaging quality indicates that the simulated FWHM, which is equivalent to a perfect lens with $\text{NA}=1$, is reasonable.^{47,51}

4.2 Future Application

The Optical Antenna (OA) would allow us for high speed scanning, large field-of-view and significantly improved image contrast and imaging details via given its sub-wavelength resolution and extended working distance (WD). The OA can be used as a NSOM tip for High-resolution Spectroscopy and Microscopy. As we demonstrated in this dissertation, it has a power to concentrate the light into a sub-wavelength spot. This showed a possibility to be used as a maskless nanolithography technique comparable to electron-beam lithography, but the OA lithography system doesn't require a expensive high-vacuum technology, EUV or DUV resist, and ultra-short wavelength. By focusing light on smaller spots, the OA can also expand integration density of an optical storage disk and be used as a device for light emitting. The most important contribution of subwavelength optics may be to build a bridge between the traditional scale of optics and the newer, smaller scale of nanotechnology.⁵²

CHAPTER V

RAPID SENSING OF BACTERIA – SEPTIC

5.1 SEPTIC (SEnsing of Phage-Triggered Ion Cascade)

Nanowell is a device which enables a rapid and specific detection of bacteria using nano scale probe to monitor the electric field fluctuations caused by ion leakage from the bacteria. When a bacteriophage infects a bacterium and injects its DNA into the host cell, a massive, transitory ion efflux from the host cell occurs. SEPTIC (SEnsing of Phage-Triggered Ion Cascade) technology developed by our research group uses a nanowell device to detect the nano-scale electric field fluctuations caused by this ion efflux.⁵³ Since one bacteriophage only infects one specific strand of bacteria and the ion efflux occurs within minutes after the infection, SEPTIC can identify different bacteria with trace quantities in several minutes (alternative methods need well-equipped laboratory circumstances, expensive instrumentation, hours to days of pre-process), with no false alarm or missed detection.

5.1.1 Phage Specific Reaction

A bacteriophage, meant by ‘bacteria’ and Greek ‘phagein (to eat)’, is a virus commonly abbreviated as ‘phage’ that infects bacteria. Typically, phage consists of a protein that has 5000~500,000 base pair long dsDNA, ssDNA, or dsRNA which is in the form of either circular or linear arrangement. Phage is much smaller than the bacteria – usually between 20 and 200nm in size. Phages are ubiquitous and can be found in all reservoirs populated by bacterial hosts, such as soil or the intestine of animals. One of the densest natural sources for phages and other viruses is sea water, where up to 10⁹ virions per millimeter have been found and up to 70% of marine bacteria may be infected by phages.⁵⁴ The dsDNA tailed phages, or *Caudovirales*, take almost 95% of all phages reported in literatures.⁵⁵ Phages are classified by the International

Committee on Taxonomy of Viruses (ICTV) based on morphology and nucleic acid as the following Table 5.1 Phages can have a lytic cycle or a lysogenic, but some species may have both. Lytic phages like T4 lyse (broken open) and destroy the host cell immediately after their penetration and infection. As the cell destroyed, the new phages move to other cells and this continuous game chasing could be used a sort of phage therapy. On the contrary to the lytic cycle, the lysogenic cycle does not result in immediate lysing of the cell, so they are called as temperate phages. Their genome resides with host DNA and participates in the replication process, and they are dormant until host conditions deteriorate, perhaps due to depletion of nutrients, then the endogenous phages (or prophages) become active.

Table 5.1 ICTV Classification of Phages.⁵⁵

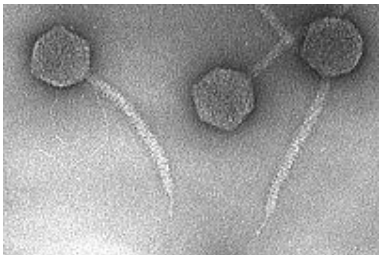
Order	Family	Morphology	Nucleic Acid
<i>Caudovirales</i>	<i>Myoviridae</i>	Non-enveloped, contractile tail	Linear dsDNA
	<i>Siphoviridae</i>	Non-enveloped, long non-contractile tail	Linear dsDNA
	<i>Podoviridae</i>	Non-enveloped, short noncontractile tail	Linear dsDNA
	<i>Tectiviridae</i>	Non-enveloped, isometric	Linear dsDNA
	<i>Corticoviridae</i>	Non-enveloped, isometric	Circular dsDNA
	<i>Lipothrixviridae</i>	Enveloped, rod-shaped	Linear dsDNA
	<i>Plasmaviridae</i>	Enveloped, pleomorphic	Circular dsDNA
	<i>Rudiviridae</i>	Non-enveloped, rod-shaped	Linear dsDNA
	<i>Fuselloviridae</i>	Non-enveloped, lemon-shaped	Circular dsDNA
	<i>Inoviridae</i>	Non-enveloped, filamentous	Circular dsDNA
	<i>Microviridae</i>	Non-enveloped, isometric	Circular dsDNA
	<i>Leviviridae</i>	Non-enveloped, isometric	Linear dsDNA
	<i>Cystoviridae</i>	Enveloped, spherical	Segment dsRNA

To penetrate into host cells, phages attach to specific receptors such as proteins, teichoic acids, lipopolysaccharides or even flagella. This specificity means that each phage can have its own host range which shows the phage specific reaction.

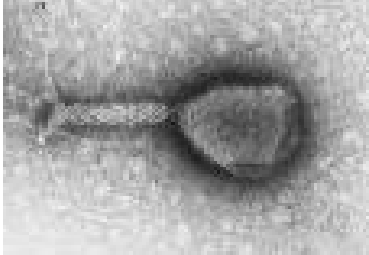
There are tens of extensively studied phages such as Lambda phage, T2 phage, T4 phage, T7 phage, T12 phage, R17 phage, M13 phage, MS2 phage, G4 phage, P1 phage, P2 phage, Phi-X174 phage, N4 phage, Phi-6 phage, and Phi-29 phage, but the most classic coliphages Lambda, T4, and T7 are investigated to study phage specific reaction with *Escherichia coli* (E-coli) bacteria in this dissertation. Table 5.2 compares those three most popular phages and their characteristics.

Table 5.2 Three Classic Coliphages.


Lambda	T4	T7
Group : dsDNA	Group : dsDNA	Group : dsDNA
Order : <i>Caudovirales</i>	Order : <i>Caudovirales</i>	Order : <i>Caudovirales</i>
Family : <i>Siphoviridae</i>	Family : <i>Myoviridae</i>	Family : <i>Myoviridae</i>
DNA : 48.5 kbp	DNA : 170 kbp	DNA : 40 kbp
Head : 50 nm	Head : 60 nm	Head : 80*110 nm
Tail : 150 nm flexible	Tail : 20 nm stubby	Tail : 115 nm contractile
* 4 tail fibers	* 6 tail fibers	* 6 tail fibers
** Lysogenic – temperate	** Lytic – virulent	** Lytic – virulent



56



57



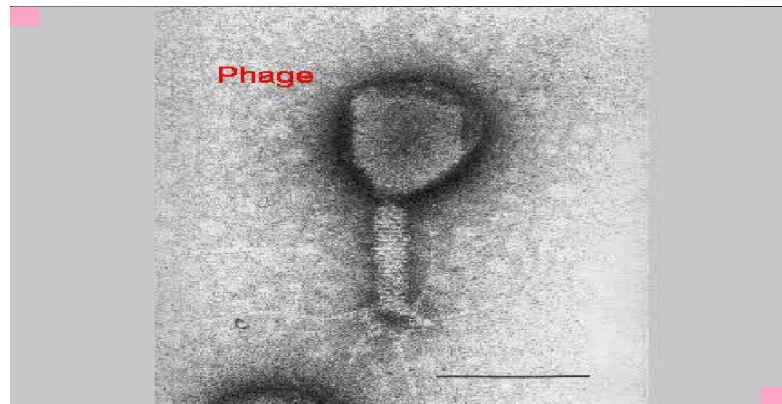
58

5.1.2 Detection Principle of the SEPTIC

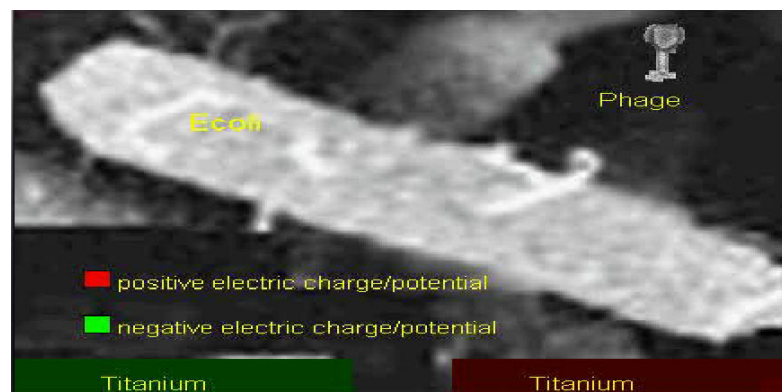
As we discussed in section 5.1.1, phages have become a focus of interest for diagnosis and therapy of bacterial disease in humans, animals and plants.⁵⁹⁻⁶¹ When a phage infects a

bacterium, the phage injects its DNA into the host cell, accompanying an efflux of ions from the host. These ions cause microscopic electric field disturbance that can be picked up a nearby nano/micro device and recognized via electric noise analysis. Since the infection of bacteria by phage is specific and usually occurs within several minutes, detecting the electrical noise based on phage-bacteria reaction provides a highly specific and identification of living bacteria, without the need of growing bacteria or complicated manipulations of nucleic acids. In order to observe this electrical noise due to the ion leakage, we have constructed nanowell devices which are composed of two electrodes with a nano or micro scale gap between them. The nanowell devices were fabricated by a hybrid of electron beam lithography (EBL), contact photolithography and reactive ion etching (RIE).

Fig. 5.1 shows sensing mechanism of the SEPTIC technology. T4 Phage (a) approaches to the bacterium (b) at which two metal electrodes receive the noise signal between bacterium and phage after infection. Phage attaches to the surface membrane of the bacterium and drill a hole to on it (c). Then it infects the host by injecting its DNA into the cell (d). Through the DNA infection process, over 100 million of ions leak from the host and this results in the electric field fluctuation which is detected by two electrodes in nanowell sensor.

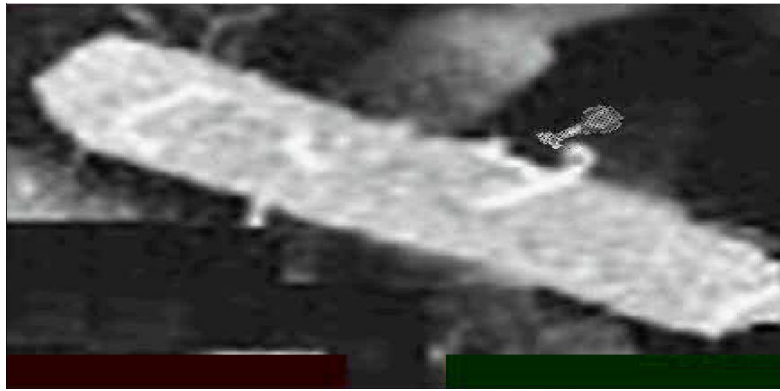


(a) T4 phage

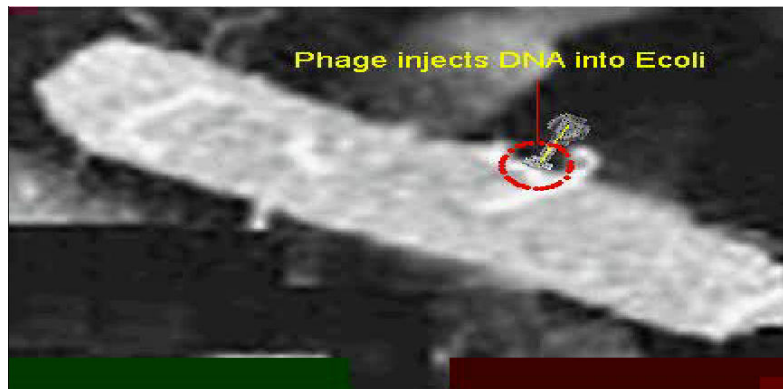


(b) Phage approaches to *E-coli*

Fig. 5.1 Illustration of the Detection Principles of the SEPTIC Technology.

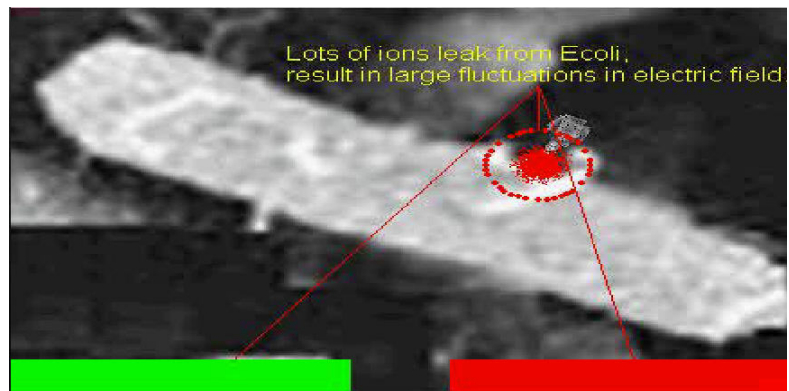


(c) Drill a hole on the membrane of the host



(d) Phage injects DNA into *E. coli*

Fig. 5.1 (continued).



- (e) Over 100 million of ions leak from the host result in electric field fluctuation which is detected by two electrodes in nanowell sensor.

Fig. 5.1 (continued).

CHAPTER VI

RAPID SENSING OF BACTERIA – EXPERIMENT

6.1 Device Fabrication

6.1.1 Nanowell and Microwell Sensor

The fabrication of the nanowell device includes two lithography processes: first, electron beam lithography (EBL) was used to write the nanowell ($150\text{ nm} \times 60\text{ }\mu\text{m}$); then conventional contact photolithography was used to pattern two large contact pads ($5\text{ mm} \times 5\text{ mm}$) and bridges ($100\text{ }\mu\text{m} \times 4\text{ }\mu\text{m}$) connected with the two pads. The pads were used for electrical connections with external circuitry and the bridges connect between the pads and the nanowell. The top-down view of the chip is illustrated in Fig. 6.1. The nanowell is actually a 150 nm wide gap in the middle of the bridges. Then the nanowell is 150 nm wide and $4\text{ }\mu\text{m}$ long, as indicated by Fig. 6.1.

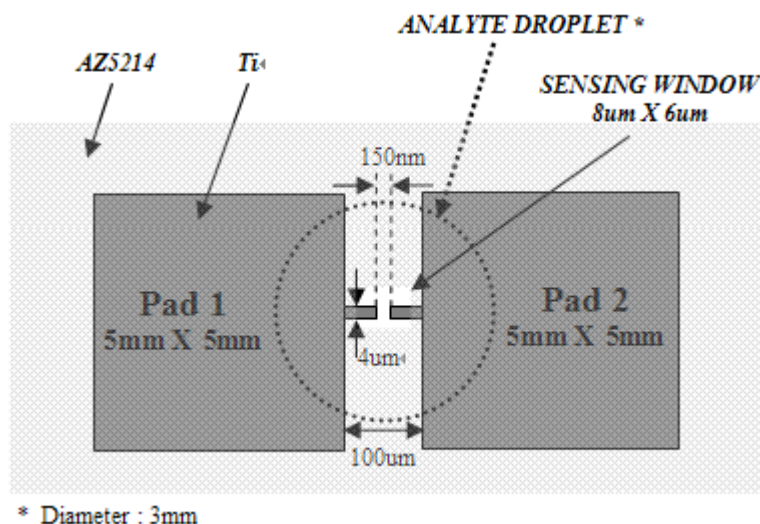


Fig. 6.1 Top-Down View of the Chip with Nanowell, Contact Pads and Bridges. Connecting between the pads and the nanowell

Fig. 6.2 shows the fabrication processes of the nanowell sensor. First, a 100-nm thick Ti layer was deposited on the surface of a lithium niobate (LiNbO_3) substrate by a DC sputtering system with 3200 V / 40 μA under the pressure of $2 * 10^{-6}$ torr. Then a 3% PMMA (950K Mono Chloro Benzene, Brewer Science Inc.) was spin coated on the Ti deposited layer. The spinning was 4000rpm for 60 s and followed by soft baking at 185°C for 90sec. The thickness of PMMA after soft bake was 200 nm. Then a 150 nm wide, 60 μm long trench is written on the PMMA film by electron beam lithography (EBL). The developer was a mixture of MIBK : IPA (1 : 3) and the development time was 1 min Fig. 6.2(a). Then the unprotected 150nm wide, 60 μm long Ti trench was etched anisotropically by reactive-ion etching (RIE) at the pressure of $2 * 10^{-5}$ torr with Ar (3 sccm) / CHF_3 (30 sccm) / He (7.5 sccm) gases. For efficient removal of Ti residue, a 10min sonication cleaning process was followed after every separated RIE process Fig. 6.2(b). Since the etching selectivity of PMMA to Ti in RIE process was almost 10 and 20nm PMMA was not enough for successful 100nm Ti etching mask, a 80% of original Ti layer was sacrificed during following subsequent RIE steps. The final thickness of the Ti layer was measured as 20 nm by a surface profilometer (Dektak 3). The whole chip was then cleaned by stripper AZ300T at 95°C for 15 min. Contact pads are then defined by conventional contact photolithography with positive resist AZ5214 using a mask aligner (MJB-3, Karl Suss). The power which was used to pattern contact pads was 11.0 mW/cm^2 for 5.8 s without filter Fig. 6.2(c). The resist processing parameters were: spinning 5000 rpm for 30 s, soft baking 99°C for 2 min on a hot plate. After developing AZ5214 resist, the Ti layer outside the contact pads was etched by RIE Fig. 6.2(d) and the resist layer was stripped by AZ300T stripper at 95°C for 15 min Fig. 6.2(e). Finally, the whole chip was spin coated with AZ5214 resist and patterned to make sensing window using mask aligner MJB-3 with the parameters of 5000 rpm – 30 s spinning, 99°C – 2 min soft baking on the hot plate, and 135°C – 12 min hard baking in a convection oven Fig. 6.2(f).

Fig. 6.3(a) shows an optical microscope image of the fabricated chip with one nanowell device, two contact pads and two connection bridges and (b) is a scanning electron microscopy (SEM) image of the fabricated nanowell.

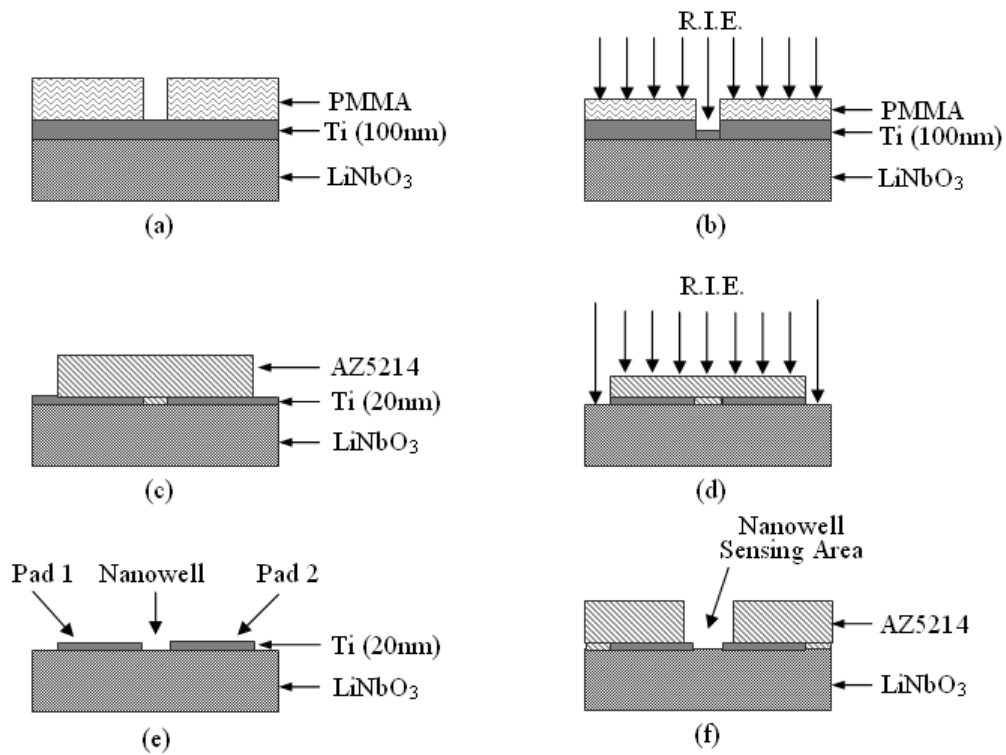


Fig. 6.2 Fabrication Processes of the Nanowell.

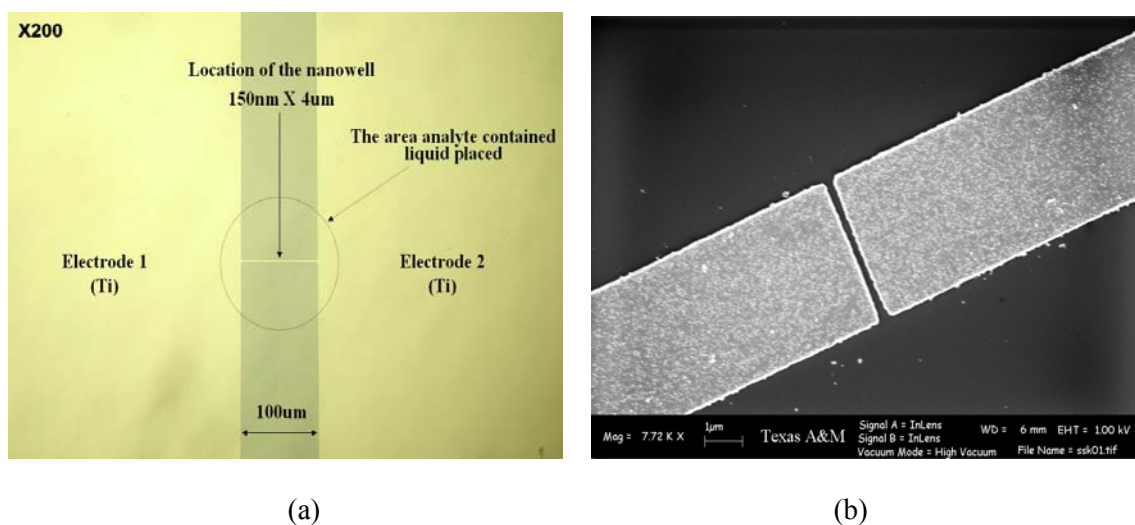


Fig. 6.3 Fabricated Nanowell. (a) 200X Optical microscope image of the fabricated nanowell device and contact pads. (b) SEM image of the nanowell.

To study the effects of the device compositions and structures, we fabricated a set of microwell array devices with different metals, different passivation layers, and different gaps on glass substrate. Two types of metal layers were patterned: 1) Ti, and 2) Au on top of Cr. And two types of passivation layers were used: 1) SiO₂ and 2) AZ 5214 resist. Each microwell connects to a pair of contact pads with 2 mm * 1 mm size. The electrodes in the microwell are 4 μm wide and 200 μm long. The gaps are 4, 10, 20 and 40 μm wide. The whole chip, except for big pads and sensing gap area, is passivated by a SiO₂ or AZ5214 resist layer. The sensing element, i.e. the gaps and the tips of the electrodes, are exposed to the analyte through a rectangular window. Fig. 6.4 shows a passivated microwell device.

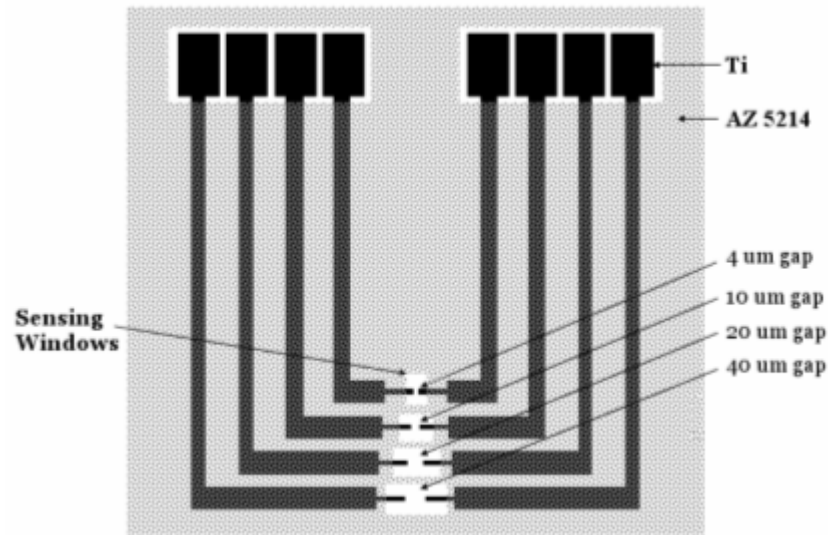


Fig. 6.4 Top-Down View of the Microwell Array with Different Gaps.

As illustrated in Fig. 6.5, the microwell devices were fabricated with similar processes of nanowell device except for electron beam lithography. First, a 150 Å thick Cr and a 450 Å Au layer were deposited on the surface of a glass substrate (2957F, VWR) through thermal evaporation in the pressure of $2 * 10^{-6}$ torr. In the case of fabricating Ti microwell arrays, a 600 Å Ti layer was sputtered with 3200 V / 40 μA DC bias under the pressure of $2 * 10^{-5}$ torr. The gas used in sputtering was 140 sccm Ar gas (Fig. 6.5(a)). Then AZ5214 resist was spin coated on the deposited Cr/Au or Ti layer, spinning speed 5000 rpm, spin time 40 s. The chips were then soft baked at 99°C for 2 min on a hot plate. The thickness of AZ5214 resist after soft baking was 1.2 μm. The microwell was patterned by contact lithography (MJB-3, Karl Suss), illuminating power 5.3 mW / cm², exposure time 10 sec without filter. After developing AZ5214 resist with a diluted MF312 (1 : 1.2 = D.I. : MF312), the Cr / Au or Ti layers were etched isotropically by Cr etchant (Type TFA, Transene Company), Au etchant (Type 1020, Transene Company) and

diluted 48% HF solution (1 : 30 = HF : D.I.) respectively (Fig. 6.5(b)). Then the resist layer was stripped by AZ300T stripper at 95°C for 15min.

To pattern the SiO₂ passivation layer, first a resist layer was spin-coated on the chip with the parameters mentioned above. Then the resist, except for the part covering the microwell gaps and the tips of the electrodes, was removed through contact lithography. Then a SiO₂ film was deposited on the chip by a RF sputtering system, the recipe was: $17.5 * 10^{-6}$ torr pressure, 400 W power and 30 sccm (Ar) / 2 sccm (O₂) gases. The remaining resist was then eliminated by lift-off process assisted with acetone sonication, so the microwell sensing elements were exposed to the ambient.

For the AZ5214 resist passivation layer, the sensing window was formed through image reversal. AZ5214 resist was applied on the chip, spin-coating 5000 rpm for 40 s, soft baking 115°C for 1 min. Then the whole resist, except for the part covering the sensing element, was pre-exposed for 2 s, illuminating power 5.3 mW/cm². Then the chip was processed with the following recipe: post-exposure bake 115°C for 3 min, then flood exposure 5.3 mW/cm² for 2 min, and developed in the diluted MF312 for image reversal (Fig. 6.5(c)). Fig. 6.6 shows the fabricated microwell array with Cr / Au electrodes and SiO₂ passivation layer on the surface of the glass wafer.

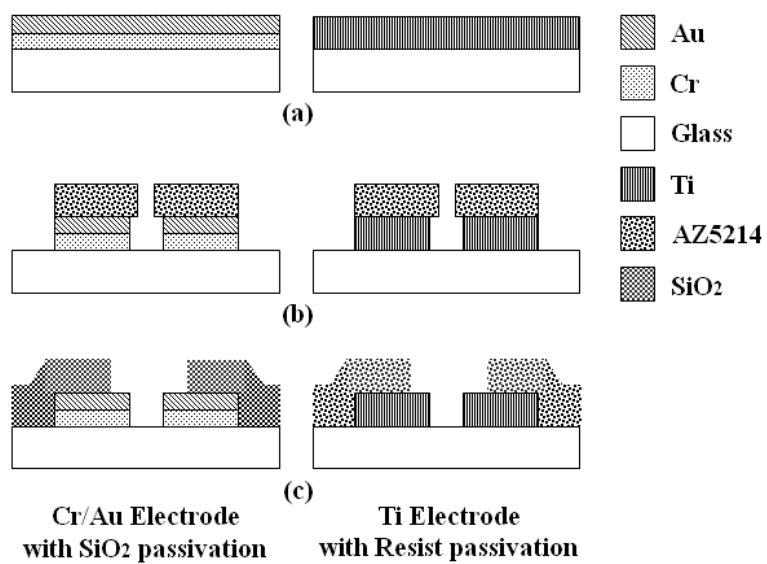


Fig. 6.5 Fabrication Processes of the Microwell Array.

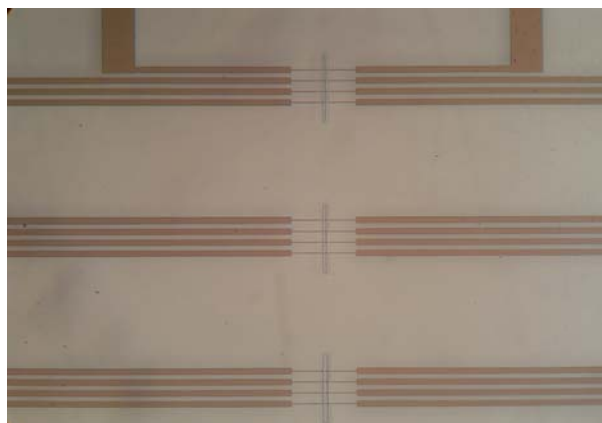


Fig. 6.6 Fabricated Microwell Array.

6.1.2 Ion Selective Field Effect Transistor (ISFET) Sensor

An Ion Selective Field Effect Transistor (ISFET) Sensor²³ was proposed to detect ion leakage between bacteria and phage. Comparing with usual Metal Oxide Semiconductor Field Effect Transistor (MOSFET), ISFET uses an electric field fluctuation of phage infection around the gate area without using a physical gate. The idea is that when the bacterium ejects their ions which were resulted by DNA injection of a phage, changed electric field around the gate can affect on the IV (Current-Voltage) characteristics as well as the threshold voltage of the ISFET. Since solid state sensor can magnify an input signal by itself, this type of device can provide much higher sensitivity and integration possibility. To fabricate this ISFET sensor, we have conducted the whole processes that MOSFET requires except for fabricating suspended and apart from electron channel design gate.

Firstly, a n-type phosphorous doped (10^{15} cm^{-3}) Si wafer was cleaned initially recipes with 10 min soap rinsing, 10 min acetone dipping and sonication, 10 min methanol dipping and sonication, 1 min diluted HF solution (1 : 10 = HF : D.I.), and 10 min more acetone and methanol. Then, a 7000 Å thick oxide layer was grown by furnace with gases of N_2 and O_2 . Furnace temperature was set as 1100 °C with gas sequence of 5 min (O_2) – 60 min (steam) – 5 min (N_2) – 25 min (O_2). Next, source and drain were defined as shown in Fig. 6.7(a). An adhesion promoter (HMDS) and an AZ5124 i-line resist were spun on SiO_2 layer with parameters of 5000 rpm for 30 s. After 2 min soft baking on a 91°C hot plate, source and drain were defined by MJB-3 mask aligner with 40 s development in diluted MF312 (MF312 : D.I. = 1 : 1.2) solution. Then, the SiO_2 of source, drain, and electron channel was etched by BOE (7 : 1 diluted with water) solution. And the suspended gate was defined by electron beam (e-beam) evaporation and lithography processes (b). After stripping the resist in a piranha solution (H_2SO_4 : H_2O_2 = 50 : 1) at 120°C for 5 min, a 300 Å thick silicon dioxide was evaporated by e-

beam evaporator and patterned as a key shape gate above the channels. Then the chip was hard baked in a 135°C convection oven for 5 min followed by BOE (7 : 1 diluted) wet etching. Another hard baking was done before the ion-implantation process. Boron (B11) implantation forming p⁺ region was done as an out sourcing process (Core System, California) with appropriate dose ($1.5 * 10^{15} \text{ cm}^{-2}$), energy (50 keV), and injection angle (7°) as described in (c). Then, the whole chip was cleaned in piranha solution to clean off particles and hard mask resist. Drive-in and annealing processes were performed in an 1100°C furnace with gas sequence of 5 min (air) – 35 min (N₂) (d). For the metallization, Au deposition (3000 Å) was conducted by a thermal evaporator and patterned to define metal contact. After hard baking in the 135°C convection oven for 5 min, Au layer was etched in a diluted aqua regia (HCl : HNO₃ : H₂O = 3 : 1 : 4) solution (e). Finally, to passivate the whole chip except metal contacts and gate region opening, another key shape gate patterning was done over SiO₂ key pattern. Then, SiO₂ layer of 5000 Å was deposited for passivation and the key shape resist (AZ 5214, 1.2 μm thickness) was lifted off in the AZ300T stripper of 95 °C for 15 min (f).

Fabricated ISFET sensor is shown in Fig. 6.8(a) X200 optical microscope image and (b) X1000 magnification.

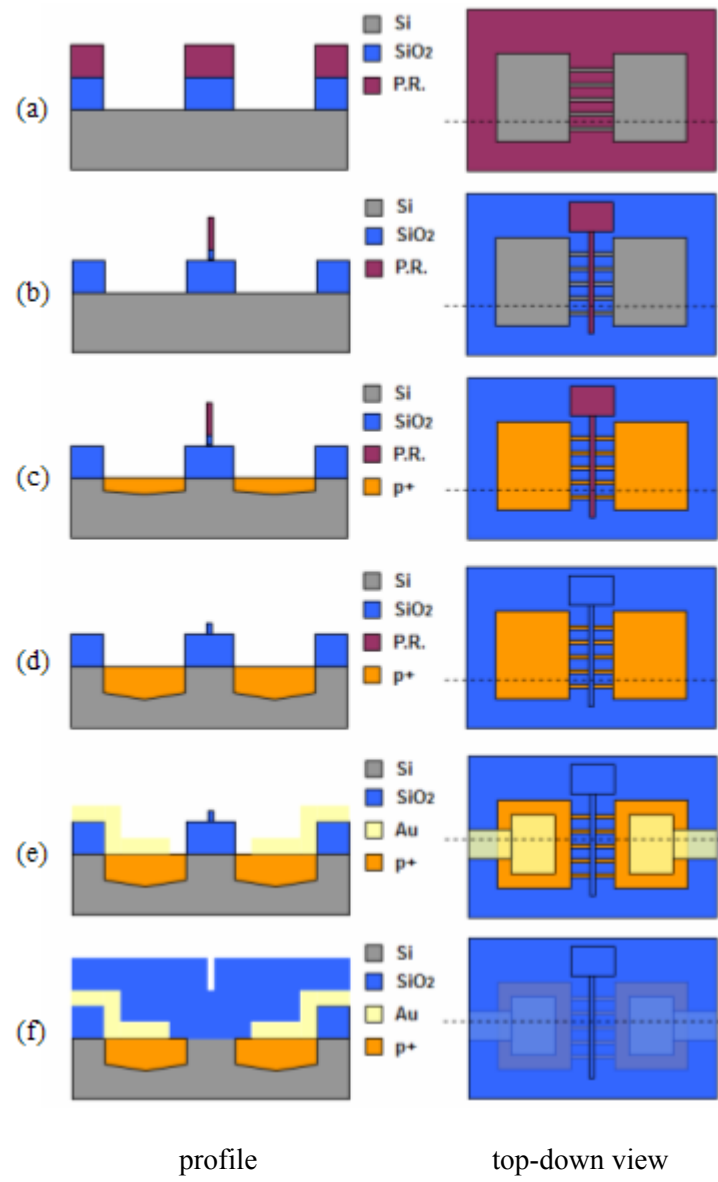
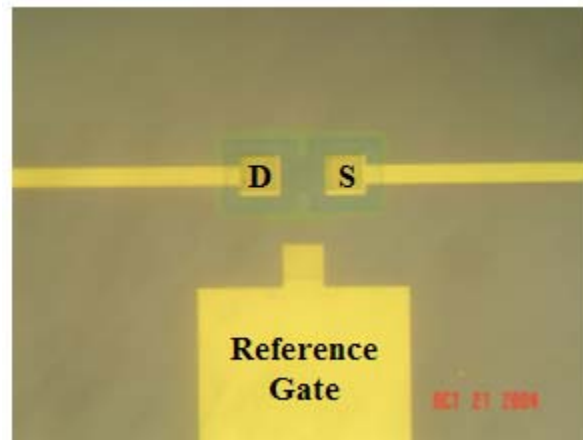
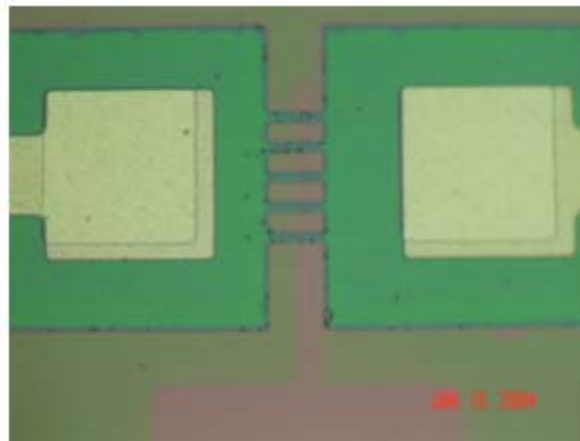


Fig. 6.7 Fabrication Processes of the ISFET.



(a)



(b)

Fig. 6.8 Fabricated ISFET Sensor. (a) X200 Optical Microscope Image (b) X1000 Magnification

6.2 Experiment Apparatus

During this experiment, the solution containing bacteria and phage was dropped in and around the nanowell, as indicated by the dotted circle in Fig. 6.1. Two probes, which provide input to an external voltage amplifier, were firmly pressed on the contact pads. In order to prevent short circuit between the two pads and reduce unwanted noise caused by ions in the

solution, the surface of the chip, except for the nanowell sensing area, was covered with hard baked resist AZ5214. A 6 μm * 8 μm rectangular window was then opened by photolithography, i.e., only the opened sensing window indicated in Fig. 6.1 was exposed to liquid during experiment. Fig. 6.9 shows the schematic representation of the experimental apparatus. The voltage fluctuations induced on the nanowell device by the electrical field was amplified by a low-noise preamplifier SR560 with high input impedance (100 M Ω) and fed into signal acquisition unit ML750 PowerLab/4SP as illustrated in Fig. 6.9. The power density spectrum of the fluctuations in frequency and time domain was determined by a Dynamic Signal Analyzer SR785 or a personal computer. The nanowell was placed in a double screening box (Amuneal Manufacturing Corp.) to shield the electromagnetic noise of outside of the box. The double screening box and the preamplifier were placed on an anti-vibration platform 100BM-2 (Nano-K) to avoid potential artifacts caused by vibrations. The time window of the determination of the power density spectrum $S_u(f)$ was 2 min.

For the microwell experiment, a drop of solution containing bacteria and phages was dropped onto the sensing window as done for the nanowell. The voltage noise in the microwell is fed to the external voltage preamplifier. The microwell was zero-biased. The voltage preamplifier was made with an instrumentation amplifier, model AMP02E from Analog Device Inc. The amplified signal was acquired by a USB DAQ card and then sent to a PC for analysis. The microwell chip and preamplifier were placed in a stainless steel shielding box to prevent electromagnetic interferences. The system diagram shown in Fig. 6.9 was repeated in the microwell experiments.

We tested the bacteria sensor systems with *E. coli* bacteria named 17181, phage T7 & lambda (λ) UR which are reactive to *E. coli*, and control bacteria coded B & 17202 insensitive to phage T7 & λ UR respectively. The bacteria and phage concentrations were all 10^9 c.f.u./ml.

Positive tests refer to the analyte containing *E. coli* (17181) and λ -UR or *E. coli* (17181) and T7, in which phage infection occurred. Negative tests refer to the analytes containing: 1) T7 only, 2) 17202 plus λ UR, and 3) B plus T7. In these analytes no infection can occur. During tests, the bacteria and phage were mixed (if necessary) at the temperature 37°C, and then dropped onto the nanowell or microwell without incubation.

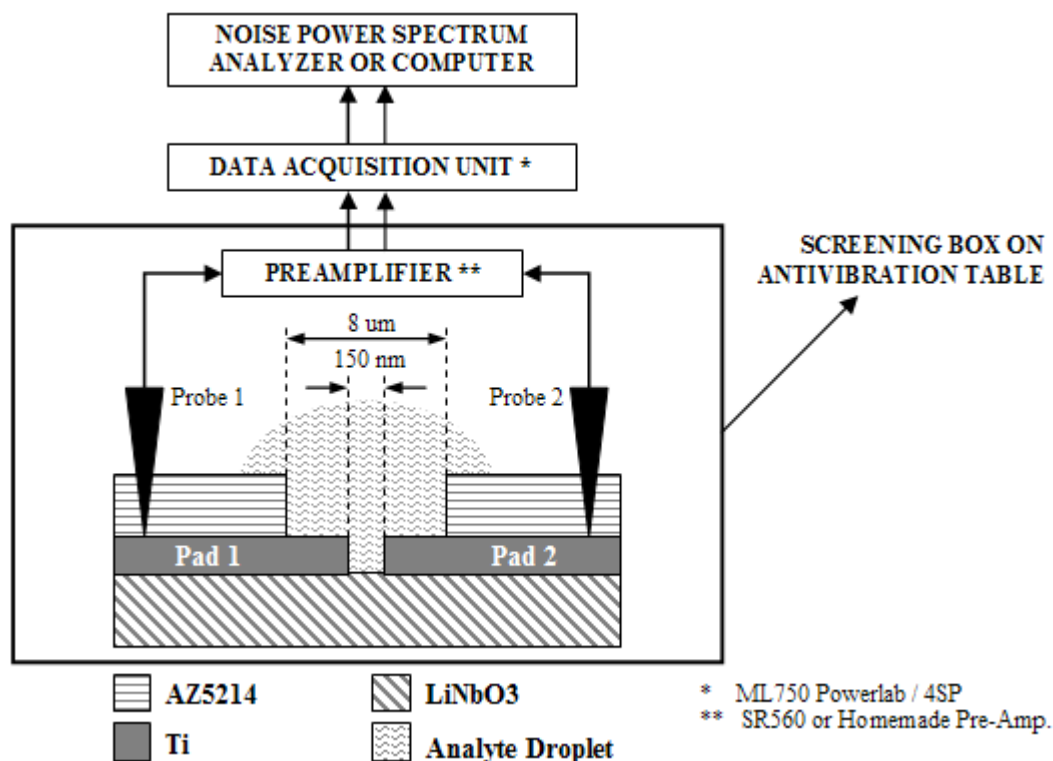


Fig. 6.9 Experiment Apparatus for the Nanowell / Microwell Sensor.

6.3 Experiment Results

6.3.1 Nanowell / Microwell Sensor

The fabricated nanowell device which had 150nm gap was used to measure the electrical field fluctuations in a fluid containing various strains of phage-infected *E. coli* bacteria.

In the presence of non-adsorbing phages and bacteria such as 17202 bacteria plus UR phage, the electrical field fluctuations were small, displaying power density spectra of approximately $1/f$ shape (see Fig. 6.10). After the phage invasion, we experienced large and slow stochastic waves with various time and amplitude scales.⁵³ These fluctuations had power spectra of approximately $1/f^2$ shape in the frequency range of 1 - 10 Hz. Experiments with 17181 bacteria and UR phage resulted in high electric fluctuations between 1min and 5min pre-incubation times, indicating a fast adsorption process of phages into bacteria, for only a limited time period.

To understand the spatial nature of the fluctuations, a device which has 100um gap was also tested. In this case, the spectra of all positive and negative cases were identical, see Fig. 6.11. This result indicates that the fluctuations have random sign space and time. As they average out in large detectors, the nanowell or smaller gap detector systems are required to observe them.

For microwell, our experiments showed no difference between microwell devices with different metals or different passivation layers. Thus in this section, we only discuss the data obtained through a SiO_2 passivated Au/Cr microwell. To investigate optimized gap size, we tested the gaps of 4, 10, 20 and 40 μm under the size of 100 μm – the big gap showing no differences between positive and negative tests.

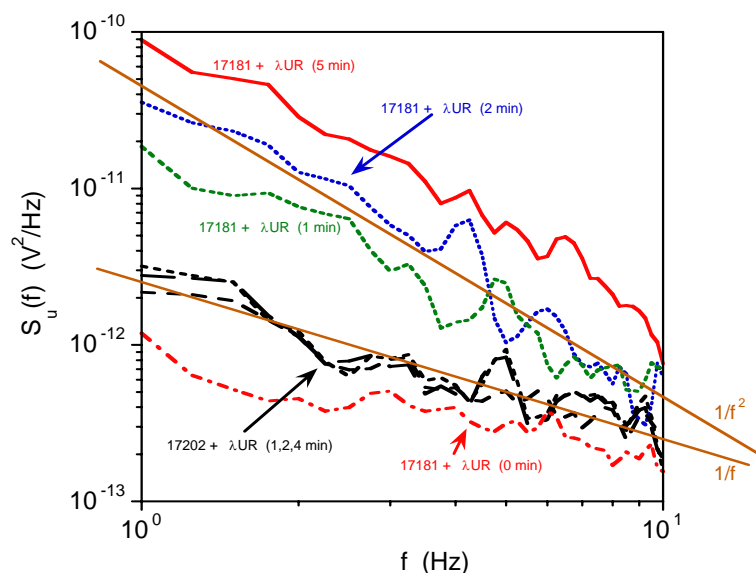


Fig. 6.10 Response with Lamda-UR Phages with Different Host Bacteria. Incubation times were 5 minutes. In the case of negative response (with host #17202), the spectrum of voltage fluctuations in the nanowell roughly follows $1/f$ shape. In the case of positive response (with host #17181), the fluctuations are enhanced resulting in a steeper spectrum with a $1/f^2$ like shape.

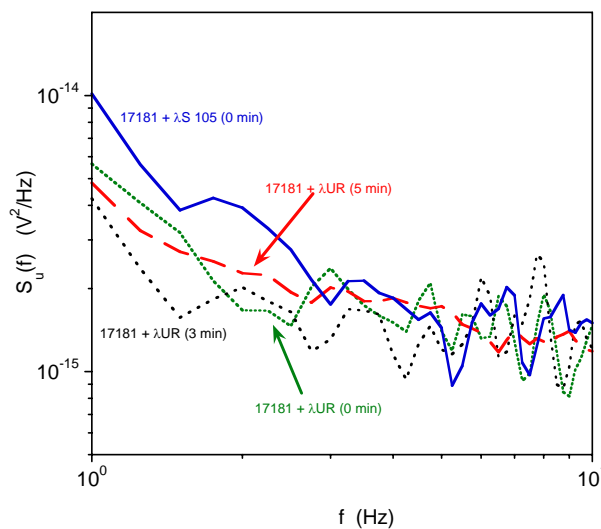


Fig. 6.11 The Spectrum Measured in the 100 μ m Gap Device. Did not show any observable dependence on phage infection. This fact indicates that the electrical field fluctuations and the ionic charge density fluctuations are random in space and time, averaging out with the larger detector.

In previous experiments, only frequency analysis of the measured data was employed.⁵³ Now we show that time analysis can also identify the positives and negatives.⁶² Fig. 6.12 and Fig. 6.13 shows two time series of the measured voltage in a positive and a negative test. In the negative test, the analyte only contained T7. Denote the measured voltage series as V_n , $n = 0, 1, 2, \dots, N$. Denote as the mean square of the series:

$$\sigma^2 = \frac{1}{N} \sum_{n=0}^N V_n^2 \quad (2.14)$$

If $V_n, n = i, i+1, \dots, i+l$, satisfy the condition

$$V_n > 4\sigma, n = i, i+1, \dots, i+l \text{ or } V_n < -4\sigma, n = i, i+1, \dots, i+l \quad (2.15)$$

Then this segment of V_n is called an abnormal pulse, because it is much beyond the noise level. In Fig. 6.12, such an abnormal pulse appeared. It lasted for about 0.15 sec, which agrees with the typical ion leakage time of 0.1~0.3 s when an *E. coli* bacterium is infected by a phage. So this pulse indicates a phage infection event.

Abnormal pulses may appear in negative tests as well, as shown in Fig. 6.13. This abnormal pulse, however, lasted much shorter than 0.1 s. Thus it could not be caused by phage infection. Instead, it might be due to mechanical vibration, unshielded electric disturbance, etc.

In every positive test, we observed one or several abnormal pulses that lasted 0.1 ~ 0.3 s. While in all the negative tests, all the abnormal pulses we observed were less than 0.1 s. Thus negatives and positives can be identified via this criterion.

Of course, negatives and positives can also be identified through frequency analysis. The PSD of the voltage noise in the microwell, denoted by $S(f)$, is calculated. Then the PSD in the 1-10 Hz range is interpolated by a function $1/f^\beta$, where β is a characteristic of a noise.

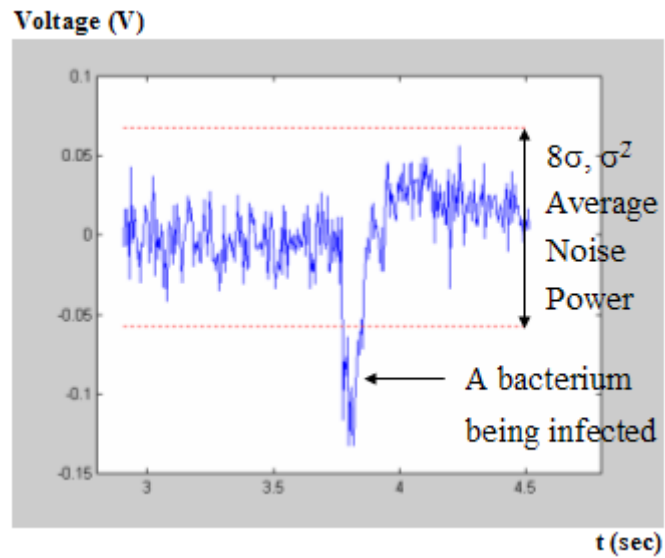


Fig. 6.12 Time Series of the Measured Voltage in Positive Test (*E-coli* plus T7 phage).

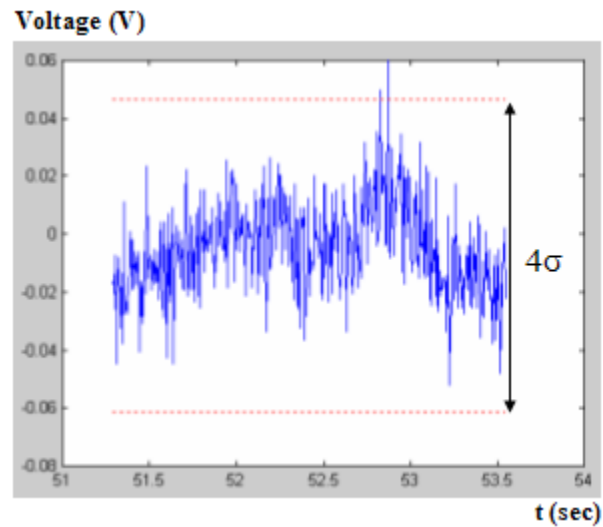


Fig. 6.13 Time Series of the Measured Voltage in Negative Test (T7 phage only).

The power spectra of a negative (B + T7) and a positive are compared in Fig. 6.14. They differ in the range of 1-10 Hz, but are indifferent at higher frequencies. In 1-10 Hz, the negative noise is a white noise ($\beta \sim 0$), whereas the positive noise is a $1/f$ noise ($\beta \sim 1$). Note that this differs

from the previous results in Fig. 6.10, which reports that negative noise is $1/f$ while positive is $1/f^2$. We believe this difference comes from the preamplifiers. Fig. 6.10 employed a commercial preamplifier with some filter configurations, SR560 from Stanford Research Systems Inc., while we used a simple home-made preamplifier.

Table 6.1 summarizes the average β of the positive and negative noises. Obviously the positive noise (*E. coli* + T7) is close to $1/f$ noise while the negatives are close to white noise.

Table 6.1 The Average β of the Positive and Negative Noises.

Analyte	T7	B + T7	<i>E. coli</i> + T7
Average β	0.18	0.12	0.92

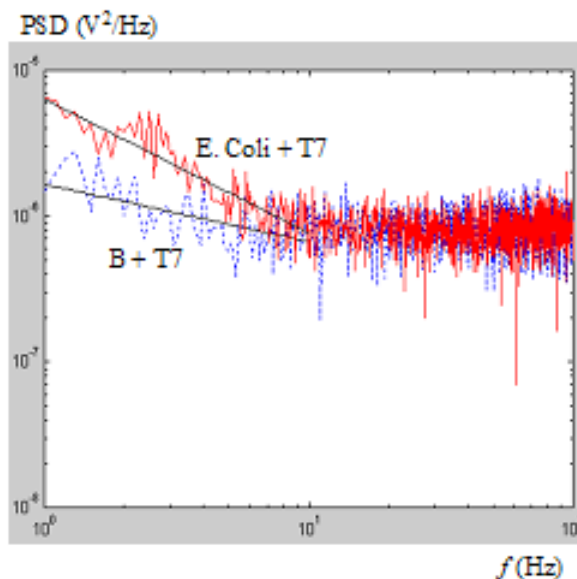
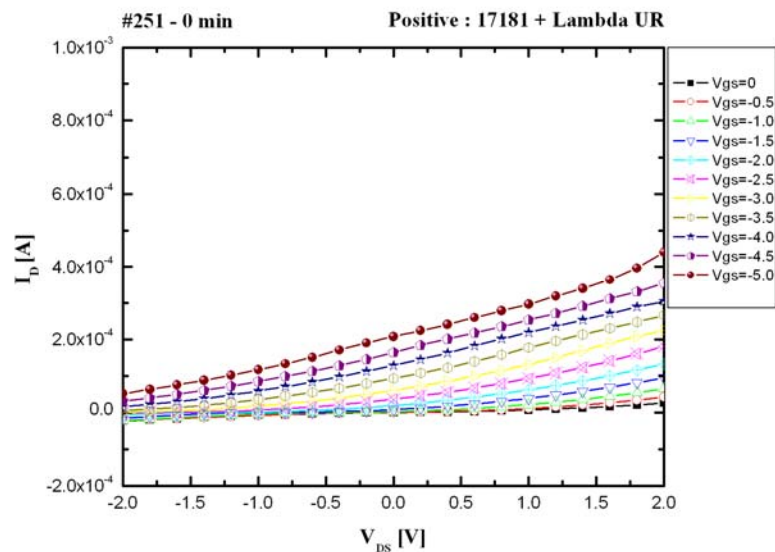


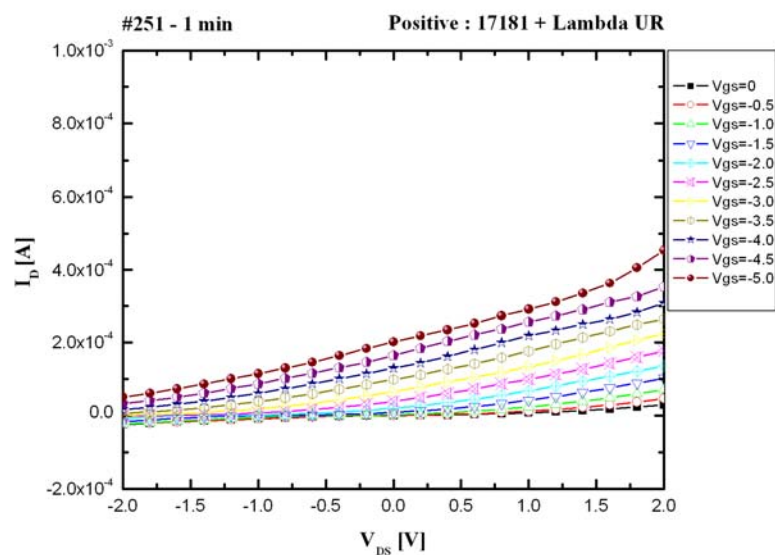
Fig. 6.14 The PSD of a Positive Noise (*E-coli* plus T7 Phage, the Solid Red Curve) and a Negative Noise (T7 Phage only, the Dotted Blue Curve). These PSD are interpolated by $1/f^\beta$, the black straight lines in the plot.

6.3.2 ISFET Sensor

To investigate ISFET sensor's sensing ability, we tested the positive reaction analyte mixture of *E-coli* (coded 17181) and UR phage which showed strong positive signal in frequency domain measurement. Since this ISFET is basically a p-type field effect transistor, a gate voltage (V_G) between 0 ~ -5 [V] with 0.5 [V] step was applied to the suspended gate of the ISFET. And the -2 ~ 2 [V] drain-source voltage (V_{DS}) of a 200 mV step was swept by a semiconductor parameter analyzer (HP 5220). The ISFET was shielded and connected to a probe station between ISFET and HP5220. Since each sweep takes almost 40 s to process the data, we extracted current-voltage (IV) characteristics once every minute as Fig. 6.15. (a) shows IV characteristics of ISFET when the analyte droplet was applied. The drain-source current I_D was measured as $4.4 * 10^{-4}$ [A] at the $V_{GS} = -5.0$ [V] and $V_{DS} = 2.0$ [V]. At the same V_{GS} and V_{DS} , the I_D was fluctuated as the time goes on. $I_{D,0\ min} = 4.4 * 10^{-4}$ decreased to $I_{D,3\ min} = 2.7 * 10^{-4}$, $I_{D,5\ min} = 2.7 * 10^{-4}$, and $I_{D,7\ min} = 2.9 * 10^{-4}$ as shown in (c), (d), and (e). Relatively high drain current was only measured at the initial stages such as (a) and (b), this implies that the phage infection to the host occurred and was measured within the first 1 minute after analyte mixture dropped. Another noticeable thing is that the sudden jump in I_{DS} at 7 min (f) was observed at the $V_{GS} = -5.0$ [V] and $V_{DS} = 0$ [V]. This result could be understood as the 0.1~0.3 abnormal pulse from positive reaction. However, ISFET has not been fabricated by normal field effect transistor processes, it showed a non-saturated IV-curve which should be a basic characteristics of field effect transistor.

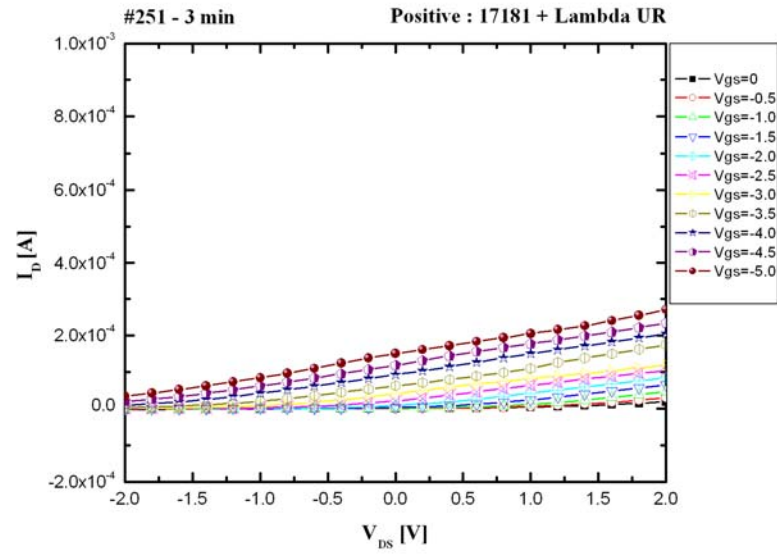


(a)

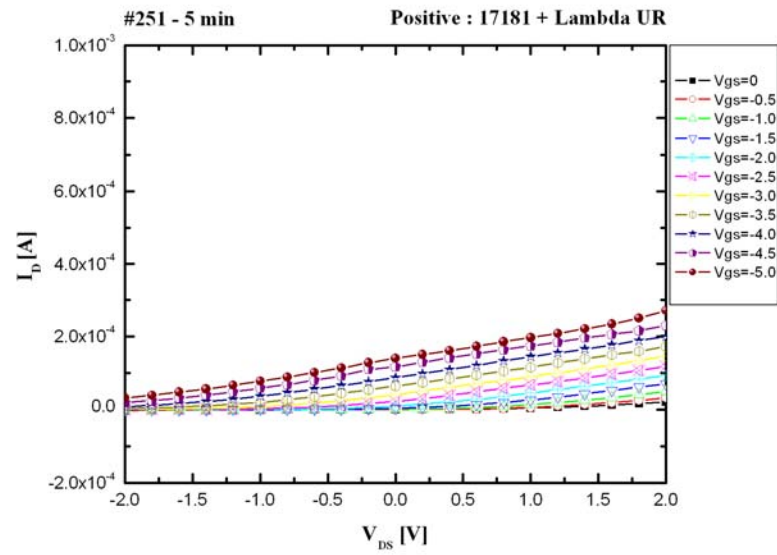


(b)

Fig. 6.15 ISFET IV-Characteristics with E-coli (coded 17181) Bacteria and Lambda-UR Phages. (a) 0 min (b) 1 min (c) 3 min (d) 5 min (e) 7 min after the analyte mixture dropped.

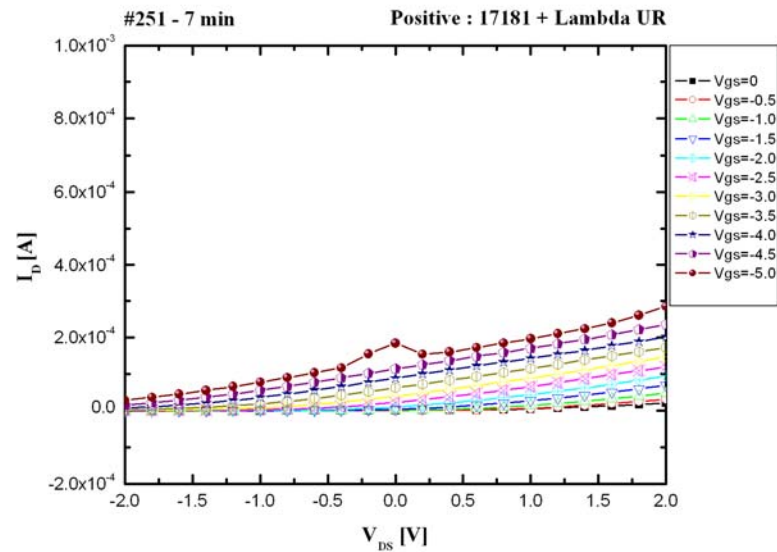


(c)



(d)

Fig. 6.15 (continued).



(e)

Fig. 6.15 (continued).

6.4 Summary

A novel bacteria detection and identification method SEPTIC (Sensing of Phage Triggered Ion Cascade) technology was studied. The SEPTIC provides fast (within several minutes), effective (living cell only), phage specific (simple and less malfunction), cheap, compact and robust method for bacteria sensing. We fabricated a number of devices such as ‘Nanowell’, ‘Microwell’, and ‘ISFET’ which detect bacteria-phage reaction in frequency domain and time domain. In the frequency domain, the positive reaction showed much higher β (a characteristic of a noise) than background noise or negative reaction. For the time domain, we observed abnormal pulses lasting 0.1 ~ 0.3 s which match with the literatures. And the ISFET showed abnormal pulse in the drain current, which may be attributed to phage infection of bacteria.

CHAPTER VII

RAPID SENSING OF BACTERIA – CONCLUSION

7.1 Conclusion

Although several technologies are available for the identification of bacteria or viruses in humans, veterinary and agricultural diagnostic laboratories, such as culturing and polymerase chain reaction (PCR), these approaches have difficulties such as time required for culturing of bacteria, expensive instrumentation or poor selectivity between living and dead bacteria. Nanowell (or Microwell) is a device which enables a rapid and specific detection of bacteria using nano (or micro) scale probe to monitor the electric field fluctuations caused by ion leakage from the bacteria.

When a bacteriophage infects a bacterium and injects its DNA into the host cell, a massive, transitory ion efflux from the host cell occurs. SEPTIC (SEnsing of Phage-Triggered Ion Cascade) technology uses a nanowell device to detect the nano-scale electric field fluctuations caused by this ion efflux.⁴² Since one bacteriophage only infects one specific strand of bacteria and the ion efflux occurs within minutes after the infection, SEPTIC can identify different bacteria with trace quantities in several minutes (alternative methods need well-equipped laboratory circumstances, expensive instrumentation, hours to days of pre-process), with no false alarm or missed detection.

A novel bacteria detection and identification method SEPTIC technology was studied. The SEPTIC provides fast (within several minutes), effective (living cell only), phage specific (simple and less malfunction), cheap, compact and robust method for bacteria sensing. We fabricated a number of devices such as ‘Nanowell’, ‘Microwell’, and ‘ISFET’ which detect bacteria-phage reaction in frequency domain and time domain. In the frequency domain, the

positive reaction showed much higher β (a characteristic of a noise) than background noise or negative reaction. For the time domain, we observed abnormal pulses lasting 0.1 ~ 0.3 s which match with the literatures. And the ISFET showed the pulse in terms of the deviated drain current.⁶²

7.2 Future Application

Fluctuation analysis coupled with the unequalled specificity and avidity of bacteriophages may provide a diagnostic technology useful for clinical, veterinary, and agricultural practice, as well as in applications to biological threat detection and reduction in bio-defense. When the nanowell (or microwell) device is integrated with micro/nano channel which carries a collected bacterium to the pre-typed phage reaction site, it would allow the detection and identification of specific bacterium with much more portability within a few minutes.

REFERENCES

- ¹ X. Luo and T. Ishihara, *Appl. Phys. Lett.* **84**, 4780 (2004).
- ² Z. Liu, Q. Wei and X. Zhang, *Nano Lett.* **5**, 957 (2005).
- ³ G. T. di Francia, *Nuovo Cimento Suppl.* **9**, 426 (1952).
- ⁴ B. J. Lin, *Microelectronic Engineering* **6**, 31 (1987).
- ⁵ H. Bethe, *Phys. Rev.* **66**, 163 (1944).
- ⁶ J. B. Pendry, *Phys. Rev. Lett.* **85**, 3966 (2000).
- ⁷ N. Fang, H. Lee, C. Sun, and X. Zhang, *Science* **308**, 534 (2005).
- ⁸ D.O.S. Melville and R. J. Blaikie, *Opt. Express* **13**, 2127 (2005).
- ⁹ W. Srituravanich, N. Fang, C. Sun, Q. Luo, and X. Zhang, *Nano Lett.* **4**, 1085 (2004).
- ¹⁰ D. B. Shao and S. C. Chen, *Appl. Phys. Lett.* **86**, 253107 (2005).
- ¹¹ W. Srituravanich, S. Durant, H. Lee, C. Sun and X. Zhang, *J. Vac. Sci. Technol. B* **23**, 2636 (2005).
- ¹² S. Durant, N. Fang, and X. Zhang, *Appl. Phys. Lett.* **86**, 126101 (2005).
- ¹³ D. O. S. Melville, R. J. Blaikie, and C. R. Wolf, *Appl. Phys. Lett.* **84**, 4403 (2004).
- ¹⁴ V. M. Shalaev, *Nature Photonics* **1**, pp. 41-48 (2007).
- ¹⁵ H. F. Ghaemi, T. Thio, D. E. Grupp, and T. W. Ebbesen, *Phys. Rev. B* **58**, 6779 (1998).
- ¹⁶ Z. Liu, Q. Wei, and X. Zhang, *Nano Lett.* **5**, 957 (2005).
- ¹⁷ T. W. Ebbesen, H. Lezec, H. Ghami, T. Thio, and P. Wolff, *Nature (London)* **391**, 667 (1998).
- ¹⁸ D. E. Grupp, H. J. Lezec, T. Thio, and T. W. Ebbesen, *Adv. Mater.* **11**, 861 (1999).
- ¹⁹ P. T. Worthinga and W. L. Barnes, *Appl. Phys. Lett.* **79**, 3035 (2001).

- ²⁰ H. J. Lezec, A. Degiron, E. Devaux, R. A. Linke, L. Martin-Moreno, F. J. Garcia-Vidal, T. W. Ebbesen, *Science* **297**, 820 (2002).
- ²¹ C. Genet and T. W. Ebbesen, *Nature (London)* **445**, 39 (2007).
- ²² D. J. D. Carter, D. Gil, R. Menon, M. K. Mondol, and H. I. Smith, *J. Vac. Sci. Technol. B* **17**(6), 3449-3452 (2000).
- ²³ M. C. Petty, M. R. Bryce, and D. Bloor, *Introduction to Molecular Electronics* (Oxford University Press, New York, 1995).
- ²⁴ I. Willner, *Science* **298**, 2407 (2002).
- ²⁵ S. Caras and J. Janata, *Anal. Chem.* **52**, 1935 (1980).
- ²⁶ J. F. Schenck, U.S. Patent, 4,238,757 (1980).
- ²⁷ R. B. M. Schasfoort, P. Bergveld, R. P. H. Kooyman and J. Greve, *Analytica Chimica Acta.* **238**, 323 (1990)
- ²⁸ P. Bergveld, *Sensors and Actuators B* **88**, 1 (2003).
- ²⁹ H. Baltés and O. Brand, *Proc. of the 16th Instrumentation and Measurement Technology Conference*, pp. 54-59 (1999).
- ³⁰ I. Eisele, T. Doll and M. Burgmair, *Sensors and Actuators B* **78**, 19 (2001).
- ³¹ G. Sberveglieri, *Sensors and Actuators B* **23**, 103 (1995).
- ³² G. Schmera and L. B. Kish, *Fluctuation and Noise Letters* **2**, 117 (2002).
- ³³ C. Colapicchioni, A. Barbaro, F. Porcelli, and I. Giannini, *Sensors and Actuators B: Chemical* **4**, 245 (1991).
- ³⁴ H. L. Grossman, W. R. Myers, V. J. Vreeland, R. Bruehl, M. D. Alper, C. R. Bertozzi, and J. Clarke, *Proc. Natl. Acad. Sci. U.S.A.* **101**, 129 (2004).
- ³⁵ T. Tanaka, H. Takeda, F. Ueki, K. Obata, H. Tajima, H. Takeyama, Y. Goda, S. Fujimoto, T. Matsunaga, *J Biotechnol* **108**, 153 (2004).

- ³⁶ X. Zhao, L. R. Hilliard, S. J. Mechery, Y. Wang, R. P. Bagwe, S. Jin, and W. Tan., *Proc. Natl Acad. Sci. U.S.A.* **101**(42), 15027 (2004).
- ³⁷ R. Edgar, M. McKinstry, J. Hwang, A. B. Oppenheim, R. A. Fekete, G. Giulian, C. Merrill, K. Nagashima, and S. Adhya, *Proc. Natl Acad. Sci. U.S.A.* **103**, 4841 (2006).
- ³⁸ L. B. Kish, G. Schmera, and J. Smulko, *Nanotechnology E-Bulletin*, SPIE (2004).
- ³⁹ L. B. Kish, R. Vajtai, and C. -G. Granqvist, *Sensors and Actuators B* **71**, 55 (2000).
- ⁴⁰ J. Hecht, *Laser Focus World* **41**(4), 73 (2005).
- ⁴¹ W. L. Barnes, A. Dereux, and T. W. Ebbesen, *Nature (London)* **424**, 824 (2003).
- ⁴² P. M. Valanju, R. M. Walser, and A. P. Valanju, *Phys. Rev. Lett.* **88**, 187401 (2002).
- ⁴³ H. J. Lezec, A. Degiron, E. Devaux, R. A. Linke, L. Martin-Moreno, F. J. Garcia-Vidal, and T. W. Ebbesen, *Science* **297**, 820 (2002).
- ⁴⁴ A. Wong and T. Pistor, *TEMPEST Version 6.0 User Guide* (Electronics Research Laboratory, University of California, Berkeley, 2000).
- ⁴⁵ E. D. Palik, *Handbook of Optical Constants of Solids* (Academic Press, San Diego, 1998).
- ⁴⁶ M. Born and E. Wolf, *Principles of Optics*, 7-th ed. (Cambridge University Press, Cambridge, 1999).
- ⁴⁷ S. Seo, H. C. Kim, and M. Cheng, "Mid-field superresolution imaging using a plasmonic lens," *Nano Lett.*, submitted.
- ⁴⁸ E. Hecht, *Optics*, 4-th ed. (Addison Wesley, Boston, 2002).
- ⁴⁹ M. J. Weber, *Handbook of Optical Materials* (CRC Press, 2003).
- ⁵⁰ I. J. Djomehri, T. A. Savas, and H. Smith, *J. Vac. Sci. Technol. B* **16**(6), 3426 (1998).
- ⁵¹ S. Seo, H. C. Kim, H. Ko, and M. Cheng, "Sub-wavelength proximity nanolithography using a plasmonic lens", *J. Vac. Sci. Technol. B* , accepted and in-press.
- ⁵² J. Hecht, *Laser Focus World*, **41**(9) (2005).

- ⁵³ M. D. King, S. Seo, J. U. Kim, R. Young, M. Cheng, and L.B. Kish, *Journal of Biological Physics and Chemistry* **5**, 3 (2005).
- ⁵⁴ L. Prescott, *Microbiology* (Wm. C. Brown Publishers, Dubuque, ISBN 0-697-01372-3, 1993).
- ⁵⁵ S. Mc Grath and D. Van Sinderen(editors), *Bacteriophage: Genetics and Molecular Biology*, 1st ed.(Caister Academic Press, Norfolk, ISBN 978-1-904455-14-1, 2007).
- ⁵⁶ Image of Lambda Phage, Steve's Place (<http://www.steve.gb.com/images/science>).
- ⁵⁷ Image of T4 Phage, Science Museum of United Kingdom (<http://www.sciencemuseum.org.uk>).
- ⁵⁸ Image of T7 Phage, Wichita State University (<http://webs.wichita.edu/mschneegurt/biol103>).
- ⁵⁹ D. H. Duckworth and P. A. Gulig, *BioDrugs* **16**, 57 (2002).
- ⁶⁰ R. Schuch, D. Nelson and V.A. Fischetti, *Nature(London)* **418**, 884 (2002).
- ⁶¹ R. Stone, *Science* **298**, 728 (2002).
- ⁶² S. Seo, H. C. Kim, M. Cheng, X. Ruan, and W. Ruan, *J. Vac. Sci. Technol. B* **24**(6), 3133 (2006).

APPENDIX A
WAVEVECTORS AND OPTICAL PROPERTY
OF HIGHLY CONDUCTIVE MATERIALS

- A.1. Silver (Ag) interfaced with air ($n=1$)
- A.2. Aluminum (Al) interfaced with air ($n=1$)
- A.3. Chromium (Cr) interfaced with air ($n=1$)
- A.4. Titanium (Ti) interfaced with air ($n=1$)

A.1. Silver (Ag) interfaced with air (n=1)

wavelength [nm]	n	k	$\varepsilon = \varepsilon' + i \varepsilon''$		Ksp,x [ko]		Ksp,zd [ko]		Ksp,zm [ko]	
			ε'	ε''	Re	Im	Re	Im	Re	Im
827	0.27	5.79	-33.451	3.127	1.015	0.001	0.008	-0.175	0.266	5.878
620	0.27	4.18	-17.400	2.257	1.030	0.004	0.017	-0.245	0.261	4.304
496	0.24	3.09	-9.491	1.483	1.056	0.010	0.029	-0.339	0.224	3.264
413	0.23	2.27	-5.100	1.044	1.109	0.026	0.061	-0.482	0.195	2.523
381	0.23	1.86	-3.407	0.856	1.171	0.056	0.106	-0.617	0.165	2.192
354	0.21	1.42	-1.972	0.596	1.333	0.172	0.254	-0.901	0.036	1.929
344	0.23	1.13	-1.224	0.520	1.423	0.570	0.731	-1.110	0.317	-1.739
335	0.30	0.77	-0.503	0.462	0.681	0.737	1.130	-0.444	0.363	-0.745
329	0.53	0.40	0.121	0.424	0.542	0.272	0.899	-0.164	0.178	0.361
326	0.73	0.30	0.443	0.438	0.624	0.154	0.806	-0.120	0.409	0.300
318	1.30	0.36	1.560	0.936	0.813	0.077	0.596	-0.106	1.029	0.393
310	1.61	0.60	2.232	1.932	0.882	0.077	0.497	-0.137	1.374	0.654
302	1.73	0.85	2.270	2.941	0.915	0.083	0.445	-0.171	1.513	0.922
295	1.75	1.06	1.939	3.710	0.936	0.088	0.414	-0.200	1.545	1.147
288	1.73	1.13	1.716	3.910	0.943	0.092	0.406	-0.212	1.527	1.224
276	1.69	1.28	1.218	4.326	0.957	0.096	0.387	-0.237	1.494	1.386
261	1.61	1.34	0.797	4.315	0.964	0.103	0.385	-0.257	1.414	1.456
248	1.55	1.36	0.553	4.216	0.967	0.108	0.387	-0.270	1.352	1.482
225	1.45	1.34	0.307	3.886	0.968	0.119	0.401	-0.288	1.243	1.470
207	1.34	1.28	0.157	3.430	0.964	0.136	0.427	-0.307	1.119	1.416
191	1.25	1.18	0.170	2.950	0.953	0.154	0.464	-0.315	1.009	1.316
177	1.18	1.06	0.269	2.502	0.932	0.171	0.509	-0.312	0.918	1.189
165	1.14	0.91	0.472	2.075	0.897	0.179	0.557	-0.288	0.860	1.020
155	1.16	0.75	0.783	1.740	0.860	0.163	0.587	-0.239	0.875	0.834
138	1.33	0.56	1.455	1.490	0.845	0.107	0.568	-0.159	1.064	0.615
124	1.46	0.56	1.818	1.635	0.862	0.089	0.535	-0.144	1.208	0.613
113	1.52	0.56	1.997	1.702	0.869	0.083	0.521	-0.138	1.274	0.612
103	1.61	0.59	2.244	1.900	0.881	0.076	0.498	-0.135	1.374	0.643
95	1.66	0.64	2.346	2.125	0.890	0.076	0.482	-0.140	1.429	0.696
89	1.72	0.78	2.350	2.683	0.908	0.080	0.455	-0.160	1.499	0.846
86	1.64	0.88	1.915	2.886	0.914	0.094	0.457	-0.188	1.417	0.958
83	1.56	0.92	1.587	2.870	0.915	0.105	0.465	-0.207	1.331	1.006

A.2. Aluminum (Al) interfaced with air (n=1)

wavelength [nm]	n	k	$\varepsilon = \varepsilon' + i \varepsilon''$		Ksp,x [ko]		Ksp,zd [ko]		Ksp,zm [ko]	
			ε'	ε''	Re	Im	Re	Im	Re	Im
827	2.75	8.31	-61.505	45.616	1.005	0.004	0.037	-0.109	2.727	8.364
775	2.63	8.60	-67.018	45.134	1.005	0.004	0.033	-0.107	2.608	8.651
729	2.14	8.57	-68.904	36.744	1.006	0.003	0.028	-0.110	2.129	8.628
689	1.74	8.21	-64.291	28.570	1.007	0.003	0.025	-0.117	1.728	8.264
653	1.49	7.82	-58.954	23.275	1.007	0.003	0.024	-0.124	1.476	7.883
620	1.30	7.48	-54.235	19.505	1.008	0.003	0.023	-0.131	1.292	7.545
564	1.02	6.85	-45.831	13.939	1.010	0.003	0.022	-0.144	1.007	6.919
517	0.83	6.28	-38.794	10.380	1.012	0.003	0.021	-0.158	0.815	6.363
477	0.70	5.80	-33.157	8.062	1.015	0.004	0.021	-0.172	0.684	5.887
443	0.60	5.39	-28.641	6.441	1.017	0.004	0.021	-0.187	0.587	5.479
413	0.52	5.02	-24.967	5.255	1.020	0.004	0.022	-0.201	0.512	5.125
387	0.46	4.71	-21.954	4.331	1.023	0.005	0.022	-0.215	0.449	4.817
365	0.41	4.43	-19.424	3.603	1.026	0.005	0.022	-0.230	0.396	4.542
344	0.36	4.17	-17.291	3.030	1.029	0.005	0.023	-0.245	0.351	4.298
326	0.33	3.95	-15.465	2.573	1.033	0.006	0.023	-0.260	0.314	4.078
310	0.29	3.74	-13.901	2.199	1.037	0.006	0.023	-0.275	0.282	3.880
295	0.27	3.55	-12.545	1.897	1.041	0.007	0.024	-0.291	0.254	3.701
282	0.24	3.38	-11.365	1.649	1.046	0.007	0.024	-0.308	0.231	3.537
270	0.22	3.22	-10.332	1.437	1.051	0.008	0.025	-0.325	0.210	3.388
258	0.21	3.08	-9.420	1.261	1.057	0.008	0.026	-0.342	0.191	3.252
155	0.07	1.66	-2.760	0.240	1.249	0.030	0.051	-0.749	0.039	2.078
146	0.06	1.53	-2.328	0.192	1.319	0.041	0.062	-0.861	0.021	2.016
138	0.06	1.40	-1.963	0.157	1.420	0.058	0.082	-1.009	0.002	-1.994
131	0.05	1.29	-1.651	0.126	1.577	0.091	0.117	-1.222	0.039	-2.033
124	0.04	1.18	-1.386	0.104	1.857	0.175	0.207	-1.569	0.124	-2.195
118	0.04	1.08	-1.156	0.086	2.491	0.543	0.590	-2.293	0.485	-2.702
113	0.04	0.98	-0.957	0.071	1.780	2.910	3.035	-1.707	2.784	-1.847
108	0.03	0.88	-0.779	0.058	0.305	1.821	2.073	-0.268	1.598	-0.330
103	0.03	0.79	-0.625	0.052	0.142	1.278	1.620	-0.112	1.006	-0.155
99	0.03	0.70	-0.489	0.048	0.093	0.974	1.394	-0.065	0.679	-0.098
95	0.04	0.61	-0.369	0.046	0.076	0.764	1.257	-0.046	0.462	-0.075
92	0.04	0.52	-0.266	0.042	0.065	0.601	1.166	-0.034	0.308	-0.058
89	0.05	0.42	-0.172	0.040	0.064	0.457	1.098	-0.027	0.187	-0.049
87	0.05	0.37	-0.136	0.040	0.066	0.400	1.075	-0.025	0.146	-0.046
86	0.06	0.33	-0.104	0.038	0.069	0.344	1.056	-0.022	0.109	-0.042
85	0.07	0.27	-0.070	0.037	0.075	0.282	1.036	-0.020	0.072	-0.039
84	0.09	0.21	-0.037	0.036	0.092	0.213	1.019	-0.019	0.037	-0.038
83	0.13	0.15	-0.008	0.038	0.128	0.151	1.003	-0.019	0.007	-0.039

A.3. Chromium (Cr) interfaced with air (n=1)

wavelength [nm]	n	k	$\varepsilon = \varepsilon' + i \varepsilon''$		Ksp,x [ko]		Ksp,zd [ko]		Ksp,zm [ko]	
			ε'	ε''	Re	Im	Re	Im	Re	Im
849	4.31	4.32	-0.086	37.238	1.000	0.013	0.117	-0.114	4.251	4.377
700	3.84	4.37	-4.351	33.562	1.002	0.015	0.116	-0.128	3.782	4.434
620	3.48	4.36	-6.899	30.346	1.003	0.016	0.114	-0.139	3.422	4.429
564	3.18	4.41	-9.336	28.048	1.005	0.016	0.111	-0.148	3.124	4.484
517	2.75	4.46	-12.329	24.530	1.008	0.017	0.104	-0.162	2.697	4.541
477	2.22	4.36	-14.081	19.358	1.012	0.018	0.097	-0.183	2.170	4.452
443	1.80	4.06	-13.244	14.616	1.017	0.020	0.097	-0.208	1.750	4.164
413	1.54	3.71	-11.393	11.427	1.022	0.023	0.103	-0.233	1.487	3.827
387	1.44	3.40	-9.486	9.792	1.025	0.028	0.115	-0.253	1.380	3.527
365	1.39	3.24	-8.566	9.007	1.028	0.032	0.123	-0.264	1.326	3.373
344	1.26	3.12	-8.147	7.862	1.032	0.034	0.124	-0.281	1.195	3.262
326	1.12	2.95	-7.448	6.608	1.038	0.037	0.128	-0.303	1.052	3.103
310	1.02	2.76	-6.577	5.630	1.044	0.043	0.137	-0.328	0.947	2.926
295	0.94	2.58	-5.773	4.850	1.052	0.050	0.148	-0.354	0.860	2.760
282	0.90	2.42	-5.046	4.356	1.057	0.058	0.164	-0.376	0.811	2.611
276	0.89	2.35	-4.730	4.183	1.060	0.063	0.173	-0.386	0.795	2.546
270	0.88	2.28	-4.424	4.013	1.062	0.068	0.182	-0.395	0.780	2.481
264	0.86	2.21	-4.145	3.801	1.065	0.073	0.192	-0.407	0.754	2.417
258	0.86	2.13	-3.797	3.664	1.067	0.081	0.207	-0.418	0.745	2.342
253	0.86	2.07	-3.545	3.560	1.068	0.087	0.219	-0.425	0.738	2.285
248	0.85	2.01	-3.318	3.417	1.070	0.094	0.231	-0.435	0.721	2.230
243	0.86	1.94	-3.024	3.337	1.069	0.102	0.248	-0.441	0.721	2.163
238	0.87	1.87	-2.740	3.254	1.068	0.112	0.268	-0.447	0.720	2.094
230	0.93	1.80	-2.375	3.348	1.058	0.121	0.293	-0.437	0.767	2.017
221	0.95	1.74	-2.125	3.306	1.053	0.129	0.312	-0.435	0.776	1.955
214	0.97	1.74	-2.087	3.376	1.050	0.128	0.313	-0.429	0.796	1.951
207	0.94	1.73	-2.109	3.252	1.054	0.131	0.314	-0.439	0.765	1.946
200	0.89	1.69	-2.064	3.008	1.060	0.139	0.323	-0.457	0.708	1.916
194	0.85	1.66	-2.033	2.822	1.066	0.147	0.330	-0.473	0.663	1.894
188	0.80	1.59	-1.888	2.544	1.072	0.163	0.353	-0.497	0.598	1.835
182	0.75	1.51	-1.718	2.265	1.078	0.186	0.383	-0.524	0.527	1.767
177	0.74	1.45	-1.555	2.146	1.074	0.203	0.411	-0.531	0.500	1.708
172	0.71	1.39	-1.428	1.974	1.075	0.225	0.442	-0.548	0.450	1.654
168	0.69	1.33	-1.293	1.835	1.071	0.248	0.476	-0.558	0.409	1.595
163	0.66	1.23	-1.077	1.624	1.056	0.291	0.541	-0.568	0.339	1.490
159	0.67	1.15	-0.874	1.541	1.023	0.315	0.592	-0.545	0.323	1.388
155	0.68	1.07	-0.683	1.455	0.984	0.333	0.638	-0.514	0.312	1.279
151	0.71	1.00	-0.496	1.420	0.942	0.332	0.666	-0.470	0.337	1.178
146	0.74	0.92	-0.299	1.362	0.898	0.323	0.690	-0.421	0.367	1.065
138	0.83	0.81	0.033	1.345	0.847	0.276	0.689	-0.340	0.479	0.915
131	0.92	0.74	0.299	1.362	0.829	0.232	0.670	-0.287	0.591	0.827
124	0.98	0.73	0.428	1.431	0.834	0.210	0.650	-0.270	0.663	0.814
118	1.01	0.72	0.502	1.454	0.834	0.199	0.641	-0.260	0.699	0.802
113	1.05	0.69	0.626	1.449	0.831	0.184	0.633	-0.241	0.746	0.766
108	1.09	0.69	0.712	1.504	0.837	0.173	0.620	-0.234	0.793	0.766
103	1.13	0.70	0.787	1.582	0.845	0.164	0.605	-0.229	0.839	0.777
99	1.15	0.73	0.790	1.679	0.854	0.163	0.594	-0.235	0.863	0.811
95	1.15	0.77	0.730	1.771	0.864	0.167	0.586	-0.247	0.864	0.857
92	1.12	0.80	0.614	1.792	0.868	0.177	0.588	-0.262	0.831	0.893
89	1.09	0.82	0.516	1.788	0.871	0.187	0.593	-0.275	0.796	0.918
86	1.03	0.82	0.389	1.689	0.867	0.204	0.611	-0.289	0.726	0.921

A.4. Titanium (Ti) interfaced with air (n=1)

wavelength [nm]	n	k	$\varepsilon = \varepsilon' + i \varepsilon''$		Ksp,x [ko]		Ksp,zd [ko]		Ksp,zm [ko]	
			ε'	ε''	Re	Im	Re	Im	Re	Im
827	2.98	3.32	-2.142	19.787	1.002	0.025	0.154	-0.163	2.902	3.401
775	2.74	3.30	-3.382	18.084	1.004	0.027	0.154	-0.176	2.662	3.387
729	2.54	3.23	-3.981	16.408	1.006	0.029	0.157	-0.188	2.460	3.323
689	2.36	3.11	-4.103	14.679	1.007	0.032	0.163	-0.201	2.277	3.209
653	2.22	2.99	-4.012	13.276	1.009	0.036	0.169	-0.212	2.133	3.095
620	2.11	2.88	-3.842	12.154	1.010	0.039	0.176	-0.222	2.020	2.990
590	2.01	2.77	-3.633	11.135	1.011	0.042	0.183	-0.232	1.915	2.885
564	1.92	2.67	-3.443	10.253	1.012	0.046	0.191	-0.242	1.821	2.790
539	1.86	2.56	-3.094	9.523	1.012	0.050	0.201	-0.250	1.756	2.683
517	1.81	2.47	-2.825	8.941	1.012	0.053	0.209	-0.256	1.701	2.596
496	1.78	2.39	-2.544	8.508	1.012	0.056	0.218	-0.261	1.667	2.518
477	1.75	2.34	-2.413	8.190	1.012	0.059	0.224	-0.265	1.634	2.470
459	1.71	2.29	-2.320	7.832	1.012	0.061	0.229	-0.271	1.591	2.423
443	1.68	2.25	-2.240	7.560	1.013	0.064	0.234	-0.275	1.558	2.385
428	1.63	2.21	-2.227	7.205	1.014	0.067	0.239	-0.283	1.505	2.349
413	1.59	2.17	-2.181	6.901	1.014	0.069	0.244	-0.289	1.462	2.312
400	1.55	2.15	-2.220	6.665	1.016	0.072	0.246	-0.295	1.421	2.295
387	1.50	2.12	-2.244	6.360	1.017	0.074	0.250	-0.303	1.368	2.269
376	1.44	2.09	-2.295	6.019	1.020	0.078	0.253	-0.314	1.306	2.244
365	1.37	2.06	-2.367	5.644	1.023	0.082	0.257	-0.326	1.234	2.220
354	1.30	2.01	-2.350	5.226	1.027	0.087	0.264	-0.340	1.159	2.177
344	1.24	1.96	-2.304	4.861	1.030	0.093	0.271	-0.354	1.094	2.134
335	1.17	1.90	-2.241	4.446	1.034	0.101	0.281	-0.371	1.018	2.082
326	1.11	1.83	-2.117	4.063	1.037	0.110	0.295	-0.388	0.949	2.020
322	1.08	1.78	-2.002	3.845	1.038	0.117	0.307	-0.397	0.912	1.974
318	1.06	1.73	-1.869	3.668	1.038	0.124	0.320	-0.404	0.885	1.927
310	1.04	1.62	-1.543	3.370	1.033	0.140	0.351	-0.412	0.847	1.818
295	1.06	1.45	-0.979	3.074	1.012	0.161	0.405	-0.402	0.839	1.637
282	1.13	1.33	-0.492	3.006	0.986	0.164	0.437	-0.370	0.896	1.497
270	1.17	1.29	-0.295	3.019	0.976	0.161	0.445	-0.353	0.934	1.447
258	1.21	1.23	-0.049	2.977	0.963	0.158	0.457	-0.334	0.971	1.376
248	1.24	1.21	0.074	3.001	0.958	0.154	0.458	-0.323	1.002	1.351
238	1.27	1.20	0.173	3.048	0.955	0.150	0.456	-0.313	1.034	1.336
230	1.17	1.16	0.023	2.714	0.952	0.169	0.483	-0.334	0.918	1.303
221	1.24	1.21	0.074	3.001	0.958	0.154	0.458	-0.323	1.002	1.351
214	1.21	1.22	-0.024	2.952	0.961	0.159	0.460	-0.332	0.970	1.365
207	1.15	1.21	-0.142	2.783	0.963	0.170	0.472	-0.348	0.902	1.361
200	1.11	1.18	-0.160	2.620	0.960	0.180	0.487	-0.355	0.853	1.333
194	1.08	1.14	-0.133	2.462	0.953	0.190	0.505	-0.358	0.814	1.291
188	1.04	1.06	-0.042	2.205	0.936	0.204	0.539	-0.354	0.757	1.204
182	1.05	1.02	0.062	2.142	0.925	0.203	0.550	-0.341	0.764	1.156
177	1.06	0.97	0.183	2.056	0.911	0.201	0.562	-0.325	0.771	1.096
172	1.07	0.95	0.242	2.033	0.906	0.198	0.565	-0.317	0.781	1.072
168	1.11	0.94	0.349	2.087	0.904	0.187	0.557	-0.303	0.827	1.057
163	1.09	0.92	0.342	2.006	0.898	0.192	0.568	-0.303	0.802	1.035
159	1.11	0.93	0.367	2.065	0.901	0.187	0.560	-0.301	0.826	1.045
155	1.10	0.94	0.326	2.068	0.903	0.190	0.560	-0.306	0.816	1.058
151	1.10	0.95	0.308	2.090	0.906	0.190	0.557	-0.309	0.816	1.070
148	1.08	0.95	0.264	2.052	0.906	0.195	0.562	-0.314	0.793	1.071
144	1.04	0.96	0.160	1.997	0.908	0.206	0.570	-0.328	0.747	1.086
141	1.02	0.95	0.138	1.938	0.905	0.212	0.579	-0.331	0.722	1.076
138	1.00	0.94	0.116	1.880	0.902	0.218	0.588	-0.335	0.697	1.066

135	0.97	0.93	0.076	1.804	0.899	0.227	0.600	-0.341	0.660	1.057
132	0.95	0.91	0.074	1.729	0.892	0.234	0.613	-0.341	0.634	1.034
129	0.94	0.90	0.074	1.692	0.888	0.237	0.619	-0.340	0.621	1.022
127	0.91	0.88	0.054	1.602	0.880	0.248	0.636	-0.343	0.583	1.000
124	0.89	0.88	0.018	1.566	0.880	0.255	0.643	-0.349	0.558	1.001
122	0.86	0.85	0.017	1.462	0.866	0.266	0.664	-0.347	0.519	0.965
119	0.85	0.83	0.034	1.411	0.857	0.269	0.674	-0.342	0.505	0.940
117	0.81	0.79	0.032	1.280	0.836	0.283	0.704	-0.337	0.453	0.890
115	0.80	0.76	0.062	1.216	0.821	0.284	0.717	-0.326	0.441	0.851
113	0.79	0.72	0.106	1.138	0.800	0.282	0.731	-0.309	0.429	0.799
111	0.81	0.69	0.180	1.118	0.791	0.268	0.729	-0.290	0.456	0.762
109	0.81	0.69	0.180	1.118	0.791	0.268	0.729	-0.290	0.456	0.762
107	0.79	0.68	0.162	1.074	0.782	0.274	0.740	-0.290	0.431	0.749
105	0.78	0.67	0.160	1.045	0.775	0.277	0.747	-0.287	0.419	0.735
103	0.77	0.65	0.170	1.001	0.764	0.276	0.756	-0.279	0.408	0.709
97	0.76	0.55	0.275	0.836	0.717	0.251	0.776	-0.232	0.407	0.585
94	0.76	0.52	0.307	0.790	0.705	0.240	0.779	-0.217	0.411	0.549
91	0.76	0.48	0.347	0.730	0.691	0.225	0.783	-0.198	0.417	0.503
89	0.77	0.45	0.390	0.693	0.684	0.210	0.781	-0.184	0.432	0.469
86	0.77	0.42	0.417	0.647	0.675	0.198	0.783	-0.170	0.436	0.436
84	0.79	0.38	0.480	0.600	0.671	0.175	0.777	-0.152	0.464	0.394

APPENDIX B

TEMPEST INPUT SOURCE CODE

Simulation Parameters;

- Material: Ti, Incident Wavelength: 405 nm, Node Size: 30nm
- $a = 150$ nm (ring width), $r = 3$ μ m (ring radius), $t = 100$ nm (metal thickness)

wavelength 0.405

x_node 267

y_node 267

z_node 200

x_dim 8.0

plane_source xy position 0 8 0 8 0.2 1 0 0 1 0 uniform 0 0

plane_source xy position 0 8 0 8 0.2 0 1 0 1 90 uniform 0 0

rectangle position 0 8 0 8 0.0 6.0 index 1.0 0.0

rectangle position 0 8 0 8 0.1 0.4 index 1.47 0.0

rectangle position 0 8 0 8 0.4 0.5 dispersive 1.57 2.16

zylinder position 3.07 0.4 0.5 4 4 index 1.0 0.0

zylinder position 2.92 0.4 0.5 4 4 dispersive 1.57 2.16

rectangle position 0 8 0 8 0.0 0.1 pml 0 0 -1 2.16 1 0 0

rectangle position 0 8 0 8 5.9 6.0 pml 0 0 1 1.0 1 0 0

plot ex steady 0.00 position 0 8 4 4 0.1 5.9 exi

plot ey steady 0.00 position 0 8 4 4 0.1 5.9 eyi

plot ez steady 0.00 position 0 8 4 4 0.1 5.9 ezi

plot ex steady 0.25 position 0 8 4 4 0.1 5.9 exq

plot ey steady 0.25 position 0 8 4 4 0.1 5.9 eyq

plot ez steady 0.25 position 0 8 4 4 0.1 5.9 ezq

plot ex steady 0.00 position 0 8 0 8 0.52 0.52 gxi

plot ey steady 0.00 position 0 8 0 8 0.52 0.52 gyi

plot ez steady 0.00 position 0 8 0 8 0.52 0.52 gzi

plot ex steady 0.25 position 0 8 0 8 0.52 0.52 gxq

plot ey steady 0.25 position 0 8 0 8 0.52 0.52 gyq

plot ez steady 0.25 position 0 8 0 8 0.52 0.52 gzq

plot refractive position 0 8 4 4 0 6 ri1

plot refractive position 0 8 0 8 0.52 0.52 ri2

APPENDIX C
MATLAB SCRIPT FILES ⁵⁴

C.1. Plotam6.m

C.2. Plotbin.m

C.3. Fwhm.m

C.1. Plotam6.m

```

function [x,y,g] = plotam6(file,dx);
% comment
fp1=fopen([file 'xi']);
fp2=fopen([file 'xq']);
fp3=fopen([file 'yi']);
fp4=fopen([file 'yq']);
fp5=fopen([file 'zi']);
fp6=fopen([file 'zq']);
size1=fread(fp1,3,'int')
size2=fread(fp2,3,'int')
size3=fread(fp3,3,'int')
size4=fread(fp4,3,'int')
size5=fread(fp5,3,'int')
size6=fread(fp6,3,'int')

[ff,ms]=min(size1);

if ms==1
    nx=size1(2);
    ny=size1(3);
    xlab='y axis (nodes)';
    ylab='z axis (nodes)';
end

if ms==2
    nx=size2(1);
    ny=size2(3);
    xlab='x axis (nodes)';
    ylab='z axis (nodes)';
end

if ms==3
    nx=size1(1);
    ny=size1(2);
    xlab='x axis (nodes)';
    ylab='y axis (nodes)';
end

%nx=401; ny=401;
disp([nx ny])

a=fread(fp1,[nx ny],'single');
b=fread(fp2,[nx ny],'single');
c=fread(fp3,[nx ny],'single');
d=fread(fp4,[nx ny],'single');
e=fread(fp5,[nx ny],'single');
f=fread(fp6,[nx ny],'single');
size(a)

a=a(:,1);
b=b(:,1);
c=c(:,1);
d=d(:,1);

```

```
e=e(:,1);
f=f(:,1);
g=a.*a+b.*b+c.*c+d.*d+e.*e+f.*f;
g=0.5*g;
x=dx*(0:(nx-1)); y=dy*(0:(ny-1));
pcolor(x,y,g); shading('flat'); caxis([0 2*mean(g(:))]); %colormap('hot');
axis equal
colorbar;
xlabel(xlab);
ylabel(ylab);
title('<|E|^2>');

fclose(fp1);
fclose(fp2);
fclose(fp3);
fclose(fp4);
fclose(fp5);
fclose(fp6);
```

C.2. Plotbin.m

```
function a=plotbin(file1)
% comment
fp1=fopen(file1);
size1=fread(fp1,3,'int')

if size1(1)==1
    nx=size1(2);
    ny=size1(3);
    xlab='y axis (nodes)';
    ylab='z axis (nodes)';
end

if size1(2)==1
    nx=size1(1);
    ny=size1(3);
    xlab='x axis (nodes)';
    ylab='z axis (nodes)';
end

if size1(3)==1
    nx=size1(1);
    ny=size1(2);
    xlab='x axis (nodes)';
    ylab='y axis (nodes)';
end

a=fread(fp1,[nx ny],'float');
if ny==1,
    plot(a);
else
    pcolor(a);
    %axis('equal');
    colormap('hot');
    shading('flat');
    colorbar;
    xlabel(xlab);
    ylabel(ylab);
end
title('Electric Field');
fclose(fp1);
```

C.3. Fwhm.m

```

function width = fwhm(x,y)

y = y / max(y);
N = length(y);
lev50 = 0.5;

if y(1) < lev50
    [garbage,centerindex]=max(y);
    Pol = +1;
    disp('Pulse Polarity = Positive')

else
    [garbage,centerindex]=min(y);
    Pol = -1;
    disp('Pulse Polarity = Negative')
end

i = 2;
while sign(y(i)-lev50) == sign(y(i-1)-lev50)
    i = i+1;
end    %first crossing is between v(i-1) & v(i)

interp = (lev50-y(i-1)) / (y(i)-y(i-1));
tlead = x(i-1) + interp*(x(i)-x(i-1));
i = centerindex+1;
while ((sign(y(i)-lev50) == sign(y(i-1)-lev50)) & (i <= N-1))
    i = i+1;
end

if i ~= N
    Ptype = 1;
    disp('Pulse is Impulse or Rectangular with 2 edges')
    interp = (lev50-y(i-1)) / (y(i)-y(i-1));
    ttrail = x(i-1) + interp*(x(i)-x(i-1));
    width = ttrail - tlead;

else
    Ptype = 2;
    disp('Step-Like Pulse, no second edge')
    ttrail = NaN;
    width = NaN;

end

```


APPENDIX D**FDTD (FINITE-DIFFERENCE-TIME-DOMAIN) SIMULATIONS**

D.1. Light interaction after a tiny hole on highly conductive metals

D.1.1. A hole in a silver (Ag) layer

D.1.2. A hole in an aluminum (Al) layer

D.1.3. A hole in a chromium (Cr) layer

D.1.4. A hole in a titanium (Ti) layer

D.2. Light interaction after a simple ring on highly conductive metals

D.2.1. A ring in a silver (Ag) layer

D.2.2. A ring in an aluminum (Al) layer

D.2.3. A ring in a chromium (Cr) layer

D.2.4. A ring in a titanium (Ti) layer

Abbreviations;

W : width of hole or ring (e.g. W50 = 50 nm width)

T : thickness of metal layer (e.g. T60 = 60 nm thickness)

R : radius of ring (e.g. R1K = 1000 nm radius)

Plot data : light intensity $\langle |E|^2 \rangle$ in arbitrary unit (a.u.)

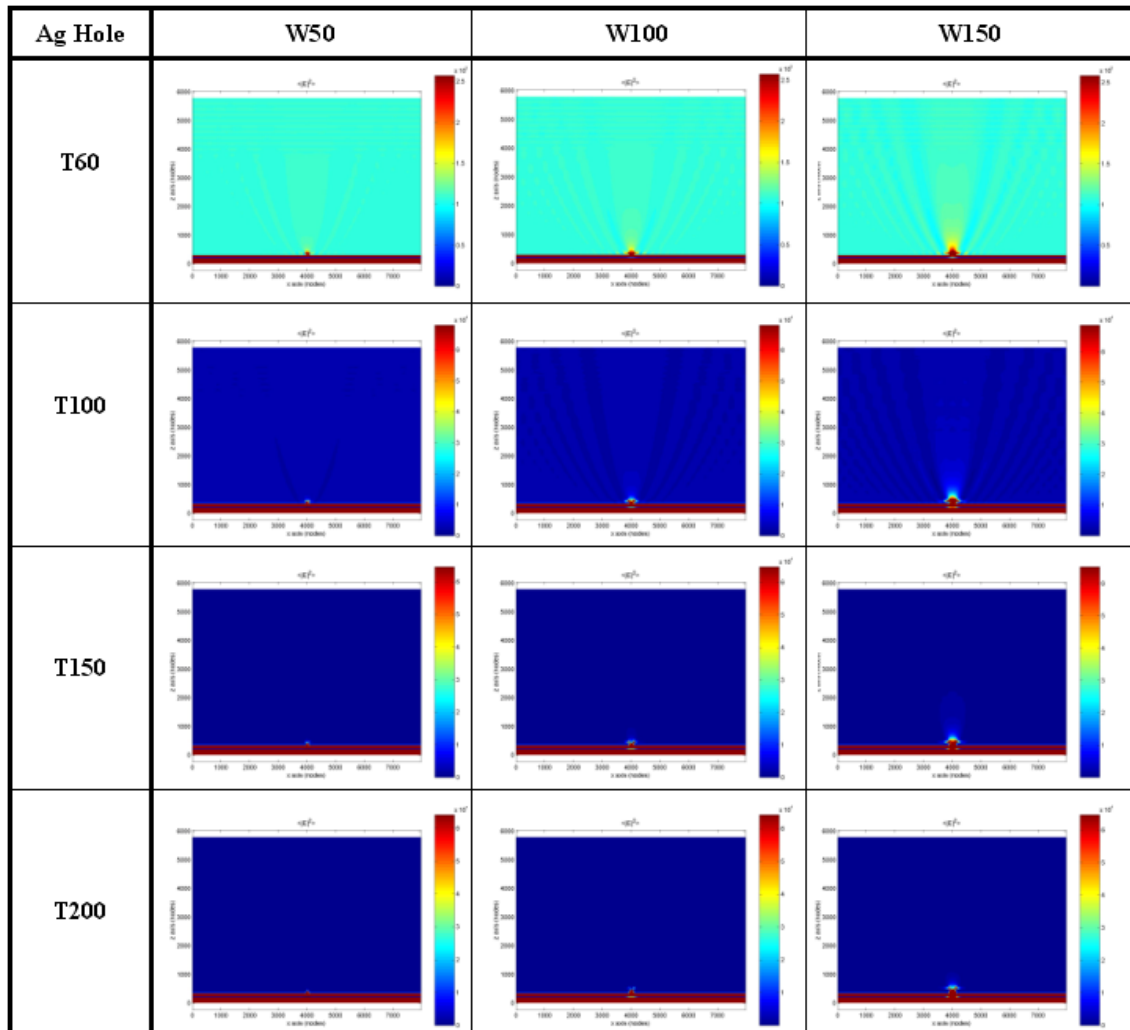
Plot direction : XZ plane in nm dimension

Simulation domain : (8000 nm, 8000 nm, 6000 nm)

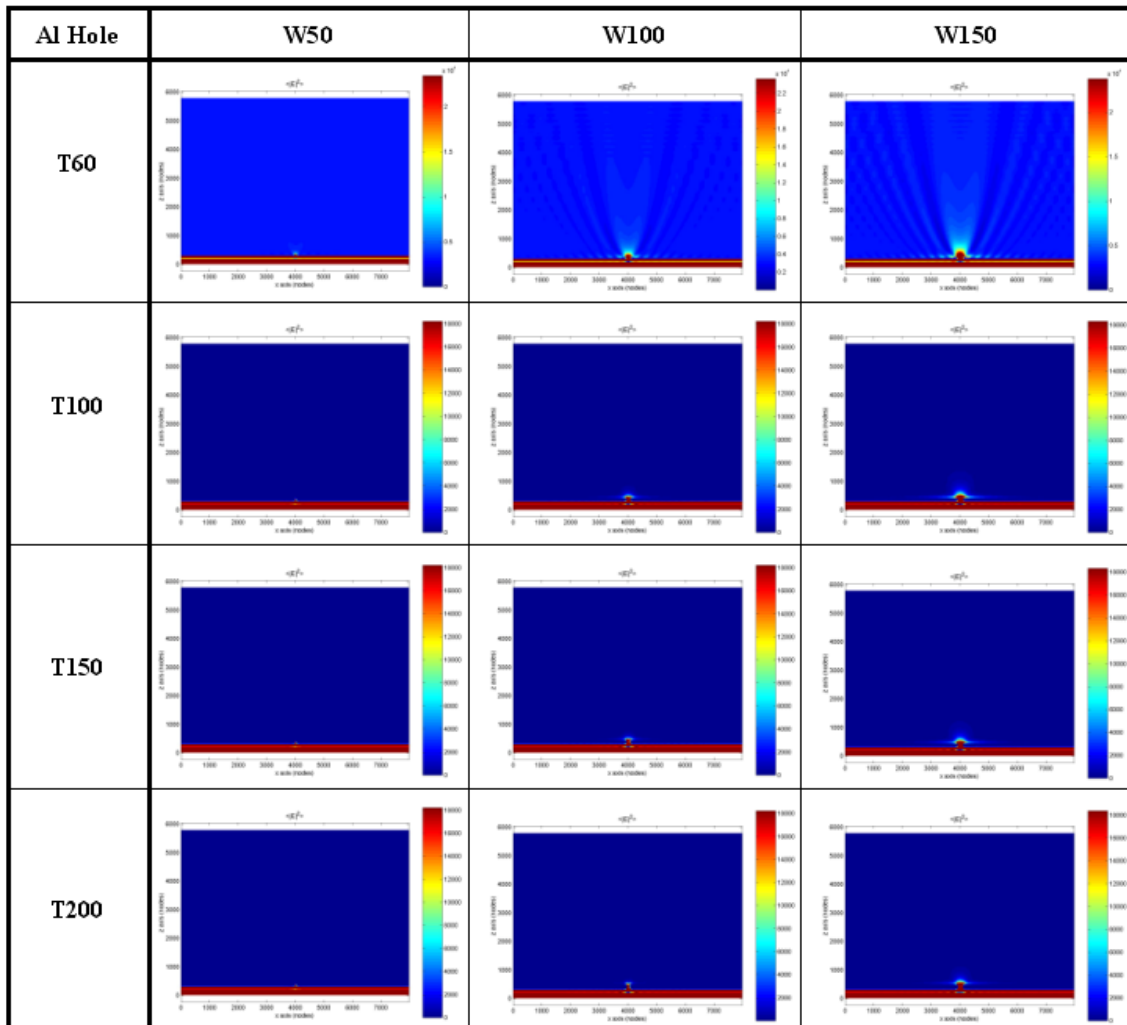
Domain center : (4000 nm, 4000 nm) central point in XY plane

D.1. Light interaction after a tiny hole on highly conductive metals

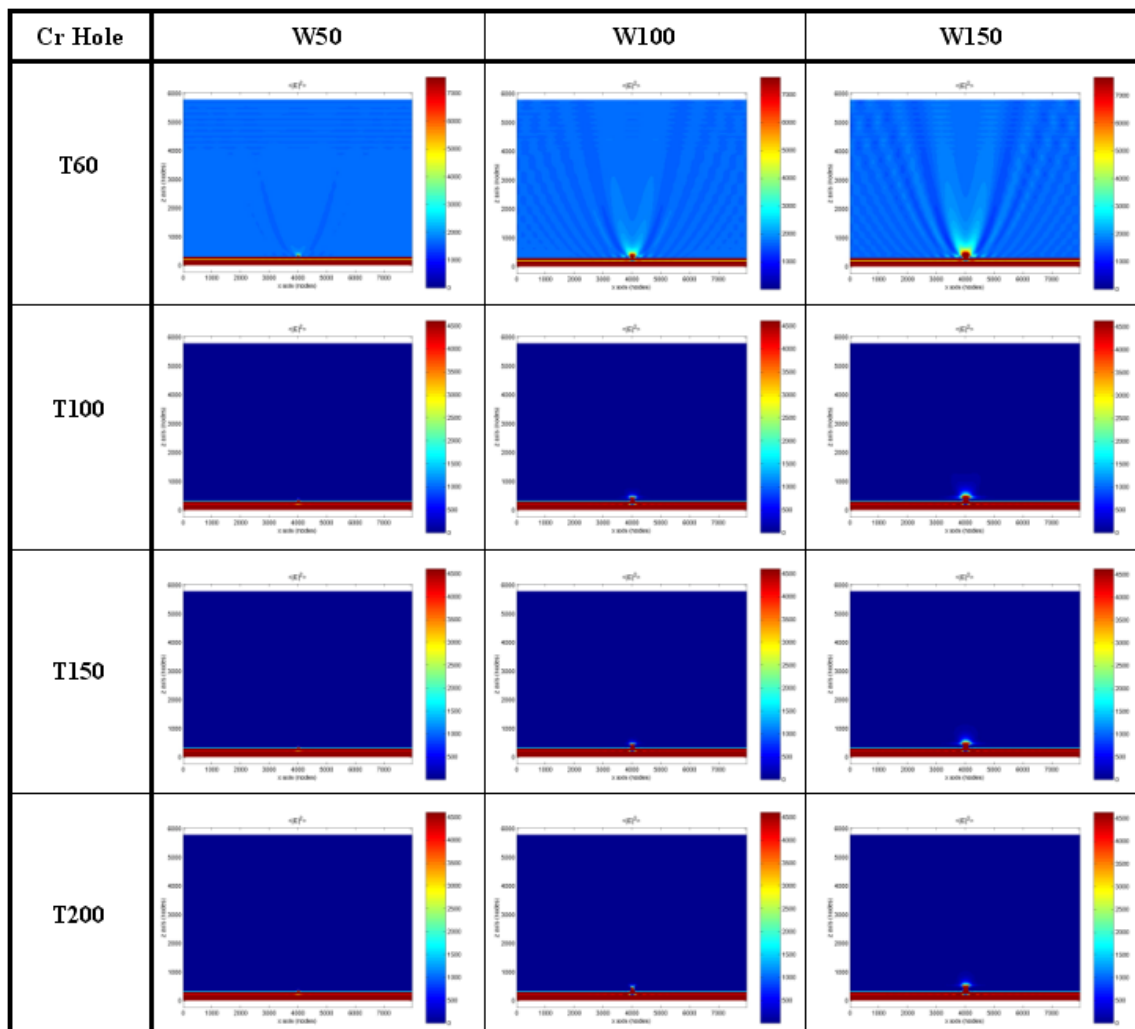
D.1.1. A hole in a silver (Ag) layer



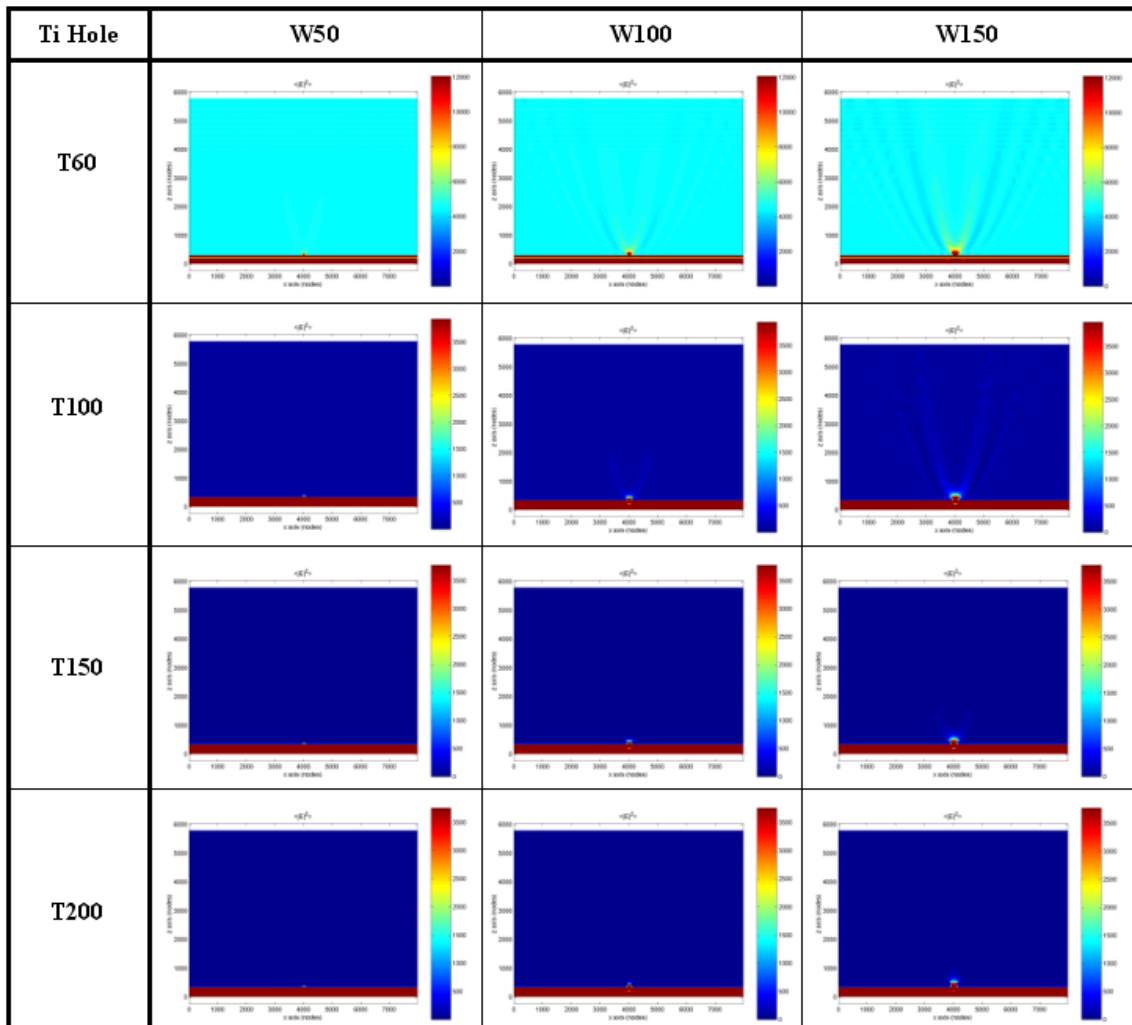
D.1.2. A hole in an aluminum (Al) layer



D.1.3. A hole in a chromium (Cr) layer



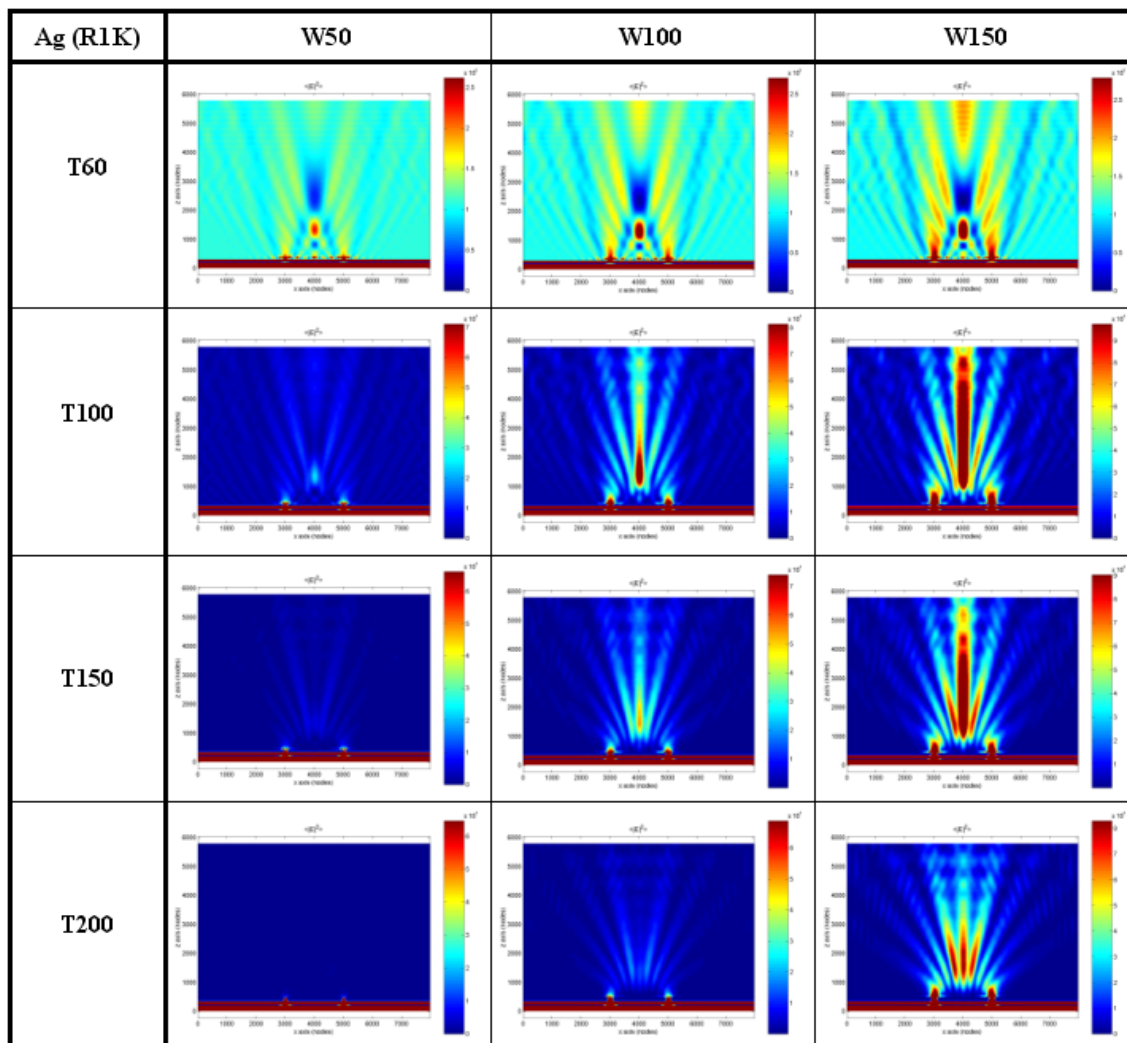
D.1.4. A hole in a titanium (Ti) layer



D.2. Light interaction after a simple ring on highly conductive metals

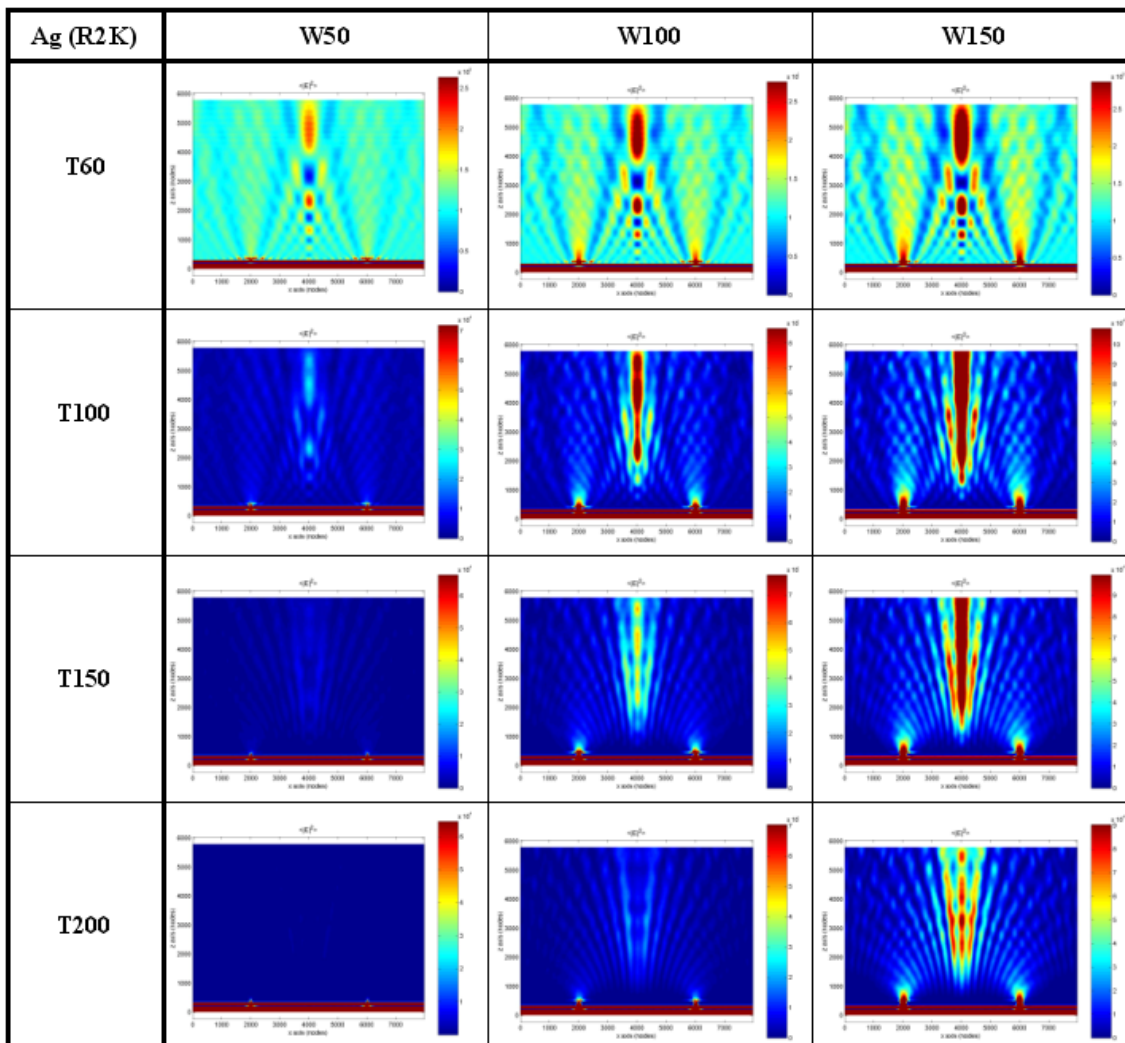
D.2.1. A ring in a silver (Ag) layer

- R1K



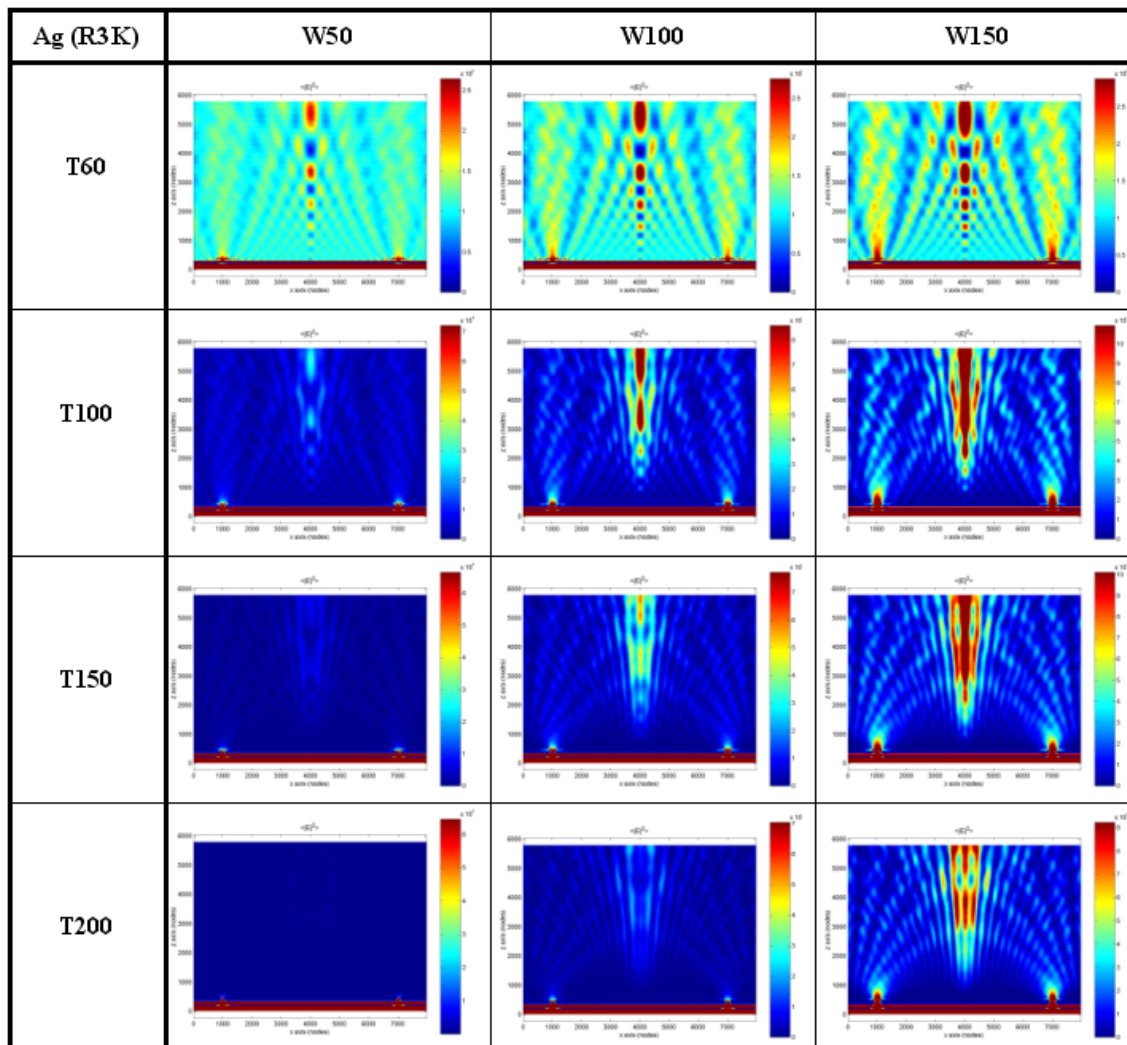
D.2.1. A ring in a silver (Ag) layer

- R2K



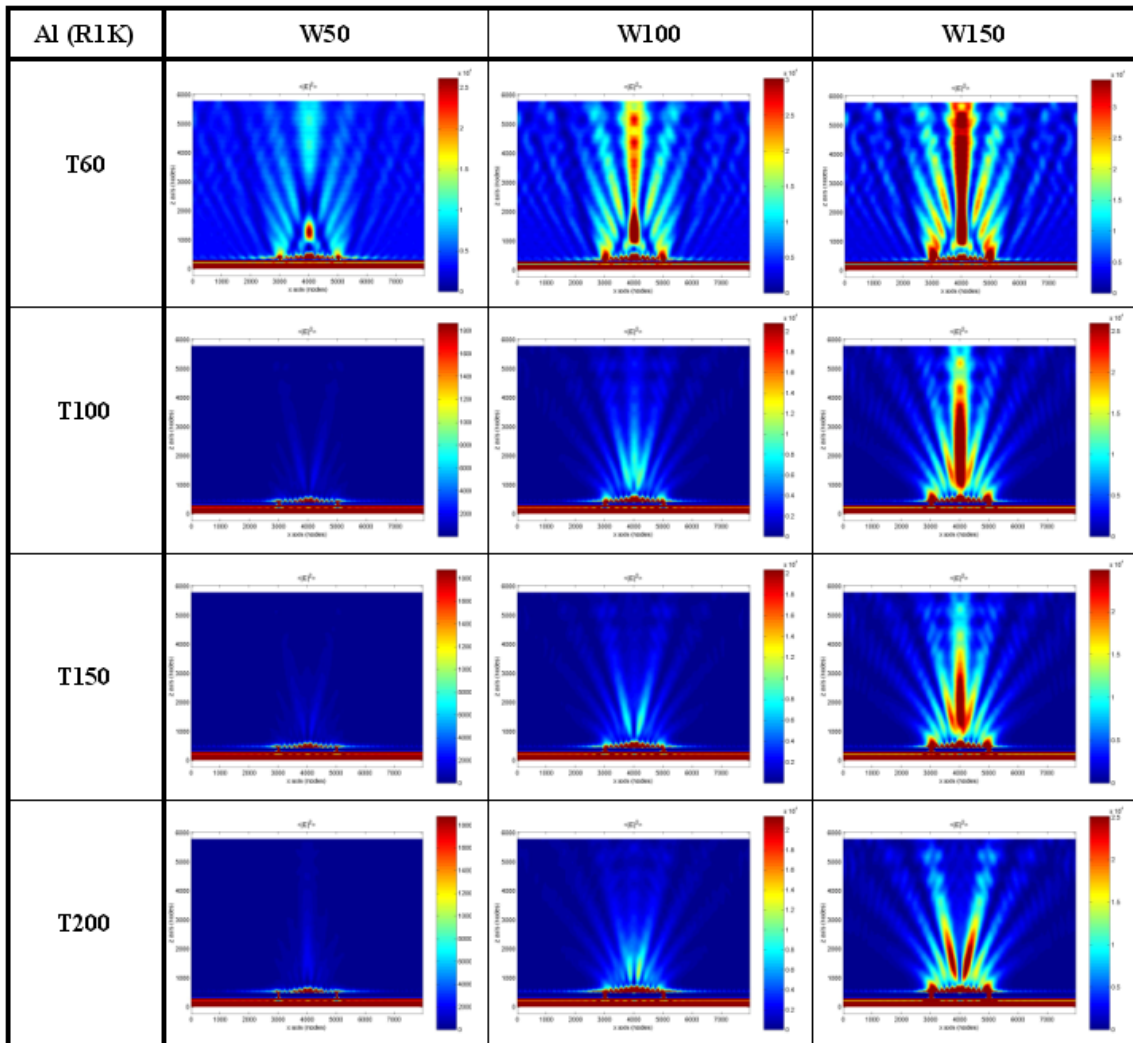
D.2.1. A ring in a silver (Ag) layer

- R3K



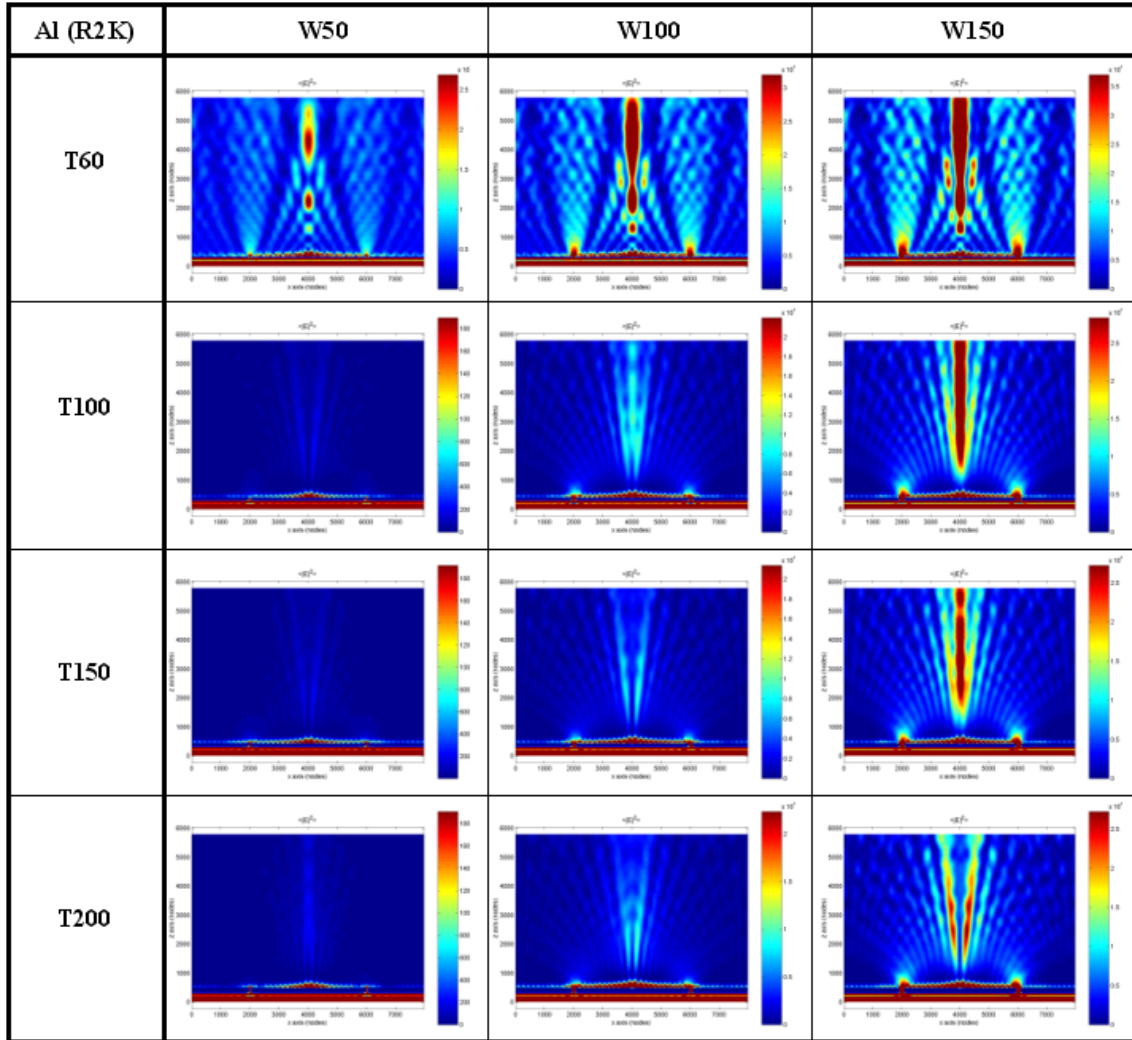
D.2.2. A ring in an aluminum (Al) layer

- R1K



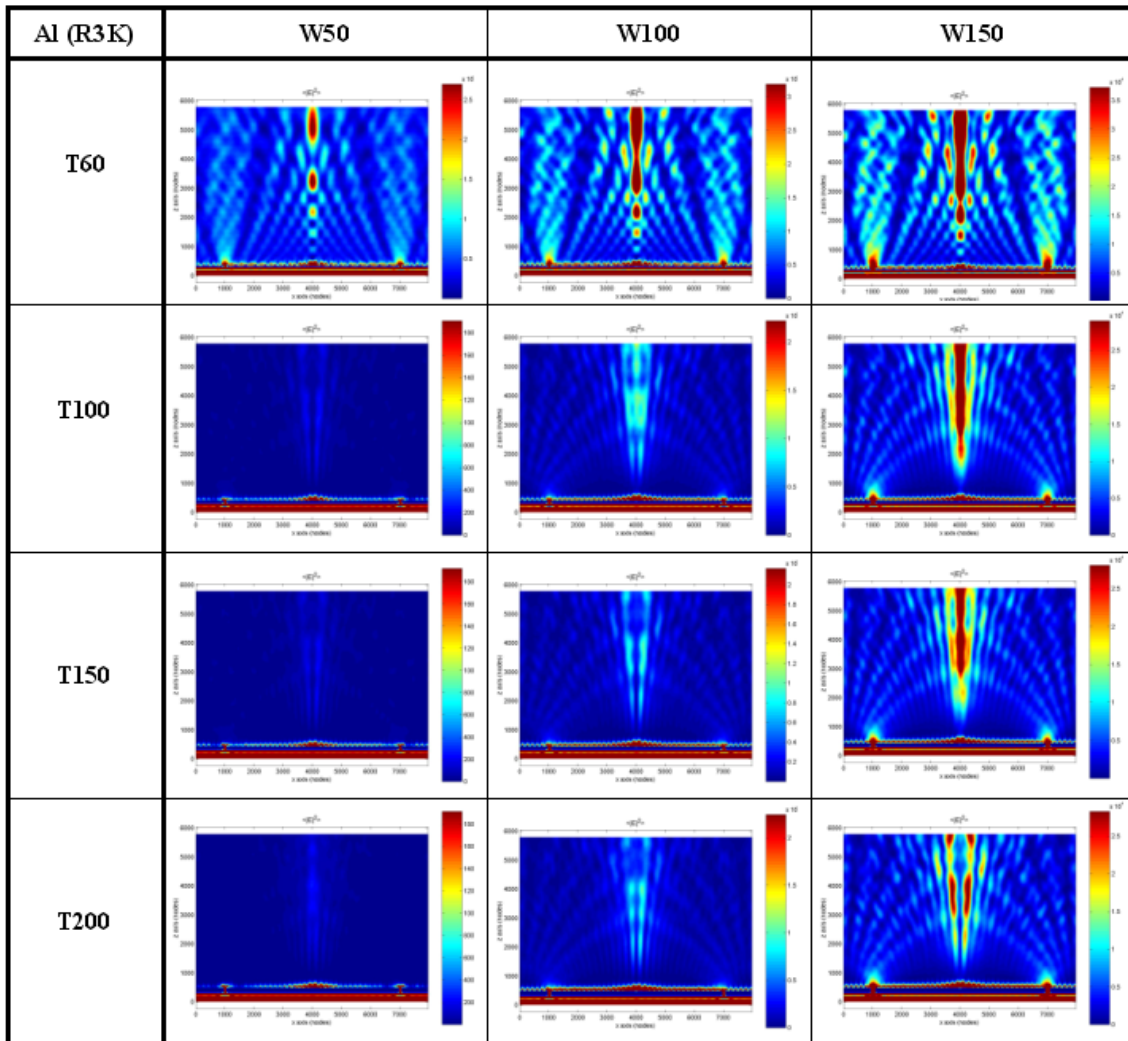
D.2.2. A ring in an aluminum (Al) layer

- R2K



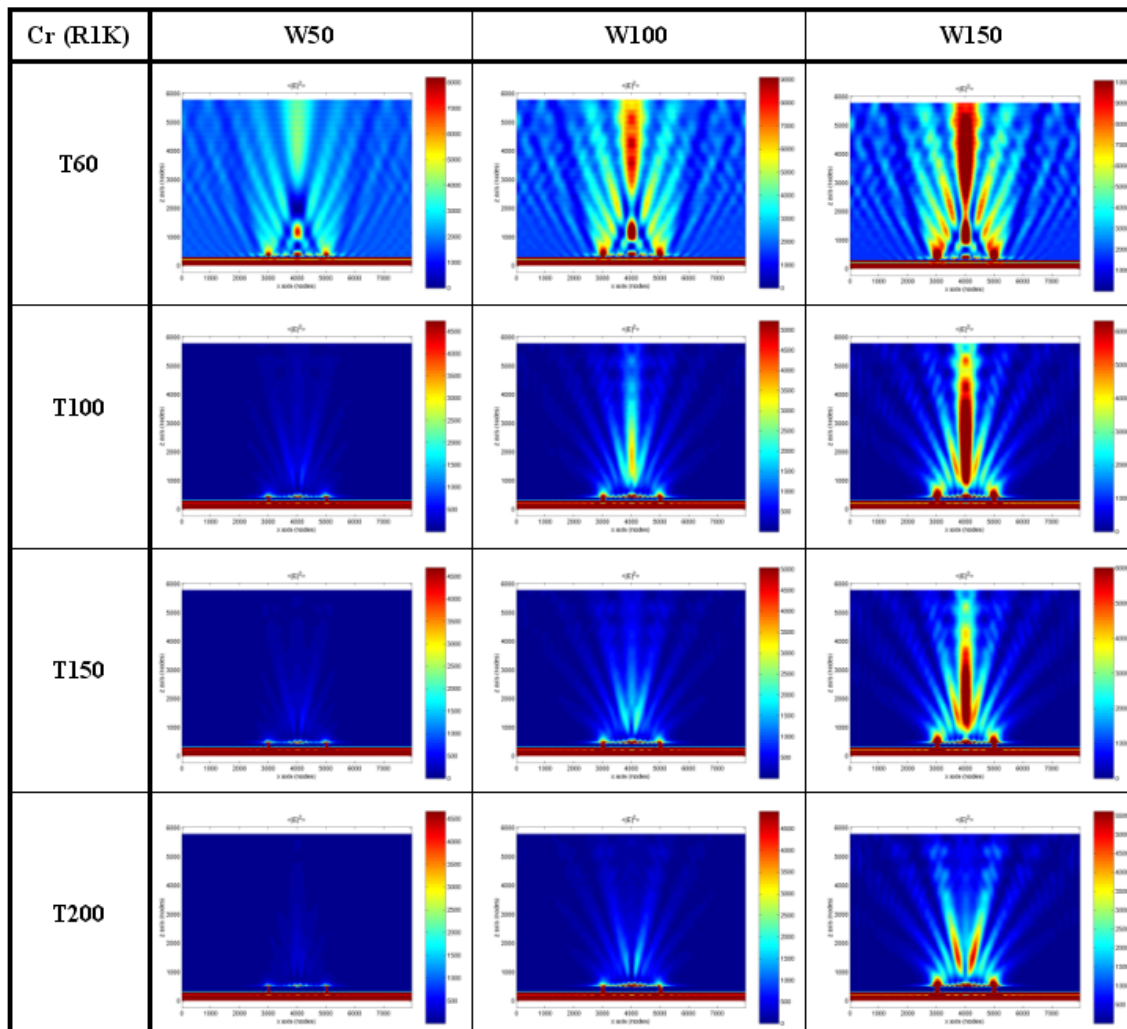
D.2.2. A ring in an aluminum (Al) layer

- R3K



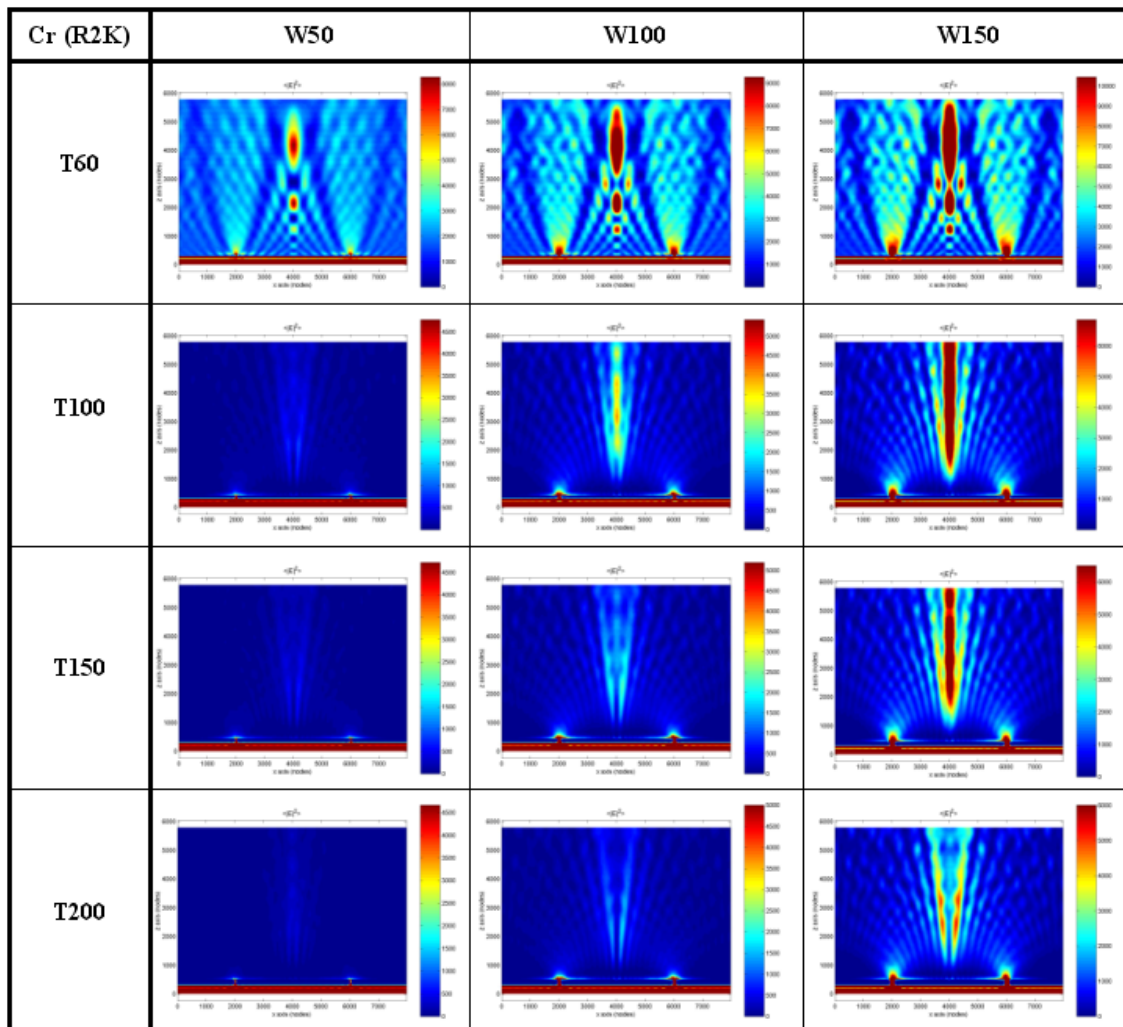
D.2.3. A ring in a chromium (Cr) layer

- R1K



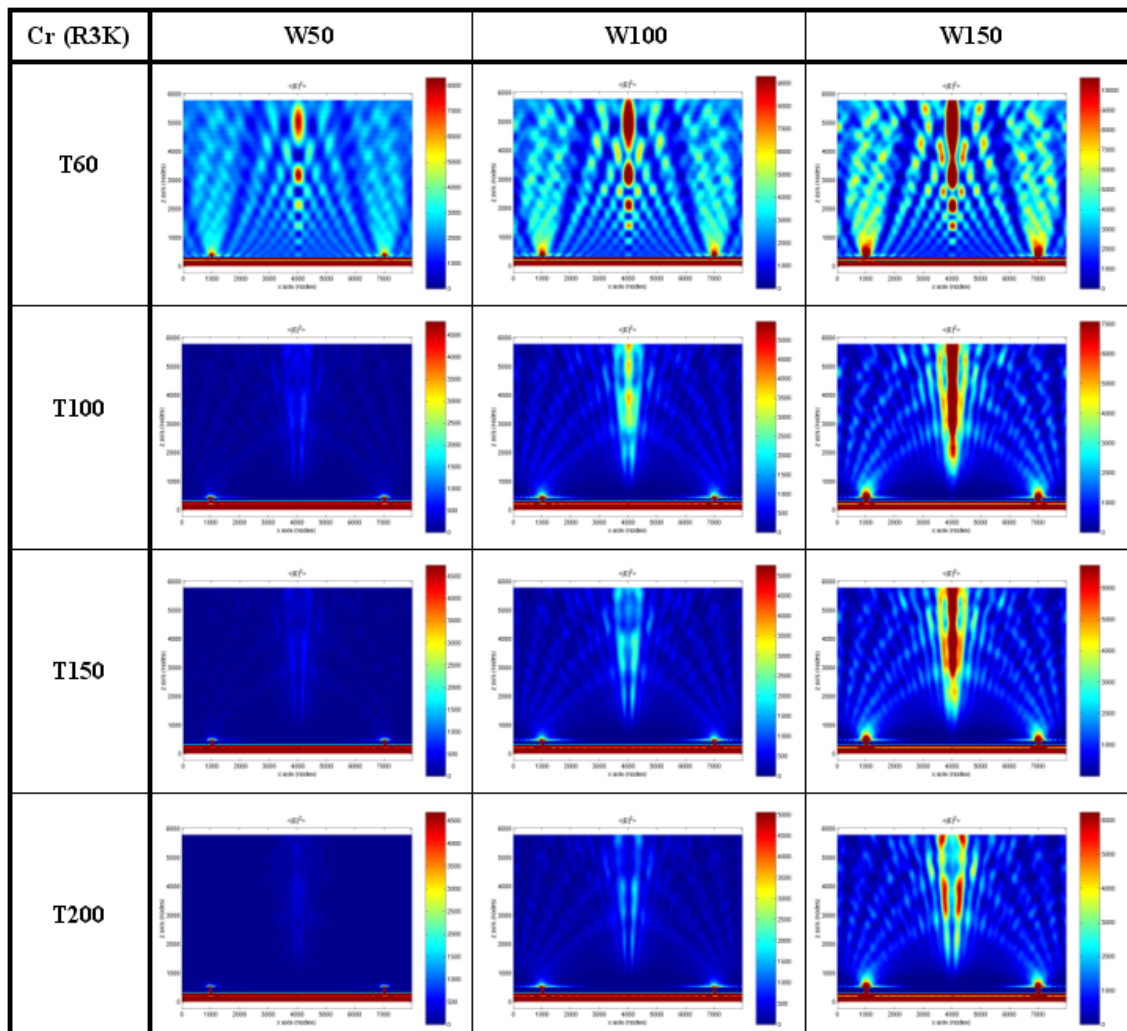
D.2.3. A ring in a chromium (Cr) layer

- R2K



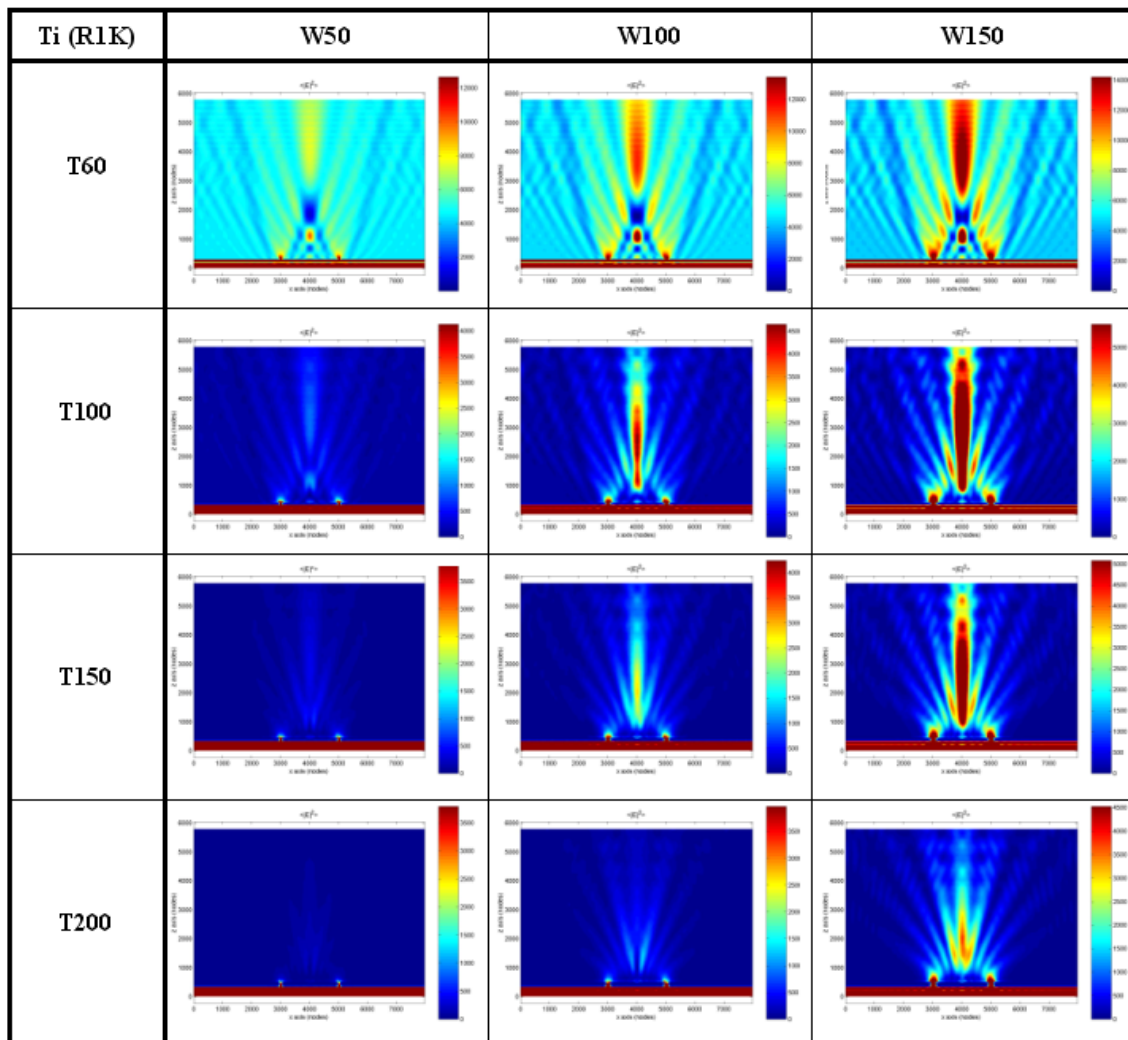
D.2.3. A ring in a chromium (Cr) layer

- R3K



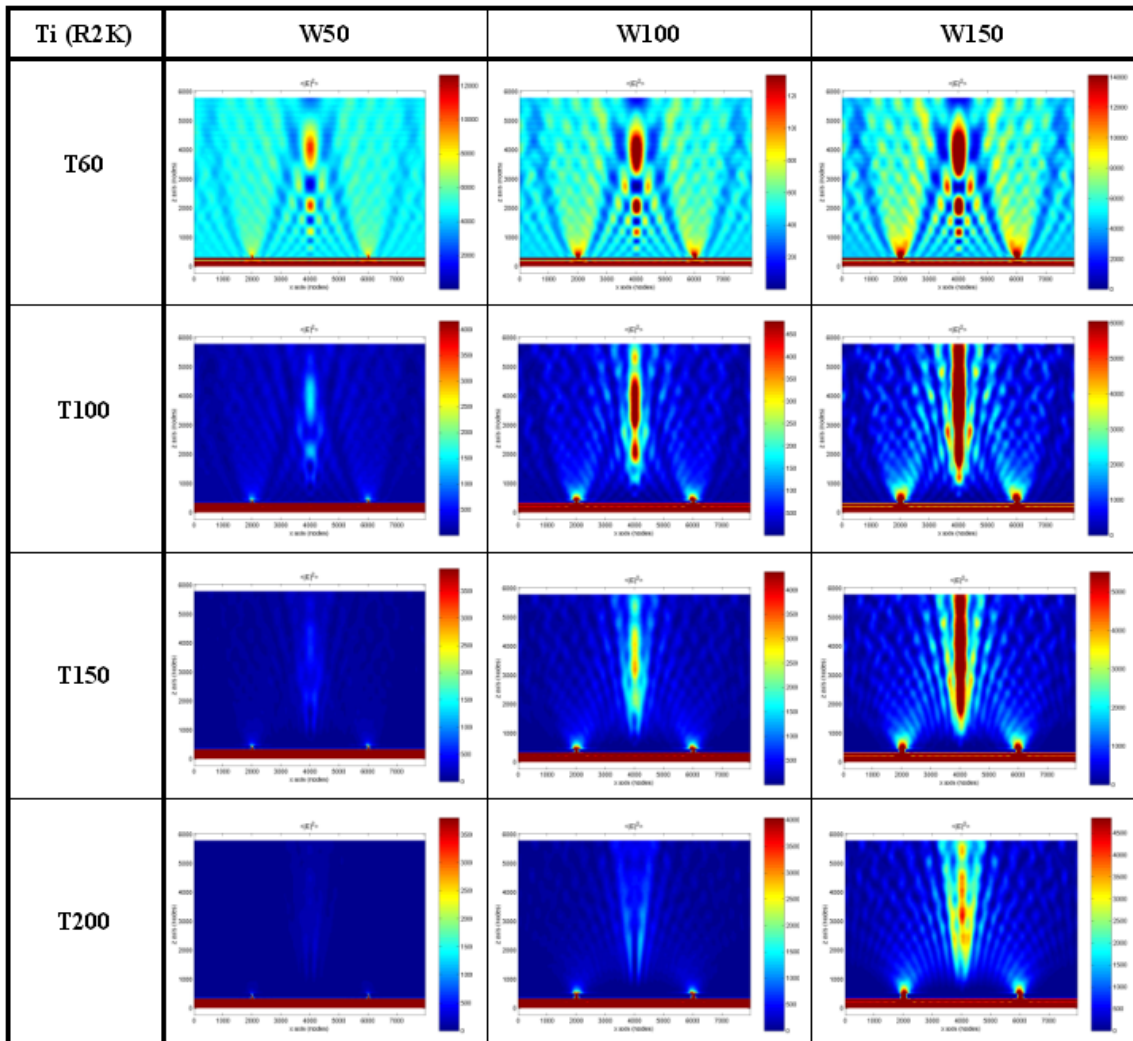
D.2.4. A ring in a titanium (Ti) layer

- R1K



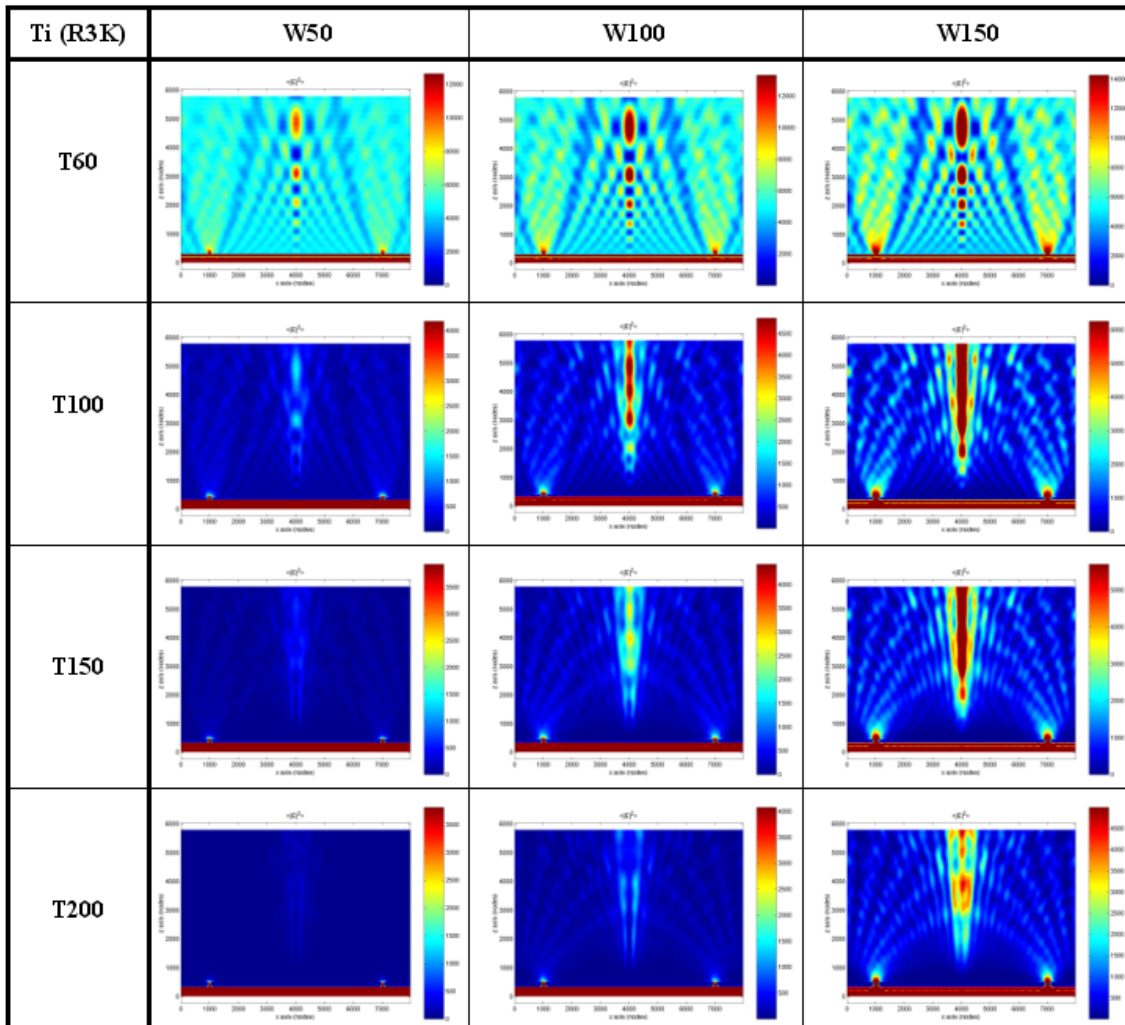
D.2.4. A ring in a titanium (Ti) layer

- R2K



D.2.4. A ring in a titanium (Ti) layer

- R3K



VITA

PERSONAL DATA:

Full Name: Sungkyu Seo
 Address: ZEC 31, ECE Department, Texas A&M University, College Station, TX
 77843-3128, U.S.A.
 Place of Birth: Masan, Republic of Korea
 E-mail: seo_sungkyu@tamu.edu

EDUCATION:

Ph.D.: in Electrical and Computer Engineering, Texas A&M University, College Station, TX,
 U.S.A. (Dec. 2007)
 B.S.: in Electrical Engineering, Korea University, Seoul, Korea (Aug. 1998)

PROFESSIONAL EXPERIENCE:

Research Assistant, ECE Dept., Texas A&M University (Nov. 2003 ~ May. 2007)
 Assistant Researcher, Microsystems Lab., EE Dept., Korea University (Sep. 2002 ~ Jun. 2003)
 Technical Staff (Assistant Manager), R&D Group, Human Electronics (Jun. 1998 ~ Feb. 2002)

AWARDS AND HONORS:

KUSCO-KSEA Scholarship (Aug. 2007) – KUSCO-KSEA
 Best Poster Award - 3rd prize (Aug. 2007) – UKC 2007 Conference, Washington D.C.
 Graduate Research Fellowship (Jun. 2005) – Dept. of ECE, Texas A&M University
 Graduate Scholarship (Sep. 2003) – Dept. ECE, Texas A&M University
 National New Technology (NT) Award (Feb. 2001) – The MOCIE of Korea
 Outstanding Academic Achievement Award (Sep. 1997) – College of Eng., Korea University

MAJOR FIELD OF SPECIALIZATION:

Nano-Optics & -Photonics (EM Wave Simulation, Device Fabrication, and Optics Experiment).
 Super Resolution Imaging overcoming Diffraction Limit using Plasmonic Lens.
 Nano Lithography (Optical / E-beam / Maskless) using Optical Antenna.
 Nano-Bio Sensor Design, Fabrication and Analysis.
 Micro / Nano Electro Mechanical Systems.

PUBLICATIONS:

- [1] S. Seo,* H. C. Kim, H. Ko, and M. Cheng, “Sub-wavelength Proximity Nanolithography using a Plasmonic Lens”, *Journal of Vacuum Science and Technology B*, 2007 (Accepted and in-press after minor revision - *Corresponding author).
- [2] S. Seo, M. D. King, R. F. Young, L. B. Kish and M. Cheng, “Patterning a Nanowell Sensor Biochip for Specific and Rapid Detection of Bacteria”, *Microelectronic Engineering*, 2007 (Accepted and in-press after minor revision).
- [3] S. Seo, H. C. Kim, M. Cheng, X. Ruan and W. Ruan, *Journal of Vacuum. Science and Technology B* **24**, No. 6, pp. 3133-3138 (2006).
- [4] M. D. King, S. Seo, J.U. Kim, R. Young, M. Cheng, and L.B. Kish, *Journal of Biological Physics and Chemistry*, **5**, pp. 3-7 (2005).
- [5] L.B. Kish, M. Cheng, J.U. Kim, S. Seo, M.D. King, R. F. Young, A. Der and G. Schmera, *Fluctuations and Noise Letters* **5**, L105-108 (2005).